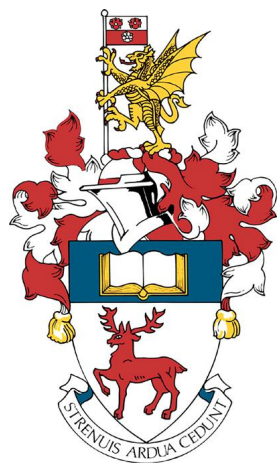


# UNIVERSITY OF SOUTHAMPTON

FACULTY OF ENGINEERING AND THE ENVIRONMENT



## Acquisition of manoeuvring characteristics of ships using RANS CFD

by

Marin Lauber

Supervised by Professor Pandeli Temarel

A thesis presented for the degree of Master of Science

September 2018

This thesis was submitted for examination in September, 2018. It does not necessarily represent the final form of the thesis as deposited in the University after examination.

# Acquisition of manoeuvring characteristics of ships using RANS CFD

Marin Lauber

## Abstract

The motivation behind the presented work is to provide a comprehensive investigation of the modelling aspects of ship manoeuvring simulations. To achieve this, slow motion derivatives and oscillatory coefficients of a benchmark model are derived by means of static drift and planar motion mechanism simulations. Aspects such as mesh and time-step sensitivity are investigated, together with a comparison of free surface modelling techniques and turbulence closure. Finally, the contributions to the derivatives from an undeflected rudder are exposed.

Numerical simulations are undertaken using a Reynolds-Averaged Navier-Stoke (RANS) finite volume method (Star-CCM<sup>+</sup>) to replicate captive model tests. Static drift and planar motion mechanism simulations in pure sway and yaw are performed for the KVLCC2 at model scale.

A proper verification and validation is performed for both sets of results. For static drift simulations, values of numerical uncertainty are found to be adequately small. However, the comparison error does not allow proper validation of the results, yet it is low enough for the agreement with the experimental data to be regarded as satisfactory. The limitations of the verification and validation procedure are reached with the results of the PMM simulations, and this does not allow numerical uncertainties to be estimated, nor to validate the results. Nevertheless, a less formal validation is performed, also showing acceptable agreement with the experimental data.

The three different time-steps chosen show very similar results, all being able to accurately capture the forces and moments. Good agreement is obtained as well when comparing local flow measurements, such as the wave pattern, nominal wake, etc., to numerical predictions. More disparity is found between the different turbulence models used, with the one-equation model showing the largest discrepancies.

This work demonstrated that RANS methods can be effectively used to derive the manoeuvring characteristics of ships in a relevant time-frame, but some numerical aspects require careful considerations. The results obtained showed good enough agreement with experimental data to allow different manoeuvring simulations to be performed using the derivatives obtained.

# **Declaration of Authorship**

I, Marin Lauber declare that this thesis and the work presented in it are my own and has been generated by me as the result of my own original research.

I confirm that:

1. This work was done wholly or mainly while in candidature for a degree at this University;
2. Where any part of this thesis has previously been submitted for any other qualification at this University or any other institution, this has been clearly stated;
3. Where I have consulted the published work of others, this is always clearly attributed;
4. Where I have quoted from the work of others, the source is always given. With the exception of such quotations, this thesis is entirely my own work;
5. I have acknowledged all main sources of help;
6. Where the thesis is based on work done by myself jointly with others, I have made clear exactly what was done by others and what I have contributed myself;
7. None of this work has been published before submission;

# Dedication

Dedicated to my beloved parents and family. For their love, endless support, encouragement and sacrifices.

# Acknowledgements

I would like to express my very great appreciation to Professor Pandeli Temarel for his valuable help and constructive suggestions during the planning and development of this thesis. I would also like to thank him for introducing me to the topic of ship manoeuvring, as well for the time he kindly dedicated to me.

I also extend my sincere thanks to my fellow M.Sc. students who provided an enjoyable working environment during this year of study.

I would also like to thank Miss Ellen Pick for proofreading this thesis, any mistake however remains my entire responsibility.

I would also acknowledges the use of the IRIDIS High Performance Computing Facility, and associated support services at the University of Southampton, in the completion of this work.

# Contents

<b>List of Figures</b>	<b>IV</b>
<b>List of Tables</b>	<b>VI</b>
<b>Nomenclature</b>	<b>VII</b>
<b>Dimensionless Quantities</b>	<b>X</b>
<b>List of Abbreviations</b>	<b>XI</b>
<b>1 Introduction</b>	<b>1</b>
1.1 Aim and Objectives . . . . .	2
1.2 Outline of the thesis . . . . .	3
<b>2 Background</b>	<b>5</b>
2.1 Captive and Free-running Simulations . . . . .	5
2.2 Mesh Motion . . . . .	7
2.3 Mathematical Model . . . . .	8
2.4 Free Surface . . . . .	8
2.5 Turbulence Closure . . . . .	9
2.6 Verification and Validation . . . . .	10
2.7 Conclusion on Background . . . . .	10
<b>3 Mathematical Model</b>	<b>12</b>
3.1 Coordinate System and Nomenclature . . . . .	12
3.2 Equations of Motion . . . . .	13
3.2.1 Static Drift . . . . .	14
3.2.2 Planar Motion Mechanism in Pure Sway . . . . .	14
3.2.3 Planar Motion Mechanism in Pure Yaw . . . . .	15
3.2.4 Rudder Contribution . . . . .	16
3.3 Viscous Flow . . . . .	16
3.4 Turbulence Closure . . . . .	17

3.5	Volume of Fluid . . . . .	18
<b>4</b>	<b>Methodology</b>	<b>20</b>
4.1	Static Drift Simulations . . . . .	20
4.1.1	Domain . . . . .	20
4.1.2	Mesh . . . . .	21
4.1.3	Numerical Solution . . . . .	23
4.1.4	Boundary Conditions . . . . .	25
4.1.5	Additional Investigations . . . . .	27
4.2	Planar Motion Mechanism Simulations . . . . .	28
4.2.1	Domain . . . . .	28
4.2.2	Overset Mesh . . . . .	28
4.2.3	Numerical Solution . . . . .	29
4.2.4	Boundary Conditions . . . . .	30
4.2.5	Motion . . . . .	31
4.2.6	Additional Investigations . . . . .	32
4.3	Verification and Validation . . . . .	32
<b>5</b>	<b>Static Drift Simulations</b>	<b>36</b>
5.1	Verification and Validation . . . . .	36
5.1.1	Global Quantities . . . . .	36
5.1.2	Local Flow Quantities . . . . .	42
5.2	Slow Motion Derivatives . . . . .	46
5.3	Additional Investigations . . . . .	48
5.4	Discussion . . . . .	49
<b>6</b>	<b>Planar Motion Mechanism Simulations</b>	<b>51</b>
6.1	Experimental Data Filtering . . . . .	51
6.2	Oscillatory Coefficients . . . . .	52
6.3	Verification and Validation . . . . .	55
6.3.1	Global Quantities . . . . .	55
6.3.2	Local Flow Quantities . . . . .	58
6.4	Additional Investigations . . . . .	58
6.5	Discussion . . . . .	59
<b>7</b>	<b>Conclusion and Future Work</b>	<b>62</b>
7.1	Conclusions . . . . .	62
7.2	Recommendations for Future Work . . . . .	63
	<b>References</b>	<b>65</b>

<b>A</b>	<b>Literature Review</b>	<b>70</b>
<b>B</b>	<b>Turbulence Models</b>	<b>75</b>
B.1	$k-\omega$ SST . . . . .	75
B.2	Realizable $k-\epsilon$ . . . . .	76
B.3	Spalart-Allmaras . . . . .	77
<b>C</b>	<b>Simulation Set-up</b>	<b>78</b>
C.1	Wall Distance ( $y^+$ ) and Boundary Layer Depth . . . . .	78
C.2	Kelvin Wake Refinement . . . . .	79
C.3	User Defined Functions . . . . .	79
C.4	Experimental Data Uncertainty . . . . .	80
C.5	Signal Processing . . . . .	81
C.6	Taylor Series Fit Verification . . . . .	81
C.7	Free Surface Elevation . . . . .	83
C.8	Star-CCM <sup>+</sup> Meshing Macro . . . . .	84

# List of Figures

3.1	Space and ship-fixed coordinate system. . . . .	12
4.1	Computational domain for the static drift simulations. . . . .	21
4.2	Bottom and profile view of the non-dimensional wall distance ( $y^+$ ) on the KVLCC2 for the static drift simulation ( $\beta = 0^\circ$ , $Fr = 0.142$ ). . . . .	22
4.3	Global view of the standard mesh refinements used for the static drift simulations ( $\beta = 0^\circ$ , $Fr = 0.142$ ) together with details of the refinements around the model. . . . .	23
4.4	CFL number at the free surface for the static drift simulation ( $\beta = 8^\circ$ , $Fr = 0.142$ ). . . . .	25
4.5	Time-history of the sway force and yaw moment during a static drift simulation using the standard mesh, ( $\beta = 8^\circ$ , $Fr = 0.142$ ). . . . .	26
4.6	Sway force and yaw moment for the initialized solution (—) and the non-initialized solution (---) for the PMM in pure sway ( $T = 12s$ , $y_0 = 0.2026m$ ). . . . .	29
4.7	Overall view of the domain used for the PMM simulations. . . . .	30
4.8	Illustration of the imposed motion for the PMM in pure yaw ( $T = 12s$ , $Fr = 0.142$ ) at three different times. . . . .	32
4.9	Convergence of the $L_2$ norm of the pressure and shear stress on the hull for the static drift simulation for the standard mesh ( $\beta = 8^\circ$ , $Fr = 0.142$ ). . . . .	34
5.1	Relative error in the force and moment prediction for the different meshes with respect to the extrapolated value $\hat{S}_{\text{ext}}^{21}$ . . . . .	38
5.2	$L_2$ norm of the pressure changes between consecutive iterations on the hull for different time-step/inner iteration combinations. . . . .	40
5.3	Isocontours of the Q-criterion (value of $1.5 \text{ s}^{-2}$ ) coloured with the normalized helicity ( $H_n$ ). . . . .	41
5.4	Bottom view of the wall shear stress on the KVLCC2 for the $k-\omega$ SST (top, standard simulation) and the Spalart-Allmaras (bottom) turbulence model for the static drift case ( $\beta = 8^\circ$ , $Fr = 0.142$ ). . . . .	43
5.5	Wave elevation around the KVLCC2, from CFD of present study (top) and experimental data (Kim et al., 2001)(bottom) for $Fr = 0.142$ , $\beta = 0^\circ$ . . . . .	44

5.6 Comparison of normalized wave profile along the hull of the model ( $Fr = 0.142$ , $\beta = 0^\circ$ ). . . . .	44
5.7 Normalized velocity in the nominal wake of the KVLCC2, from CFD of present study (right) and experimental data (Kume et al., 2006)(left) for $Fr = 0.142$ , $\beta = 0^\circ$ . . . . .	45
5.8 Isocontours of Q-criterion (value of $1.5 s^{-2}$ ) coloured with normalized helicity ( $H_n$ ) showing the vortical structures forming on the KVLCC2 ( $\beta = 16^\circ$ , $Fr = 0.142$ ) using the $k-\omega$ SST turbulence model. . . . .	45
5.9 Sway force for different sway velocities, showing the mesh, time-step and turbulence sensitivity results. . . . .	47
5.10 Yaw moment for different sway velocities, showing the mesh, time-step and turbulence sensitivity results. . . . .	48
6.1 Power-spectral density of the sway force and yaw moment for the PMM in pure sway, data from experiment ( $T = 12$ s, $y_0 = 0.2026m$ ). . . . .	52
6.2 Sway force and yaw moment for a single period of oscillation for the PMM in pure sway ( $T = 12$ s, $y_0 = 0.2026m$ ). . . . .	53
6.3 Experimental data fitting for the pure yaw simulation ( $T = 12$ s). . . . .	54
6.4 CFD data fitting for the pure yaw simulation ( $T = 12$ s). . . . .	54
C.1 Instantaneous free surface elevation for the PMM in pure sway at a time $t=36$ s after motion initialisation. Initialized solution. . . . .	83
C.2 Instantaneous free surface elevation for the PMM in pure sway at a time $t=36$ s after motion initialisation. Non-initialized solution. . . . .	83

# List of Tables

1.1	List of contributors for benchmark data for SIMMAN 2014 . . . . .	2
1.2	Particulars of the KVLCC2, ship and model. . . . .	4
2.1	Range of benchmark data from NMRI for the KVLCC2. . . . .	10
4.1	Implicit unsteady and segregated solver parameters for the static drift simulations. . . . .	26
4.2	Boundary conditions for the static drift simulations. . . . .	27
4.3	Implicit unsteady and segregated solver parameters for the planar motion mechanism simulations. . . . .	31
5.1	$L_2$ norm of the change between iterations for the different meshes ( $\beta = 8^\circ$ , $Fr = 0.142$ ). . . . .	37
5.2	Grid convergence study for the static drift simulations ( $\beta = 8^\circ$ , $Fr = 0.142$ ). .	38
5.3	Temporal sensitivity study for the static drift simulations ( $\beta = 8^\circ$ , $Fr = 0.142$ ). . . . .	40
5.4	Comparison of slow motion derivatives against experimental values. Gradients calculated using values from $\beta \pm 4^\circ$ . . . . .	47
5.5	Comparison of slow motion derivatives for bare hull and hull with rudder. .	49
6.1	Mesh and solver metrics for the planar motion mechanism simulations. . . . .	55
6.2	Grid convergence study for the planar motion mechanism in pure sway ( $T=12s$ , $y_0 = 0.2026m$ ). . . . .	56
6.3	Oscillatory coefficients from planar motion mechanism simulations against experimental data. . . . .	57
6.4	Oscillatory coefficients from planar motion mechanism simulations in pure sway ( $T=12s$ ) with for different mesh sizes and turbulence models. . . . .	57
6.5	Influence of rudder on oscillatory coefficients from PMM in pure sway and yaw. . . . .	61

# Nomenclature

$B_{WL}$	breadth on waterline	[m]
$C_T$	total drag coefficient	[-]
$C_{u_l}$	lower value of CFL threshold	[-]
$C_{u_u}$	upper value of CFL threshold	[-]
$D$	experimental result	[various]
$e_a^{ij}$	approximate relative error between $i^{th}$ and $j^{th}$ solution	[-]
$E$	comparison error	[various]
$Fr$	Froude number	[-]
$g$	acceleration due to gravity	[m/s <sup>2</sup> ]
$h$	water depth	[m]
$I_{zz}$	second moment of inertia	[kg m <sup>2</sup> ]
$L_{PP}$	length between perpendiculars	[m]
$L_{WL}$	length on waterline	[m]
$m$	mass	[kg]
$N$	yaw moment	[Nm]
$n$	rate of revolution	[1/s]
$p$	apparent order of convergence	[-]
$p$	pressure	[N/m <sup>2</sup> ]
$r$	yaw velocity	[rad/s]
$\dot{r}$	yaw acceleration	[rad/s <sup>2</sup> ]
$r_{ij}$	refinement ration between $i^{th}$ and $j^{th}$ mesh	[-]

---

$Re$	Reynolds number	[ $-$ ]
$R_G$	convergence of the solution	[ $-$ ]
$S$	numerical/simulation result	[ <i>various</i> ]
$S_{ij}$	mean strain-rate tensor	[ $1/s$ ]
$S_{km}$	numerical error of the $k^{th}$ variable at the $m^{th}$ refinement	[ <i>various</i> ]
$\hat{S}_{km}$	corrected numerical error of the $k^{th}$ variable at the $m^{th}$ refinement	[ <i>various</i> ]
$\hat{S}_{ext}^{21}$	extrapolated numerical solution	[ <i>various</i> ]
$T$	draft	[ $m$ ]
$T$	time period	[ $s$ ]
$u$	longitudinal velocity	[ $m/s$ ]
$u_i$	$i^{th}$ cartesian component of the velocity field	[ $m/s$ ]
$\dot{u}$	longitudinal acceleration	[ $m/s^2$ ]
$U_0$	free-stream velocity	[ $m/s$ ]
$U_\phi$	discretization uncertainty for variable $\phi$	[ <i>various</i> ]
$U_D$	uncertainty of the experiment	[ <i>various</i> ]
$U_G$	uncertainty due to discretization error	[ <i>various</i> ]
$U_I$	uncertainty due to iterative error	[ <i>various</i> ]
$U_V$	validation uncertainty	[ <i>various</i> ]
$U_{SN}$	numerical uncertainty of the simulation	[ <i>various</i> ]
$v$	transverse velocity	[ $m/s$ ]
$\dot{v}$	transverse acceleration	[ $m/s^2$ ]
$w$	vertical velocity	[ $m/s$ ]
$\dot{w}$	vertical acceleration	[ $m/s^2$ ]
$X$	longitudinal force	[ $N$ ]
$x$	longitudinal position	[ $m$ ]
$x_G$	longitudinal position of the centre of gravity	[ $m$ ]

---

$Y$	transverse force	[ $N$ ]
$y$	transverse position	[ $m$ ]
$y^+$	non-dimensional wall distance	[ $-$ ]
$y_0$	amplitude of oscillation	[ $-$ ]
$Z$	vertical force	[ $N$ ]
$z$	vertical position	[ $m$ ]
$\alpha$	volume fraction	[ $-$ ]
$\beta$	drift angle	[ $rad$ ]
$\gamma$	non-dimensional yaw rate	[ $-$ ]
$\delta$	rudder angle	[ $rad$ ]
$\delta_{ij}$	Kronecker delta	[ $-$ ]
$\delta_D$	error in the experimental value	[ <i>various</i> ]
$\delta_{SN}$	numerical error in simulated value	[ <i>various</i> ]
$\delta_{I_{km}}^*$	iterative error of the $k^{th}$ variable at the $m^{th}$ refinement	[ <i>various</i> ]
$\epsilon_{ij}$	change between $i^{th}$ and $j^{th}$ corrected solutions	[ <i>various</i> ]
$\theta$	pitch angle	[ $rad$ ]
$\lambda$	scale factor	[ $-$ ]
$\mu$	dynamic viscosity	[ $kg/(sm)$ ]
$\nu$	kinematic viscosity	[ $m^2/s$ ]
$\rho$	density of the fluid	[ $kg/m^3$ ]
$\tau_{ij}$	Reynolds stress tensor	[ $kg/ms^2$ ])
$\phi$	roll angle	[ $rad$ ]
$\phi^n$	value of variable $\phi$ at time $n$ .	[ <i>various</i> ]
$\psi$	yaw angle	[ $rad$ ]
$\omega$	angular velocity ( $2\pi/T$ )	[ $rad/s$ ]
$\Omega_{ij}$	vorticity or rotation tensor	[ $1/s$ ]
$\nabla$	displacement volume moulded	[ $m^3$ ]

# Dimensionless Quantities

Throughout this thesis, the different quantities used are made nondimensional as follows:

$$\begin{aligned} X' &= \frac{X}{\frac{1}{2}\rho U^2 L_{PP}^2} & Y' &= \frac{Y}{\frac{1}{2}\rho U^2 L_{PP}^2} & N' &= \frac{N}{\frac{1}{2}\rho U^2 L_{PP}^3} \\ u' &= \frac{u}{U} & v' &= \frac{v}{U} & \gamma = r' &= \frac{r L_{PP}}{U} \\ \dot{u}' &= \frac{\dot{u} L_{PP}}{U^2} & \dot{v}' &= \frac{\dot{v} L_{PP}}{U^2} & \dot{r}' &= \frac{\dot{r} L_{PP}^2}{U^2} \end{aligned}$$

The nondimensional hydrodynamic coefficients are therefore:

$$\begin{aligned} X'_v &= \frac{X_v}{\frac{1}{2}\rho U L_{PP}^2} & Y'_v &= \frac{Y_v}{\frac{1}{2}\rho U L_{PP}^2} & N'_v &= \frac{N_v}{\frac{1}{2}\rho U L_{PP}^3} \\ X'_{\dot{v}} &= \frac{X_{\dot{v}}}{\frac{1}{2}\rho L_{PP}^3} & Y'_{\dot{v}} &= \frac{Y_{\dot{v}}}{\frac{1}{2}\rho L_{PP}^3} & N'_{\dot{v}} &= \frac{N_{\dot{v}}}{\frac{1}{2}\rho L_{PP}^4} \\ X'_r &= \frac{X_r}{\frac{1}{2}\rho U L_{PP}^3 r} & Y'_r &= \frac{Y_r}{\frac{1}{2}\rho U L_{PP}^3 r} & N'_r &= \frac{N_r}{\frac{1}{2}\rho U L_{PP}^4 r} \\ X'_{\dot{r}} &= \frac{X_{\dot{r}}}{\frac{1}{2}\rho L_{PP}^5 r} & Y'_{\dot{r}} &= \frac{Y_{\dot{r}}}{\frac{1}{2}\rho L_{PP}^5 r} & N'_{\dot{r}} &= \frac{N_{\dot{r}}}{\frac{1}{2}\rho L_{PP}^6 r} \end{aligned}$$

The partial differential notation proposed in SNAME (1950) is used, it is repeated here for completeness:

$$Y_v = \frac{\partial Y}{\partial v} \quad N_v = \frac{\partial N}{\partial v} \quad Y_{\dot{v}} = \frac{\partial Y}{\partial \dot{v}} \quad N_{\dot{v}} = \frac{\partial N}{\partial \dot{v}}$$

# List of Abbreviations

CFD	Computational Fluid Dynamics
CFL	Courant–Friedrichs–Lewy
CMT	Circular Motion Test
CPU	Central Processing Unit
(D)DES	(Delayed) Detached Eddy Simulation
DOF	Degrees Of Freedom
DTMB	David Taylor Model Bassin
EASM	Explicit Algebraic Stress Model
FVM	Finite Volume Method
GCI	Grid Convergence Index
HSVA	Hamburgische Schiffbau-Versuchanstalt
IIHR	Iowa Institute of Hydraulic Research
IMO	International Maritime Organization
INSEAN	Istituto Nazionale Per Studi Ed Esperienze Di Architettura Navale
ITTC	International Towing Tank Conference
JBC	Japanese Bulk Carrier
JMU	Japan Marine United Corporation
KCS	KRISO Container Ship
KRISO	Korean Research Institute of Ships and Ocean Engineering
LES	Large Eddy Simulation
LS	Level Set
MARIN	Maritime Research Institute Netherlands
MMG	Mathematical Manoeuvring Model Group
MOERI	Maritime & Ocean Engineering Research Institute
NMRI	National Maritime Research Institute
PIV	Particle Image Velocimetry

---

## LIST OF ABBREVIATIONS

PMM	Planar Motion Mechanism
QUICK	Quadratic Upwind Interpolation for Convective Kinematics
RANS	Reynolds-Averaged Navier-Stokes
RMS	Root Mean Square
RST	Reynolds Stress Transport
SD	Static Drift
SIMPLE	Semi-Implicit Method for Pressure Linked Equations
SST	Shear Stress Transport
VOF	Volume Of Fluid
V&V	Verification & Validation
VIRTUE	Virtual Tank Utility in Europe
VLCC	Very Large Crude Carrier

# Chapter 1

## Introduction

Historically, resistance and propulsion, as well as seakeeping were the main considerations in ship design, as far as the performance of the ship was concerned. The manoeuvrability of a ship was assessed by sea trials, providing a very accurate assessment of its capabilities when conducted properly. However, if its manoeuvrability was regarded as unsatisfactory, modifications were extremely expensive.

More recently, with the implementation of manoeuvring resolutions by the International Maritime Organisation, see (IMO, 2002), requirements for manoeuvring predictions became more demanding. As a result, naval architects need to be able to accurately predict the manoeuvring characteristics of a ship (such as its course keeping or turning abilities) during the design. Before computational methods provided an attractive alternative, model tests or empirical methods were the preferred approaches.

Model tests can be used to directly simulate standard manoeuvres required by the IMO, such as a turning circle, zigzag, etc., see Bertram (2012) for a thorough description of the different manoeuvres. This is the free-running approach, which is regarded as the most accurate, but requires large facilities and a self-propelled model as well as a tracking equipment, which greatly increases the complexity of the test.

An alternative is captive model test, where the model is forced into different harmonic motions and the forces and moments are measured. From those, hydrodynamic coefficients are extracted. They can then be used with suitable equations of motion to simulate any manoeuvre. Initially, free-running tests are less costly than captive model tests, but once the hydrodynamic coefficients have been determined, a whole range of manoeuvres can be simulated using those coefficients, as opposed to the single manoeuvre performed with the free-running approach.

Empirical methods (Clarke, 1983; Inoue and Kijima, 1978; Kijima et al., 1990) are comprised of a large database of hydrodynamic coefficients, obtained from model test, fitted with a regression method. These yield acceptable results provided they are applied to ships similar to the one used to create the database.

**Table 1.1:** List of contributors for benchmark data for SIMMAN 2014.

Test <sup>a</sup>	KVLCC2	KCS	DTMB-5145
SD (Bare)	NMRI	-	FORCE, IIHR <sup>b</sup>
SD (App.)	NMRI, HMRI	JMU, FORCE	MARIN
PMM (Bare)	NMRI	-	FORCE, IIHR <sup>c</sup>
PMM (App.)	NMRI, HMRI	JMU, NMRI, FORCE	MARIN

<sup>a</sup> SD: Static Drift, PMM: Planar Motion Mechanism

<sup>b</sup> Results from the Istituto Nazionale per Studi ed Esperienze di Architettura Navale (INSEAN) are also available.

While extensive use of potential flow theory was, and still is made in seakeeping and hydroelasticity to determine the added-mass and the fluid damping of ship sections for use with strip theory, limited attempts have been made to predict manoeuvring characteristics of ships using this approach. One of the issues that arise is that the complex flow phenomenon present at the stern or bow of the ship is not well reproduced by strip theory (Clark, 1972), leading to poor predictions. Euler methods (inviscid Navier-Stokes), despite the increased fidelity, also result in large discrepancies compared to viscous approaches (Duman and Bal, 2016).

Not until Reynolds-Average Navier-Stokes (RANS) methods were applied to ship manoeuvring (Miyata et al., 1997) did numerical predictions improve. Despite their abilities to model viscous flow, such methods are extremely expensive, and the lack of confidence in the results does not allow direct application to the ship. They are mostly utilized at model scale, where experimental data is available to validate the findings. Recently, a large effort has been undertaken to render those approaches more mature, with the creation of a workshop for verification and validation of ship manoeuvring simulations (SIMMAN). They addressed this by creating a large database of experimental results and introduced a proper verification and validation procedure, see table 1.1 for an exhaustive list of the data available.

## 1.1 Aim and Objectives

This thesis aims at investigating the modelling aspects of ship manoeuvring using RANS methods. Static drift (SD) and planar motion mechanism (PMM) tests in pure sway and yaw will be numerically replicated using a RANS finite volume commercial computational fluid dynamics (CFD) package (Star-CCM<sup>+</sup>) to derive the hydrodynamic coefficients of a benchmark ship, namely the KVLCC2 (table 1.2), see section 2.6 for the complete justification of this choice.

To achieve this aim, this project is structured as follows:

- Static drift simulations:
  - Verification and validation of the results obtained following SIMMAN (2014) and Stern et al. (2001) for a chosen test case ( $\beta = 8^\circ$ ).
  - Time-step and turbulence closure sensitivity study for the test case, using the Realizable  $k-\epsilon$  and Spalart-Allmaras model.
  - Static drift simulations at a range of drift angles ( $\pm 16^\circ$ ) using the chosen mesh and time-step to determine the slow motion derivative  $Y_v$  and  $N_v$ .
  - Additional study using the double-body approach, an approach where the forward speed of the model is reduced and an investigation of the contribution of the addition of an undeflected rudder to the derivatives.
- Planar motion mechanism simulations:
  - Verification and validation of the results obtained following SIMMAN (2014) and Stern et al. (2001) for a chosen test case (pure sway T=12 s).
  - Pure sway PMM simulation to acquire the velocity and linear acceleration dependent coefficients  $Y_v$ ,  $N_v$ ,  $Y_{\dot{v}}$  and  $N_{\dot{v}}$  for two periods: 12 and 6 seconds.
  - Pure yaw PMM simulation to acquire the rotary and angular acceleration dependent coefficients  $Y_r$ ,  $N_r$ ,  $Y_{\dot{r}}$  and  $N_{\dot{r}}$  for two periods: 12 and 6 seconds.
  - Additional investigation on turbulence closure for the chosen test case using the Realizable  $k-\epsilon$  model and on the contribution of an undeflected rudder to the oscillatory coefficients.

## 1.2 Outline of the thesis

This thesis is divided into 7 chapters. After this introduction and the definition of the aim and objectives, chapter 2 presents the background of ship manoeuvring simulations, giving an overview of the methods used and the results obtained as well as the current gap in the field.

Subsequently, chapter 3 introduces the background theory of numerical simulations of ship manoeuvring. The equations of motion, coordinate system and the equations of viscous flow are presented with emphasis on the methods used throughout this thesis.

Building on the information assembled, the methodology used to derive the manoeuvring derivatives of the KVLCC2 is presented in chapter 4. The mesh generation process, as well as the numerical solution are described together with the procedure for verification and validation of the numerical results.

Chapter 5 provides the results obtained for the static drift simulations, with emphasis on the verification and validation process as well as on the additional study described earlier. To conclude this chapter, the manoeuvring derivatives are presented and then discussed. A similar structure is used for chapter 6, which provides the results of the planar motion mechanism simulations.

Finally, chapter 7 concludes this thesis, also giving recommendations for future work.

**Table 1.2:** Particulars of the KVLCC2, ship and model.

Dimension	Ship	Model	Units
$\lambda$	1	1/110	[ $\cdot$ ]
$L_{PP}$	320.0	2.9091	[m]
$L_{WL}$	325.5	2.9591	[m]
$B_{WL}$	58.0	0.5273	[m]
$T$	20.8	0.1891	[m]
Displacement	312622	0.2349	[ $m^3$ ]
$I_{zz}$	-	89.67	[ $Nms^2$ ]
$x_G$	-	0.1009	[m]
$Fr$	0.142	0.142	[ $\cdot$ ]
$Re$	$2.14 \times 10^9$	$1.94 \times 10^6$	[ $\cdot$ ]
$U$	7.97	0.76	[m/s]
$\rho$	1026.0210	999.1026	[kg/m $^3$ ]
$\mu$	$1.220 \times 10^{-3}$	$1.138 \times 10^{-3}$	[kg/(sm)]

# Chapter 2

## Background

This chapter provides an introduction to numerical simulations of ship manoeuvring as well as a thorough and comprehensive review of the current practices. First, the free-running and captive approach are introduced. The different mathematical models and numerical strategies used are presented and contrasted. Finally, the verification and validation procedure is introduced with an overview of the available benchmark data for captive model test simulations.

The reader is referred to appendix A for a comprehensive list of the literature covering manoeuvring simulations.

### 2.1 Captive and Free-running Simulations

Numerical manoeuvring simulations using computational fluid dynamics can be categorized in the same way as model tests. Free-running simulations replicate self-propelled model tests of standard manoeuvres, such as zigzag, turning circle, pull-out manoeuvres, etc., while captive simulations replicate captive model tests.

Self-propelled model simulations were first performed for resistance computations. Carrica et al. (2010) used and overset mesh to descretize the propeller and a speed controller to find the self-propulsion point of the KVLCC1. Only surge, heave, roll and pitch motions were considered in this work. Head seas effects were later added (Carrica et al., 2011). These simulations were able to very accurately predict the resistance of the ship as well as its self-propulsion point, only underestimating the total drag coefficient by 2.5% while the propeller RPM were overestimated by 2%.

Applications of self-propelled model simulations to manoeuvring are more recent. For example, Mofidi and Carrica (2014) performed a standard 10/10 and a modified 1/15 zigzag manoeuvre with the Korean Container Ship (KCS) using a moving rudder and propeller. To accurately capture the interactions between the rudder and the propeller, they made use of delay detached eddy simulation (DDES), where the large coherent

structures are resolved and a RANS model is used near walls, to model the small-scale turbulence. Carrica et al. (2016) then improved the work done by including shallow water effects. Their results showed acceptable agreement with experimental data (below 2.7% for all self-propulsion relevant variables, and below 20% for overshoot angles and rudder yaw). Here again, use of scale-resolving simulations was made to better capture the rudder-propeller interactions. In all the above-cited work, extensive use of the overset technique was made to produce high-quality grids, combining Cartesian meshes for the domain and free surface refinement with  $O$  type meshes for the ship and the propeller. Finally, Shen and Korpus (2015) completed the effort done in free-running simulations by including the ability to simulate manoeuvres in waves. They performed 6 DOF computation on the ONR tumblehome (ONRT) model, in head and quartering seas. Very good agreement was found with ship motion data in head seas, with the increased complexity of quartering seas, notable differences in the results were observed, especially for the roll motion.

While the agreement with experimental data is usually excellent, those simulations are performed using very large meshes, up to 70 million cells, to fully resolve all flow features and use advanced computational strategies such as DDES. This does not allow free-running simulations to be integrated into the design with the computational power available nowadays to naval architects.

Captive model simulations replicate static drift, planar motion mechanism (PMM) in pure sway or pure yaw and rotatory arm test in a numerical environment. Static drift simulations differ from resistance computations only because of the drift angle ( $\beta$ ) imposed on the model. They are performed to find the sway velocity dependent ( $Y_v$ ,  $N_v$ ) force and moment coefficients (Hajivand and Mousavizadegan, 2015; Simonsen et al., 2012; Turnock et al., 2008) for example.

The drift angles considered usually range from  $\pm 20^\circ$  with Froude number ( $Fr$ ) in the range of 0.05-0.25, corresponding to the approach speed of the ship. In most simulations, it is observed that, as the drift angle is increased beyond  $\beta \sim 8^\circ$ ,  $Y$  becomes non-linear,  $N$  also becomes non-linear as drift angles are increased, but this is not as pronounced as for  $Y$ . Duman and Bal (2016), Kim et al. (2015), and Simonsen et al. (2012) all observed this behaviour, despite performing the simulations on different models. Where the force and moment become non-linear is also where the agreement between the numerical predictions and the experimental data starts to deteriorate (Duman and Bal, 2016; Kim et al., 2015). As opposed to static model tests, where the sway velocity can be varied by either changing the drift angle of the model or the forward velocity ( $v = -U_0 \sin \beta$ ), the usual practice in static drift simulations is to vary the drift angle and not the speed of the model. This removes the problems associated with the mesh dependence to the Reynolds number ( $y^+$ ) otherwise created.

While rotating arm tests are prohibited due to the required facility, they can be easily performed numerically. Toxopeus et al. (2013) executed rotating arm simulations on the KVLCC2 using a circular domain and time-varying boundary conditions. They compared results with conventional PMM simulations. Unfortunately, no conclusion can be drawn regarding the best approach as some simulations took the tank wall into account and the turbulence model used also varied.

To derive the linear and rotatory velocity and acceleration dependent forces and moment coefficients, planar motion mechanism simulations (in pure sway and yaw) are used. Many examples can be found in the literature, He et al. (2016), Kim et al. (2015), and Oldfield et al. (2015). Pure sway PMM allow the sway velocity and acceleration derivatives ( $Y_v$ ,  $N_v$ ,  $Y_{\dot{v}}$ ,  $N_{\dot{v}}$ ) to be determined while PMM in pure yaw provide the rotatory dependent derivative ( $Y_r$ ,  $N_r$ ,  $Y_{\dot{r}}$ ,  $N_{\dot{r}}$ ). Agreement with linear derivatives is usually acceptable, but discrepancies are present for higher order ones. It is also notable that pure yaw PMM result in much weaker agreement with experimental data, see He et al. (2016) and Kim et al. (2015) for examples. The increased complexity of the pure yaw PMM is the result of a complex flow pattern forming around the model, and is thus more non-linear than the pure sway case. Despite the increased complexity for this particular case, the captive approach is much more practical than the free-running one to determine the manoeuvring characteristics of the ship during the design, due to the lower computational cost. It also then allows a wide range of manoeuvres to be simulated using the derived coefficients, as opposed to the free-running approach, where only the results for one manoeuvre are obtained.

## 2.2 Mesh Motion

Mesh motion can be achieved either by deforming a single mesh or by imposing motion to a part of the mesh (overset or chimaera approach). For example, Turnock et al. (2008) used a weighted (or spring analogy) mesh deformation approach to simulate pure sway PMM on the KVLCC2. This method has the advantage of being easy to set-up but large mesh motions are prohibited, this might be the reason why pure yaw PMM were not considered in the example given.

Sakamoto and Kume (2014) used the overset technique to achieve the desired motion during their PMM in pure sway and yaw simulations. Because it allows for an unlimited range of motion, the overset mesh technique is the most commonly used in PMM simulations. It also removes all issues which can arise when cells are deformed, as opposed to the morphing approach. Overset techniques are of particular interest when new components (such as rudders, propellers, etc.) are added to the domain as there is no need to re-mesh it. However, it is unclear if any of the two approaches has an advantage in terms of accuracy and computational time.

## 2.3 Mathematical Model

To relate the global force and moment measured on the model to the corresponding velocities and accelerations, mathematical models are used. There is a vast number of mathematical models which can be employed. Integrated models, such as Abkowitz, express the global forces and moments as a function of  $u$ ,  $v$ ,  $r$ ,  $\dot{u}$ ,  $\dot{v}$ ,  $\dot{r}$ ,  $\delta$  and expand each expression as a Taylor series about an equilibrium condition (Abkowitz, 1964). The corresponding coefficients are then found by measuring the in- or out-of-phase forces and moments. Modular models decompose the forces acting on the ship in contribution from the hull, rudder and propeller. The forces acting on the hull are then expressed as a polynomial function of  $v$  and  $r$  (Yasukawa and Yoshimura, 2015). A least-square approach is usually used to find the corresponding coefficients for the forces and moments. Appendages contributions are usually added following empirical or first principle methods.

## 2.4 Free Surface

One of the critical aspects of these simulations is to model the free surface accurately. Many different methods are used. For low Froude numbers, a double body approach is often employed to reduce computational cost. Zou et al. (2010) used this method to simulate the flow around the KVLCC2 at different drift angles ( $0\text{-}6^\circ$ ) and water depth ratios ( $h/T \sim 1.2\text{-}8.3$ ) at a Froude number of 0.064. While the results for the deep water case showed acceptable agreement with experiments, the accuracy for the shallow water cases was lower, typically underestimating the results by  $\sim 10\%$ . Although the double body approach could be an acceptable assumption in deep water, shallow water effects may have too much influence on the wave field, resulting in the observed low accuracy of those simulations.

Two classes of methods are used in free surface modelling, they are referred to as: interface-tracking and interface-capturing. Interface-tracking methods deform the mesh to follow the position of the free surface. They are more commonly used on Cartesian structured grids as they allow for a reduction in the number of grid points but require a re-meshing at each time-step. They are also less accurate when non-linear free surface effects, such as wave breaking, occur. Interface-capturing methods track the position of the free surface on the grid by defining a transport equation for the different phases. Different implementations are available, the two most common are; the volume-of-fluid (VOF) approach (He et al., 2016; Kim et al., 2015) and the level set (LS) formulation (Hochbaum and Uharek, 2014; Hochbaum and Vogt, 2002); the latter having the advantage of smoothly varying, while the VOF approach results in a discontinuous interface (Ferziger and Peric, 2012), which can lead to some numerical issues (excessive smearing, etc.).

To conclude their study, Shenoi et al. (2013) discussed that the accuracy of manoeuvring

simulations could be enhanced by accounting for the free surface, especially for higher order derivatives. However, their study did not include a grid dependence study. This would indicate if the discrepancies with the data observed are the result of discretization errors, or in fact of modelling errors.

To avoid reflection of the waves on the boundaries, numerical damping is required. Gallagher et al. (2009) recommended the use of a body force term added to the Navier-Stokes equations to dampen the waves away from the model. A similar result can be achieved by aggressively coarsening the mesh near the boundaries (ITTC, 2017); although this approach is easier to implement, reflections can occur inside the domain if the coarsening is too aggressive.

## 2.5 Turbulence Closure

Turbulence closure provides perhaps the most important choice in CFD simulations. As discretization and iterative errors can be estimated and controlled, one of the remaining unknown is the choice of the turbulence model. The literature describing the differences between models is vast, see Pope (2001) and Wilcox (1993). The choice of turbulence model is a flow-specific problem. In their guidelines for the application of CFD in marine hydrodynamics, Gallagher et al. (2009) recommended investigating the turbulence model sensitivity of the simulation, as one would do with the mesh size. The ITTC (2011) guidelines for ship CFD applications give an overview of the turbulence model used in ship hydrodynamics, with the  $k-\omega$  being the preferred choice for both steady and unsteady marine applications.

Linear turbulence viscosity model such as Spalart-Allmaras,  $k-\epsilon$  and  $k-\omega$  are mostly used. Turnock et al. (2008), Duman and Bal (2016) and Simonsen et al. (2012) all used the shear stress transport formulation of the the  $k-\omega$  model (*SST*) proposed by Menter (1994) which blends a standard  $k-\epsilon$  model used in the free-flow with a  $k-\omega$  model in the boundary layer (it also uses a new formulation of the eddy viscosity). This allows the sensitivity to the turbulent quantity at the inlet of the standard  $k-\omega$  model to be removed and increases the performance in predicting boundary layer separation compared to the standard  $k-\epsilon$  model. For simulations where separation is more likely to occur, Menter's formulation of the  $k-\omega$  model can be expected to give more accurate results.

More advanced turbulence models are also used. For example, Toxopeus et al. (2013) compared the results obtained from experimental flow measurements on the KVLCC2 with results from numerical simulations using both linear ( $k-\omega$  *SST*) and non-linear (Explicit Algebraic Stress Model (EASM)) turbulent viscosity models. The results showed that the linear viscosity models can accurately predict the forces and moments, but differences are present in the details of the flow (i.e. vortex core strength).

Abdel-Maksoud et al. (2015) compared PIV wind tunnel results for the same ship at a

**Table 2.1:** Range of benchmark data from NMRI for the KVLCC2.

Test	$Fr$ [-]	$\beta$ [°]	$y_0$ [m]	$\gamma$ [-]	T [s]
Static Drift	0.142	$\pm 16$	-	-	-
Pure Sway	0.142	-	0.2026	0	6 - 12
Pure Yaw	0.142	-	<i>varies</i>	0.4	6 - 12

drift angle of 30° to numerical simulations using different turbulence models and numerical methods, such as delayed detached eddy simulation (DDES) or large eddy simulation (LES). While better insight of the flow field is gained by resolving more of the turbulent energy spectrum, such methods do not result in practically significant improvement in ship manoeuvring predictions.

## 2.6 Verification and Validation

To assess the accuracy of a numerical prediction, verification and validation (V&V) is required. To address this, Stern et al. (2001) proposed a method to assess the numerical uncertainty in CFD simulations for marine applications. The method relies on a mesh sensitivity approach to estimate the discretization error. The validation of the simulations performed relies on extensive model test data. For the 2014 SIMMAN workshop, three ships were extensively tested by different contributors, and the results published, as shown in table 1.1.

Experimental data for both the KVLCC2 and the DTMB-5415 is widely available, both for bare hull and appended models. For this study, the KVLCC2 is preferred, as it features a more conventional and simpler hull shape (no sonar dome). In addition, for SIMMAN 2019, the DTMB-5415 model will be replaced, whereas the KVLCC2 will be kept. The National Maritime Research Institute (NMRI) provides raw force measurements for static drift and PM simulations via the SIMMAN (2014) workshop; this data was used for the validation.

## 2.7 Conclusion on Background

This survey of the literature highlighted the most common practices and strategies used in numerical ship manoeuvring. While rotating arm tests become attractive numerically, some difficulties associated with the domain and boundary conditions required make them less compelling than static drift simulations. Static drift simulations are also more similar to PMM simulations, in the sense that the domain and mesh will share some similarities. Another issue is how the CFD software deals with rotating frame of reference, this might

not be available in all commercial code, it is therefore easier to replicate static drift tests.

Some of the studies presented previously relied on the double body approach to limit computational cost, however, few undertakers pointed out the limitations of such approaches. It seems appropriate to capture the free surface in this study, using the VOF method, to gain more physical fidelity. Regarding turbulence closure, the  $k-\omega$  SST turbulence model is the most widely used, it is therefore the obvious choice as the standard model for this investigation.

Regarding the software package, Star-CCM<sup>+</sup>, is by far the most utilized commercial CFD package and is therefore an obvious choice. Finally, the overset mesh method is preferred to morphing as it is aimed to simulate PMM in pure yaw for this study and it is not clear if morphing can cope with such deformation.

# Chapter 3

## Mathematical Model

This chapter provides the background theory used in the numerical simulation of ship manoeuvring used throughout this thesis. The coordinate system and the governing equations of ship manoeuvring are introduced. Then, the static drift and planar motion mechanism motions are described. Finally, the governing equations of viscous flow are presented.

### 3.1 Coordinate System and Nomenclature

Two different coordinate systems are used in ship manoeuvring. A ship-fixed coordinate system ( $oxyz$ ), fixed to the hull at the origin ( $o$ ) and a space-fixed (*inertial*) coordinate system ( $OXYZ$ ). For consistency with the experimental data available, the origin for the ship-fixed coordinate system is taken at midship, and not at the centre of gravity, for all simulations presented herein. The motions of the ship-fixed coordinate system are expressed relative to the space-fixed coordinate system.

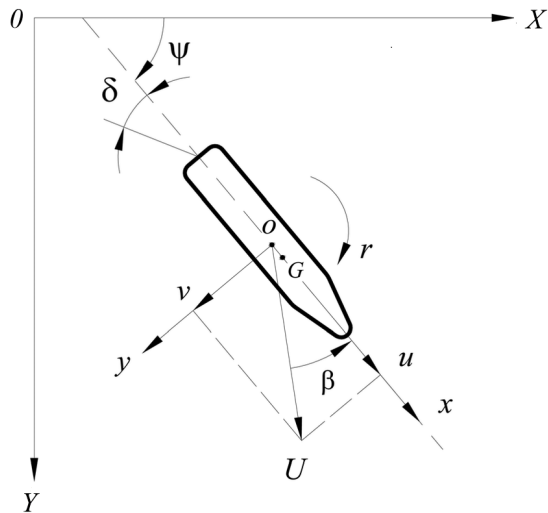


**Figure 3.1:** Space and ship-fixed coordinate system. Adapted from Luo et al. (2016).

In the ship-fixed coordinate system,  $x$  is pointing forward,  $y$  to starboard and  $z$  downwards. The origin of the space-fixed coordinate system is usually taken as lying on the undisturbed free surface. A positive yaw angle  $\psi$  is therefore defined as a *clockwise* rotation of the ship in the space-fixed coordinate system. Similarly, a positive drift angle  $\beta$  corresponds to the flow coming from starboard.

For captive model tests or numerical simulation of captive model tests, forces and moments are expressed in the ship-fixed coordinate system. They are made nondimensional following the notation introduced in the *Dimensionless Quantities*.

### 3.2 Equations of Motion

Considering only 3 degrees of freedom, the equations of free-motion in surge, sway and yaw for a body whose axis coincide with the principal axis of symmetry are (see Lewis (1989) for the complete derivation)

$$\begin{aligned} X &= m(\dot{u} - rv - x_G r^2) \\ Y &= m(\dot{v} + ru + x_G \dot{r}) \\ N &= I_z \dot{r} + mx_G(\dot{v} + ru), \end{aligned} \tag{3.1}$$

where use of  $r \equiv \psi$  and  $\dot{r} \equiv \ddot{\psi}$  has been made. The terms on the left hand side represent the hydrodynamic forces and moments. Under the assumptions of small disturbances, they can be expanded as a first order Tylor series with kinematic parameters

$$\left. \begin{array}{l} X \\ Y \\ N \end{array} \right\} = f(u, v, r, \dot{u}, \dot{v}, \dot{r}). \tag{3.2}$$

After simplification and linearization with considerations such as ship symmetry, constant forward speed, etc. the symmetric and antisymmetric fluid action can be combined with equation 3.1 to yield

$$\begin{aligned} -X_u(u - U) + (m - X_{\dot{u}})\dot{u} &= 0 \\ Y_v v + (Y_{\dot{v}} - m)\dot{v} + (Y_r - mu)r + (Y_{\dot{r}} - mx_G)\dot{r} &= 0 \\ N_v v + (N_{\dot{v}} - mx_G)\dot{v} + (N_r - mx_G u)r + (N_{\dot{r}} - I_{zz})\dot{r} &= 0, \end{aligned} \tag{3.3}$$

where  $X_u$ ,  $Y_v$ ,  $N_v$ ,  $Y_r$ ,  $N_r$ ,  $X_{\dot{u}}$ ,  $Y_{\dot{v}}$ ,  $N_{\dot{v}}$ ,  $Y_r$ ,  $N_r$  are the so-called slow motion derivatives,  $m$  is the mass of the ship,  $I_{zz}$  is the moment of inertia in yaw and  $x_G$  is the distance from the centre of gravity to the origin of ship-fixed coordinate system, see figure 3.1. They account for centrifugal and inertial effects due to the origin of the ship-fixed coordinate system not being on the centre of gravity of the ship.

### 3.2.1 Static Drift

For ship is towed at a constant drift angle  $\beta$  and zero yaw rate  $r$ , the sway velocity can be expressed as

$$v = -U_0 \sin \beta, \quad (3.4)$$

and thus there is no accelerations ( $\dot{v} = \ddot{r} = 0$ ). The equations of motion simplify to:

$$\begin{aligned} Y &= Y_v v \\ N &= N_v v, \end{aligned} \quad (3.5)$$

where the hydrodynamic forces are only a function of the sway velocity. Measurement of the sway force and yaw moment for a range of sway velocities allow the manoeuvring derivative to be extracted by recording the gradient at the origin.

### 3.2.2 Planar Motion Mechanism in Pure Sway

For pure sway tests, under sinusoidal excitation, the transverse motion of the ship, expressed in the earth fixed coordinate system is given by, see Temarel (2017),

$$y(t) = -y_0 \sin(\omega t) \quad v(t) = -y_0 \omega \cos(\omega t) \quad \dot{v}(t) = y_0 \omega^2 \sin(\omega t), \quad (3.6)$$

where  $y_0$  is the sway amplitude, and  $\omega$  is the sway angular velocity. The motion is imposed such that the resulting angular velocity and acceleration are zero ( $r = \dot{r} = 0$ ) and the equations of motion simplify to

$$\begin{aligned} Y &= \tilde{Y}_v v + \tilde{Y}_{\dot{v}} \dot{v} \\ N &= \tilde{N}_v v + \tilde{N}_{\dot{v}} \dot{v}, \end{aligned} \quad (3.7)$$

implying that the hydrodynamic sway force and yaw moment are solely function of the sway velocity and acceleration. The coefficients  $\tilde{Y}_v$ ,  $\tilde{Y}_{\dot{v}}$ , etc., are the frequency dependent oscillatory coefficients. In the limit of infinitely small frequency of oscillations, they become the slow motion derivatives, for example for  $\tilde{Y}_v$ ,

$$\lim_{\omega \rightarrow 0} \tilde{Y}_v = Y_v. \quad (3.8)$$

The coefficients are obtained by measuring the in-phase components (proportional to  $\dot{v}$ ) and the out-of-phase (proportional to  $v$ ) components of the force and moment.

Throughout this thesis, when referring to frequency independent coefficients, the term *slow motion derivatives* will be employed, the use of *oscillatory coefficients* will be made to refer to frequency dependent coefficients and finally when both will be referred to, the term *manoeuvring derivatives* will be employed.

### 3.2.3 Planar Motion Mechanism in Pure Yaw

Pure yaw tests introduce an additional drift angle, so that the ship's centreline is always tangent to its path, resulting in zero sway velocity and accelerations ( $v = v' = 0$ ) in the ship-fixed coordinate system.

This is achieved by imposing a transverse displacement and a yaw angle in the earth-fixed coordinate system. To express the resulting velocity in the ship-fixed coordinate system, the transformation matrix  $\mathbf{T}$  is used, see Temarel (2017),

$$\mathbf{T} \begin{bmatrix} U \\ v_0 \\ 0 \end{bmatrix} = \begin{bmatrix} u \\ v \\ 0 \end{bmatrix} .$$

Assuming no heel and pitch ( $\theta = \phi = 0$ ) the matrix simplifies to

$$\mathbf{T} = \begin{bmatrix} \cos \psi & \sin \psi & 0 \\ -\sin \psi & \cos \psi & 0 \\ 0 & 0 & 1 \end{bmatrix} .$$

Thus in the ship-fixed coordinate system the surge and sway velocities are (ignoring heave)

$$\begin{bmatrix} u \\ v \end{bmatrix} = \begin{bmatrix} \cos \psi U & \sin \psi v_0 \\ -\sin \psi U & \cos \psi v_0 \end{bmatrix} .$$

The condition that ensures that the sway velocity, and thus sway acceleration, is zero in the ship-fixed coordinate system is

$$\sin \psi U = \cos \psi v_0 , \quad (3.9)$$

where the sway velocity has the form

$$v_0 = -y_0 \omega \cos (\omega t) . \quad (3.10)$$

Substitution of the previous equation in equation 3.9 gives the yaw angle

$$\psi = \tan^{-1} \left( \frac{-y_0 \omega}{U} \cos (\omega t) \right) , \quad (3.11)$$

which is more commonly expressed as

$$\psi \approx \tan^{-1} \left( \frac{-y_0 \omega}{U} \right) \cos (\omega t) = \psi_0 \cos (\omega t) . \quad (3.12)$$



The linear equations of motion therefore simplify to

$$\begin{aligned} Y &= \tilde{Y}_r r + \tilde{Y}_{\dot{r}} \dot{r} \\ N &= \tilde{N}_r r + \tilde{N}_{\dot{r}} \dot{r}, \end{aligned} \quad (3.13)$$

implying that the hydrodynamic sway force and yaw moment are solely function of the yaw rate and acceleration. The oscillatory coefficients are then obtained by measuring the in-phase components (proportional to  $\dot{r}$ ) and the out-of-phase (proportional to  $r$ ) components of the force and moment.

### 3.2.4 Rudder Contribution

The manoeuvring derivatives obtained for the hull with rudder can be decomposed in contribution of the undeflected rudder and the bare hull, taking the static drift as an example,

$$\begin{aligned} Y'_v &=_{R} Y'_v +_{BH} Y'_v \\ N'_v &=_{R} N'_v +_{BH} N'_v, \end{aligned} \quad (3.14)$$

where the subscripts  $R$  and  $BH$  represent the rudder and bare hull contributions, respectively. This assumes that there is no contribution to the acceleration dependent derivatives from the rudder. Similar expressions can be developed for the PMM case.

## 3.3 Viscous Flow

The motion of an incompressible Newtonian fluid is governed by the continuity and the Navier-Stokes equations, describing the conservation of mass and momentum, respectively. Note that for an incompressible flow, where the expected temperature changes are minimal, the energy conservation equation is de-coupled from the continuity equation and can be safely ignored. In a Cartesian coordinate system the continuity equation is

$$\frac{\partial \tilde{u}_i}{\partial x_i} = 0. \quad (3.15)$$

And the conservation of momentum, in non-conservative form

$$\rho \left[ \frac{\partial \tilde{u}_i}{\partial t} + u_j \frac{\partial \tilde{u}_i}{\partial x_j} \right] = - \frac{\partial \tilde{p}}{\partial x_i} + \mu \frac{\partial^2 \tilde{u}_i}{\partial x_j^2}, \quad (3.16)$$

where  $\tilde{u}_i$  represents the instantaneous  $i^{th}$  component of the velocity field and  $\tilde{p}$  the instantaneous pressure field (Einstein's summation convention has been employed).

The *Reynolds-Averaged Navier-Stokes* equations are obtained by performing Reynolds

decomposition of the instantaneous quantities  $\tilde{\phi}$  into a mean,  $\phi$  and a fluctuating part  $\phi'$

$$\tilde{\phi} = \phi + \phi'. \quad (3.17)$$

Therefore, the Reynolds-Average continuity and Navier-Stokes (RANS) equations are given by:

$$\frac{\partial u_i}{\partial x_i} = 0 \quad (3.18)$$

$$\rho \left[ \frac{\partial u_i}{\partial t} + u_j \frac{\partial u_i}{\partial x_j} \right] = - \frac{\partial p}{\partial x_i} + \mu \frac{\partial^2 u_i}{\partial x_j^2} - \rho \frac{\partial}{\partial x_j} \overline{u'_i u'_j}. \quad (3.19)$$

The appearance of the last term on the right-hand side, called Reynolds stresses, require additional equations to close the system. This is achieved using turbulence models.

### 3.4 Turbulence Closure

To provide closure to the RANS equations, the Reynolds stresses have to be determined. The most common approach is to use the Boussinesq hypothesis, which relates the Reynolds stresses to the mean flow strain-rate (in a similar way as Newton's law of viscosity) with the eddy/turbulent viscosity  $\mu_t$  used as a constant of proportionality. For an incompressible flow, it reads

$$\tau_{ij} = -\rho \overline{u'_i u'_j} = 2\mu_t S_{ij} - \frac{2}{3}\rho k \delta_{ij}, \quad (3.20)$$

where  $S_{ij}$  is the mean strain-rate tensor,  $k$  the kinetic energy of the turbulent fluctuation and  $\delta_{ij}$  is the Kronecker delta. Many different turbulence models can be used, the most common being the two-equation models, the  $k-\epsilon$  and  $k-\omega$  family, see 2.5. From the literature survey, it was determined that the Shear Stress Transport version (Menter, 1994) of the  $k-\omega$  turbulence model was mostly used in ship manoeuvring, both for steady and unsteady simulations. This is due to its ability to better capture flow separation compared to the  $k-\epsilon$  family, as well as being less sensitive to the turbulent quantities at the inlet than the standard  $k-\omega$ . It is also more stable than the  $k-\epsilon$  but is more computationally demanding.

This particular formulation of the  $k-\omega$  turbulence model is available in Star-CCM<sup>+</sup> (Siemens, 2017) and used for all simulations throughout this thesis, unless otherwise stated. It solves two transport equations, one for the turbulent kinetic energy  $k$

$$\frac{Dk}{Dt} = \tau_{ij} \frac{\partial u_i}{\partial x_j} - \beta^* \rho \omega k + \frac{\partial}{\partial x_j} \left[ (\mu + \sigma_{k1} \mu_t) \frac{\partial k}{\partial x_j} \right], \quad (3.21)$$

and one for the specific dissipation rate,  $\omega$ ,

$$\begin{aligned} \frac{D\rho\omega}{Dt} = & \frac{\gamma}{\nu_t} \tau_{ij} \frac{\partial u_i}{\partial x_j} - \beta \rho \omega^2 + \frac{\partial}{\partial x_j} \left[ (\mu + \sigma_\omega \mu_t) \frac{\partial \omega}{\partial x_j} \right] \\ & + 2\rho(1 - F_1) \sigma_\omega \frac{1}{\omega} \frac{\partial k}{\partial x_j} \frac{\partial \omega}{\partial x_j}, \end{aligned} \quad (3.22)$$

where  $\tau_{ij}$  is the Reynold's stress tensor. A blending function,  $F_1$ , is used to calculates the new model constants  $\phi$  from the constant  $\phi_1$  and  $\phi_2$  depending on the wall distance

$$\phi = F_1 \phi_1 + (1 - F_1) \phi_2. \quad (3.23)$$

The constant of set  $\phi_1$  are for the  $k-\omega$  SST model

$$\begin{aligned} \kappa &= 0.41 & \beta^* &= 0.09 & \beta_1 &= 0.0750 & \sigma_{k1} &= 0.85 \\ \sigma_{\omega 1} &= 0.5 & a_1 &= 0.31 & \gamma_1 &= \beta_1/\beta^* - \sigma_{\omega 1} \kappa^2 / \sqrt{\beta^*} \end{aligned} .$$

The constant of set  $\phi_2$  are the same as for a standard  $k-\epsilon$  model. For the full description of all the other constants and functions used with the  $k-\omega$  turbulence model, refer to appendix B.1.

### 3.5 Volume of Fluid

The Volume of Fluid (VOF) approach as proposed in Hirt and Nichols (1981) is used to capture the free surface. It defines a transport equation for the evolution of the volume fraction of fluid  $\alpha_i = V_i/V$

$$\frac{\partial \alpha_i}{\partial t} + u_i \frac{\partial \alpha_i}{\partial x_i} = 0, \quad (3.24)$$

with constrain

$$\sum_{i=1}^n \alpha_i = 1. \quad (3.25)$$

The volume function is tracked in every cell of the domain, cells with values of  $\alpha_i = 0$  are called empty, cells with values of 1 are full and when  $0 < \alpha_i < 1$ , there is a fluid interface in the cell.

The two fluids are considered as a single effective fluid whose properties vary according to the volume fraction of individual fluid cells

$$\rho = \rho_1 \alpha_i + \rho_2 (1 - \alpha_i) \quad \mu = \mu_1 \alpha_i + \mu_2 (1 - \alpha_i). \quad (3.26)$$

Thus the continuity and Navier-Stokes equations are solved for the effective fluid, and the interface is simply defined as the location where rapid changes in fluid properties are observed (Ferziger and Peric, 2012).

To avoid the smearing at the free surface resulting from the discretization of the convective term in the transport equation when using standard schemes, high-order schemes are often used. For example, the High Resolution Interface Capturing method (HRIC) (Muzaferija, 1998) or the Compressive Interface Capturing Scheme for Arbitrary Meshes (CICSAM)(Ubbink and Issa, 1999).

# Chapter 4

## Methodology

This chapter details the methodology used to set-up the static drift and planar motion mechanism simulations. First, the static drift simulations are introduced, the domain and mesh generation processes and the numerical solutions are detailed. Similar explanations are then provided for the planar motion mechanism simulations. Finally, the verification and validation procedure is presented.

All numerical simulations were undertaken using CD-Adapco's Star-CCM<sup>+</sup> version 12.04.11. using double precision. Static drift simulations were undertaken on the *Lyceum 2* student cluster at the University of Southampton, while the PMM simulations used the *IRIDIS 4* supercomputer.

### 4.1 Static Drift Simulations

Static drift simulations consist of measuring sway force and yaw moment for different sway velocities. This is achieved by towing the model at different drift angles and constant forward speed ( $Fr = 0.142$ ). The drift angles considered are based on the available experimental data and are: -16°, -8°, -4°, 0°, 4°, 8°, 16°.

#### 4.1.1 Domain

To solve the flow around the ship, a proper domain is required. Its size will govern the number of cells used and thus the computational time.

For manoeuvring simulations, the ITTC (2017) recommend using 3-5 ship lengths in the longitudinal direction, 2-3 ship lengths in the transverse direction and a ship length in the vertical direction. Adequate refinements are required in areas of rapid flow changes, i.e. at the free surface, on the ship's surface and in its wake. Because drift angles are considered, the half-body approach cannot be used in ship manoeuvring.

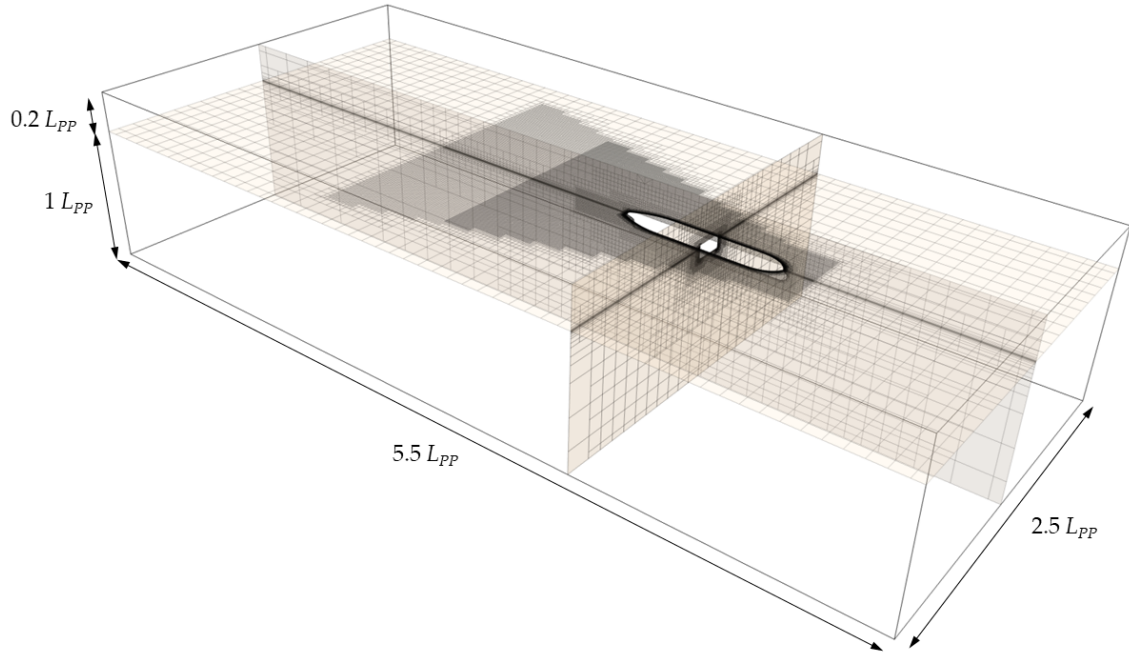


**Figure 4.1:** Computational domain for the static drift simulations. Note the mesh refinement in way of the free surface and the two levels refinement for the Kelvin wave pattern.

The domain was defined following the prior recommendations. The model hull file (.igs) was provided by SIMMAN (2014). The final domain extends 1.5 lengths in front, 3 lengths behind the model, 2.5 model lengths are used in the transverse direction, and 1 model length in depth. The top boundary is placed 0.2 model length above the undisturbed free surface. The domain dimensions are depicted in figure 4.1.

#### 4.1.2 Mesh

Using the automatic mesh generation capability of Star-CCM<sup>+</sup>, an unstructured hexahedral mesh of the whole domain was generated. This approach was chosen as it produces better quality meshes than polyhedral or tetrahedral meshes, by providing more control on the skewness and aspect-ratio of the cells. Unstructured hexahedral meshes are also particularly attractive for free surface flows as the grid lines are running parallel to the surface, rendering the capturing operation easier. The local refinements required are also easily added.

Structured meshes are typically not used for ship manoeuvring as the computational efficiency gained does not justify the additional pre-processing time required.

To minimise the number of cells in the simulations, a wall function approach was chosen to model the boundary layer. This requires proper placement of the first cell on the model. A  $y^+$  target value of 30 was chosen, in accordance with the wall function approach. An

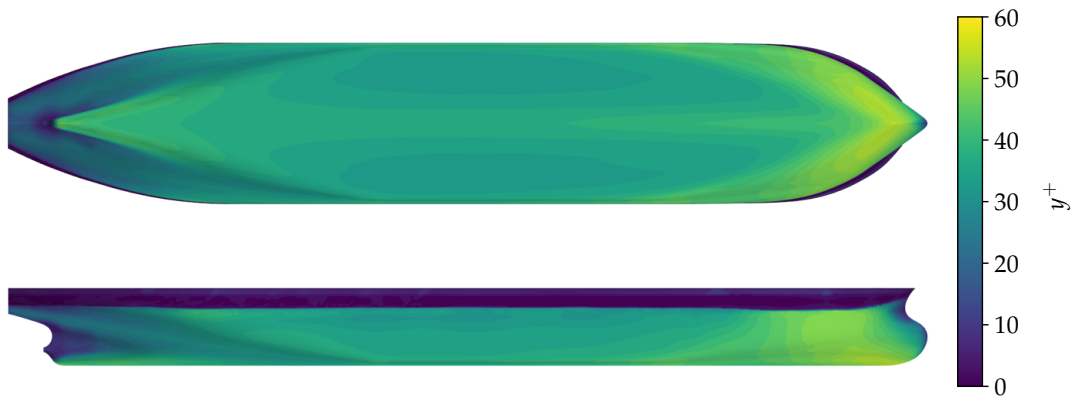


**Figure 4.2:** Bottom and profile view of the non-dimensional wall distance ( $y^+$ ) on the KVLCC2 for the static drift simulation ( $\beta = 0^\circ$ ,  $Fr = 0.142$ ).

empirical method (see appendix C.1) was used to determine the first cell height based on the expected Reynolds number of the simulation. This enabled a preliminary case to be solved to adjust for this crude estimate. The final  $y^+$  on the ship is presented in figure 4.2. The boundary layer mesh was achieved using a prism layer on the surface of the model.

This prism layer must also contain enough cells in the normal direction to properly resolve the boundary layer. Typically, 10 cells are recommended (ITTC, 2017). Boundary layer theory can be used to estimate the boundary layer depth based on flat-plates formula, see appendix C.1. The growth rate and total thickness of the prism layer were thus adjusted to match the required boundary layer depth, the number of cells in the normal direction and first cell height ( $y^+$ ). This ensured that the wall approach requirements were respected and that sufficient cells were used to model the boundary layer.

The Kelvin wake pattern is a distinctive feature of surface ships. To properly capture it, a global free surface refinement was applied to the whole domain, clustering 10 cells in the expected wave amplitude (calculated using empirical methods and later refined, see appendix C.2). Two additional refinements were applied in the wake of the ship. A first Kelvin wake refinement, extending  $2 L_{PP}$  downstream of the hull with an additional 5 cells in the expected wave height, and a finer Kelvin wake refinement, extending  $1 L_{PP}$  downstream of the hull, and totalling 20 cells in the vertical direction, as recommended by ITTC (2017). In addition to vertical refinements, horizontal refinements were also added at the free surface. They were applied to achieve an aggressive grid coarsening on the edge of the two Kelvin wake refinements to act as a wave damper. Again an empirical method was used to determine the required longitudinal and transverse grid spacing, see appendix C.2.

To capture the viscous wake generated by the ship, another refinement was applied underwater, extending  $1/2 L_{PP}$  downstream of the ship. Finally, refinements were applied on the bow and stern of the ship, as well as on the turn of the bilge, to capture the different

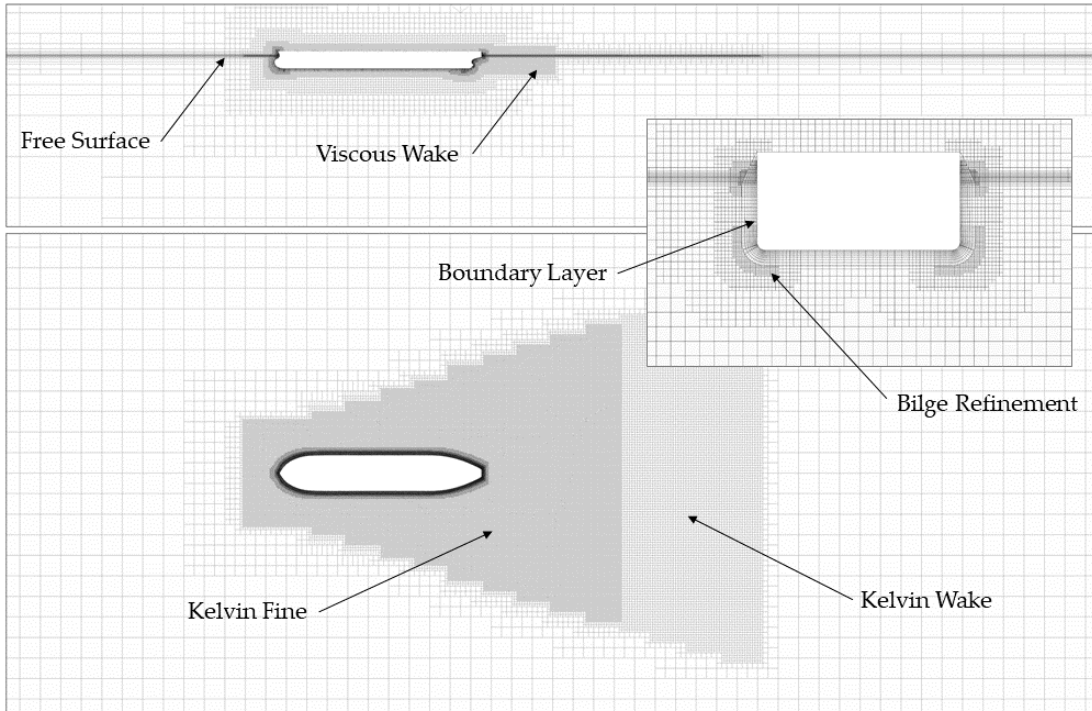


**Figure 4.3:** Global view of the standard mesh refinements used for the static drift simulations ( $\beta = 0^\circ$ ,  $Fr = 0.142$ ) together with details of the refinements around the model.

bilge vortices generated. The final mesh is depicted in figure 4.3. The total cell count is 3.4 million. This mesh will be used as the standard mesh for all following simulations. The mesh independence of the solution was tested, see section 4.3

To obtain the desired drift angle, the model was rotated inside the domain, with all relevant mesh refinements. This ensured that the Kelvin and the viscous wake refinements were adequately positioned downstream of the model regardless of the drift angle imposed. A Star-CCM<sup>+</sup> macro was written to automate the re-meshing process of the domain for the different drift angles, see appendix C.8.

#### 4.1.3 Numerical Solution

Many problems with a steady solution can be solved as unsteady problems until a steady state solution is achieved. For ship hydrodynamics, both approaches are valid if the free surface is not accounted for. However, when the free surface is modelled an unsteady approach is required.

To reach a quasi-steady solution for the static drift simulations, the momentum and continuity equations are solved using an *Implicit Unsteady* method, where the momentum

equation is advanced in time using an implicit approach. The governing equations are solved using the *Segregated Flow solver*. This solver uses the SIMPLE (Semi-Implicit Method for Pressure Linked Equations) algorithm to obtain a solution to the momentum and continuity equation at the next time-step ( $n+1$ ). First, the new velocity field is obtained by solving the linearised momentum equation at the present time-step, then, to ensure that the velocity field is divergence-free (satisfies continuity), the velocity field is corrected using a discrete Poisson equation for the pressure. The resulting velocity field does not satisfy the momentum equation, the procedure is therefore repeated until an acceptable level of convergence is obtained. These are called *inner iterations*. For a thorough review of the SIMPLE scheme, see Ferziger and Peric (2012).

Careful considerations have to be made regarding the choice of time-step and inner iterations. Shorter time-steps will require fewer inner iterations to maintain an acceptable computational time while larger time-steps will lose some of the physics, especially as the free surface is considered. A balance must be found.

Perhaps the best method to determine the correct time-step/inner iteration combination is to use the *Courant–Friedrichs–Lewy* condition (CFL), which guarantees stability of numerical schemes

$$\text{CFL} = \frac{u\Delta t}{\Delta x} \leq 1. \quad (4.1)$$

This can be used to determine the maximum time-step allowed for stability, knowing the mesh size and flow velocity. With an average mesh size in the domain of 0.05 m, the maximum time-step to achieve a Courant number below 1 is 0.06 s, with a model speed of 0.76 m/s.

Within Star-CCM<sup>+</sup>, a High Resolution Interface Capturing scheme (HRIC) is used at the free surface. This requires additional considerations for the time-step. Threshold values of the local CFL ( $C_{u_l}$  and  $C_{u_u}$ ) are specified, below  $C_{u_l}$ , the HRIC scheme is used, above  $C_{u_u}$ , an upwind-difference (UD) scheme is used. A blending function is applied for CFL values in-between. Convergence can be promoted by lowering the values of this threshold which will use the UD sooner, this will however result in excessive numerical dissipation at the free surface. For problems which have a steady-state solution, large values are recommended, ensuring the HRIC scheme is used irrespectively of the time-step selected (Siemens, 2017).

It is recommended (ITTC, 2011) that the simulation is progressed so that the wave pattern can run around 10 ship lengths during the simulation. This results in a minimum physical time of around 40 s. Upon analysis of preliminary simulations, it was determined that this time was not long enough to obtain converged results, see figure 4.5. A physical time of 100 s is therefore chosen for the static drift simulations. This allows the last 10 s to be time-averaged to obtain the forces and moments. With this physical time,

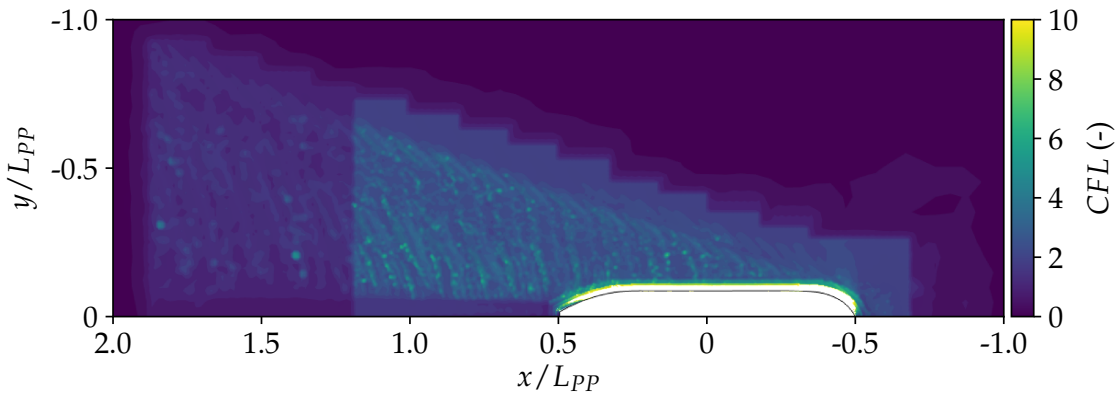


**Figure 4.4:** CFL number at the free surface for the static drift simulation ( $\beta = 8^\circ$ ,  $Fr = 0.142$ ). Note that close to the ship the CFL cannot be kept to the desired values due to the size of the cells, viewed from above.

the chosen time-step is 0.05 s, with 10 inner iterations, for a total of 20 000 iterations per simulation ( $\sim 300$  CPU hours). This time-step also respects the requirements for the Courant number. To ensure that the HRIC scheme is used at the free surface, the threshold values are increased to 5 and 10 for  $C_{u_l}$  and  $C_{u_u}$ , respectively. The time-step sensitivity of the solution was examined, see section 5.1. All solver parameters used are presented in table 4.1.

Under-relaxation factors are used to multiply the velocity field obtained at the end of a time-step to initialize the computation of a new time-step. Following recommendations from Siemens (2017) regarding batch jobs, the default under-relaxation factors were used.

#### 4.1.4 Boundary Conditions

To capture the viscous stresses on the ship, the no-slip condition was applied. An *all y+* wall treatment approach was used to resolve the boundary layer (appropriate with the use of the  $k-\omega$  SST turbulence model). In this method, the velocity profile is expressed as a blended function between the log-law and the resolved velocity profile, depending on the local  $y^+$  value. This approach is particularly attractive in this case as it is difficult to achieve a uniform  $y^+$  on the model, see figure 4.2. No roughness corrections were applied.

The default turbulent quantities at the inlet were used, this corresponds to a low level of background turbulence in the flow. For manoeuvring tests in a towing tank, those values are not expected to be large. Moreover, the formulation of the  $k-\omega$  turbulent model used has a low sensitivity to the turbulent inlet quantities (this is the reason for its development). The shear stress specification on the walls of the tank and the deck of the model were set to the slip condition. Table 4.2 summarizes all the different boundary conditions used.

The kinematic boundary condition is not applied directly to the free surface. However,

**Table 4.1:** Implicit unsteady and segregated solver parameters for the static drift simulations.

Property	Value	Comment
Time-step	0.05s	Sensitivity examined
Inner iteration	10	
Temporal discretization	$2^{nd}$ order upwind	
Convective discretization	$2^{nd}$ order upwind	
$C_{u_l}$	5.0	
$C_{u_u}$	10.0	
URF <sub>velocity</sub>	0.8	default
URF <sub>pressure</sub>	0.2	default
URF <sub>SF</sub>	0.9	default
URF <sub><math>k-\omega</math></sub>	0.8	default
URF <sub><math>\mu_t</math></sub>	1.0	default

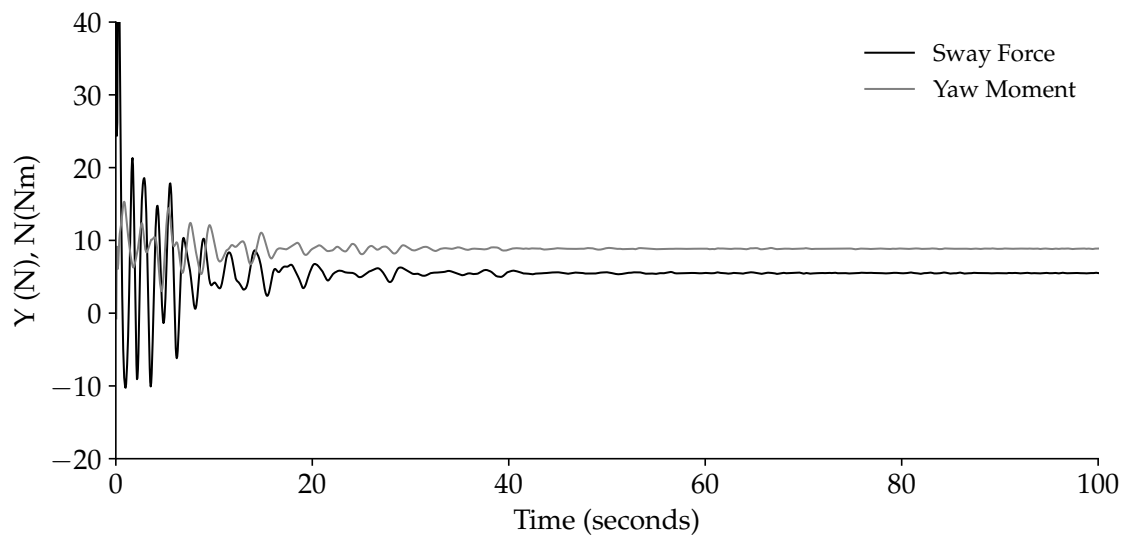


**Figure 4.5:** Time-history of the sway force and yaw moment during a static drift simulation using the standard mesh, ( $\beta = 8^\circ$ ,  $Fr = 0.142$ ).

**Table 4.2:** Boundary conditions for the static drift simulations.

Boundary	Quantity	Value
Inlet	-Turbulence Intensity	0.01
	-Turbulent Viscosity Ratio	10.0
	-Velocity	Wave <sup>1</sup>
	-Volume Fraction	Wave <sup>1</sup>
Outlet	-Turbulence Intensity	0.01
	-Turbulent Viscosity Ratio	10.0
	-Pressure	Wave <sup>1</sup>
	-Volume Fraction	Wave <sup>1</sup>
Hull	-Shear Stress	No-Slip
Deck	-Shear Stress	Slip
Tank Walls	-Shear Stress	Slip

<sup>1</sup> Star-CCM<sup>+</sup> uses flat-water waves when using the VOF model to specify the velocity, hydrostatic pressure and volume fraction at the boundaries.

the solution to the VOF implies that it is satisfied (it also implicitly satisfies the dynamic boundary condition)(Ferziger and Peric, 2012).

#### 4.1.5 Additional Investigations

Additional investigations have been undertaken, namely the double-body approach, and a method where the speed of the model was altered to obtain the desired sway velocity (as opposed to changing the drift angle).

The double-body approach was used to investigate the influence of modelling the free surface. The domain was cut at the free surface and the symmetric boundary condition applied to the newly created boundary. The mesh refinements were kept the same as in the standard simulations, except for the free surface refinements, which were omitted. The viscous wake refinement was enlarged to provide an additional global refinement around the hull and in the wake of the model. A steady approach was used to solve the simulation, with a total of 5000 iterations (iterative convergence was observed after 1000). The resulting cell count was 2.71 M.

The second investigation used the standard mesh (generated for a drift  $\beta = 8^\circ$ ) but adjusted the forward speed of the model such that the resulting sway velocity matched that of the static drift test at  $\beta = 4^\circ$ . No adjustment to the standard mesh, solver parameters, etc., were made.

The influence of the rudder was also considered. To reduce the number of simulations required, only the undeflected condition was considered. The rudder geometry was also

simplified, instead of featuring a rudder horn, the profile was extended to the surface of the hull, thus creating a larger rudder but greatly simplifying the mesh. The rudder uses a standard NACA 0018 section. The geometry, as well as its position on the model, are available from SIMMAN (2014). The addition of the rudder increased the cell count by 0.1 M based on the standard mesh. The solver parameters, turbulence closure, etc., are equivalent to the standard simulation described previously. The drift angles considered are limited to 16, 8, 4 and 0 degrees. The excellent symmetry obtained for the bare hull simulations comforted the author in the adequacy of this choice.

## 4.2 Planar Motion Mechanism Simulations

Preliminary PMM simulations showed instabilities in the form of oscillations on the free surface. The exact cause of those instabilities could be threefold; the free surface was not exactly aligned with gridlines, the solution initialisation, and especially the motion, caused waves to be generated and those waves reflected against the walls, or finally, the non-conservatism of overset interpolation caused the solution to be unstable.

A release and ramp time were applied to try to mitigate those effects but because they only delay the computation of the forces on the model and not the start of the motion, no improvements were observed. The wave damping function proposed by Choi and Yoon (2009) was also used to try to reduce the oscillations but without great success.

The method which provided the best results was to simulate a straight-ahead tow, without imposing any motion, until the solution had settled ( $L_2$  norm in the pressure change below  $5.0 \times 10^{-4}$ , see section 4.3), and then using the results obtained to initialize the PMM simulations. This completely removed the oscillations on the free surface (see appendix C.7), as well as helping the solution reach an harmonic state quicker, see figure 4.6. This approach was adopted to set-up all PMM simulations.

### 4.2.1 Domain

The domain size used for the planar motion mechanism simulations was the same as for the static drift simulations, with the addition of the overset, which is described in the next section, see figure 4.7.

### 4.2.2 Overset Mesh

Overset meshes are used to discretize a domain where different meshes overlap. In this case, it allows a part of the mesh, the overset, to move inside the background domain. During the overset process, a hole in the background mesh is created using the overset. The resulting cells are then grouped in the following categories; (1) inactive, (0) active, (-1) acceptor and (-2) acceptor used as a donor.

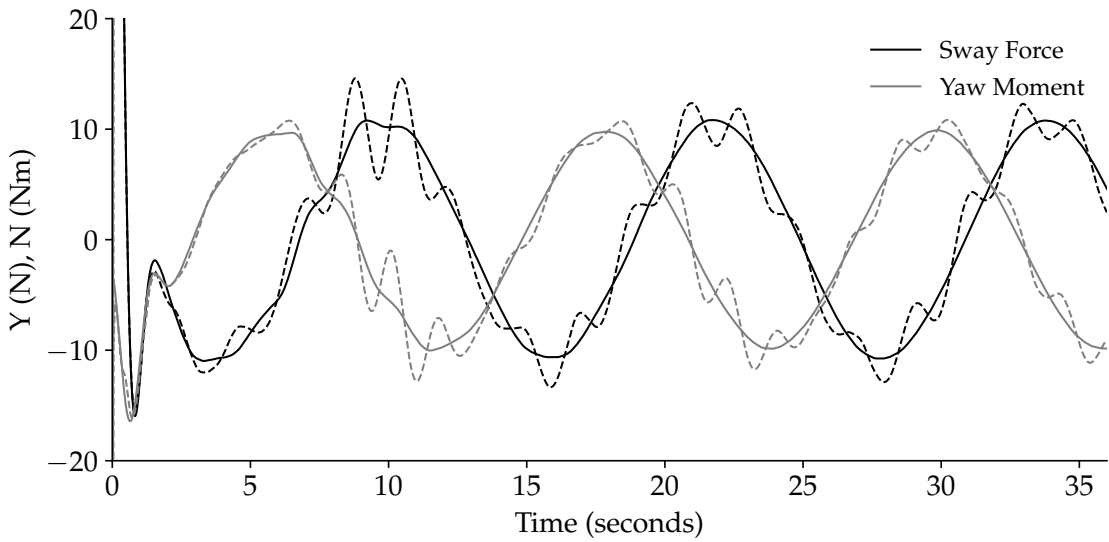


**Figure 4.6:** Sway force and yaw moment for the initialized solution (—) and the non-initialized solution (---) for the PMM in pure sway ( $T = 12s$ ,  $y_0 = 0.2026m$ ). Time  $t = 0$  corresponds to the start of the imposed motion.

In the active cells, the governing equations are solved, the inactive cells are the result of the hole cutting process and no equation is solved in them. The acceptor cells are used to couple the solution between the overset and the background mesh. Finally, donor cells are cells in the background in contact with the overset used for the interpolation, see Siemens (2017).

The overset mesh topology is similar to the mesh used for the static drift simulations, in addition, an overset part is created. This consists of a block containing the model and the desired refinements (the same prism layer was used to achieve the desired  $y^+$  value, as well as the same free surface refinements). This block is then placed in the background mesh. An overlap refinement has to be created where the overset is expected to move in the background mesh. Care has to be taken in ensuring that the cells of the overset and the overlap are of similar size.

#### 4.2.3 Numerical Solution

Planar motion mechanism simulations require an unsteady approach to solve them. As in the static drift simulation, an implicit unsteady approach is used with the segregated flow solver.

The number of time-steps per oscillatory period used in the literature varies drastically for PMM simulations, from 300 to 6000 for free surface simulations. Oldfield et al. (2015) estimated that 2800 time-steps per oscillation gave acceptable temporal discretization errors for the DTMB-5415. The chosen time-step is therefore 0.005 s, for a total of 2400 time-steps per period of oscillation. In addition, the overset mesh approach requires a

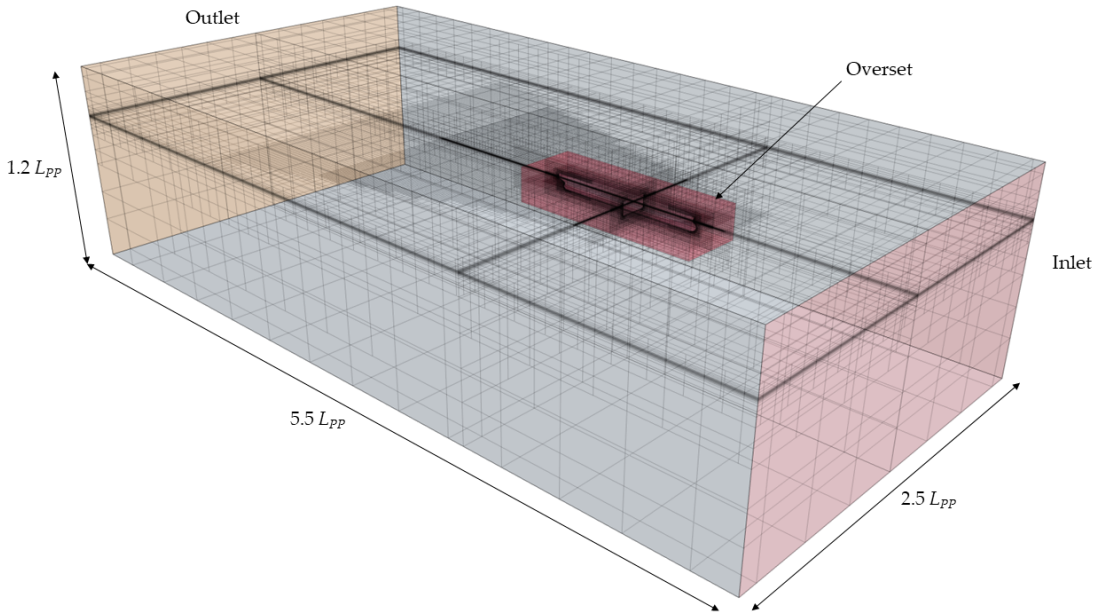


**Figure 4.7:** Overall view of the domain used for the PMM simulations.

maximum displacement of half a cell per time-step (using 2<sup>nd</sup> order temporal discretization). With an average cell size at the interface of 0.02 m, and a maximum velocity of 0.25 m/s this criterion is easily achieved. Table 4.3 summarises the solver parameters.

#### 4.2.4 Boundary Conditions

In addition to the boundary conditions on the domain itself, which are the same as the boundary conditions for the static drift simulations, see table 4.2, an interface between the overset and the background is created. This interface is used to provide the coupling between the two regions, 4-5 cells are required on each side with the linear interpolation used. With the use of linear interpolation, mass conservation is not strictly imposed at the interface. This has an effect when the discrete Poisson equation is used to obtain the divergence-free velocity field with the SIMPLE scheme. For external flow, this error is minimal (0.1%, see Star CCM<sup>+</sup> (2013)) and it is recommended not to correct it but can have significant effects for internal flows. Two methods are proposed within Star-CCM<sup>+</sup>, a source term and a flux correction term. Both have been used to try to improve the instabilities described earlier. Use of the source term created waves at the overset boundaries, generating unstable solutions and the flux correction term did not seem to improve the results. For simplicity, no correction was applied at the overset interface, additional information is required to make an informed decision concerning the adequacy of this choice, as of now the initialization described earlier seems to provide adequate results.

**Table 4.3:** Implicit unsteady and segregated solver parameters for the planar motion mechanism simulations.

Property	Value	Comment
Time-step	0.005s	2400 time-step/oscillations
Inner iteration	20	
6DOF solver	4	iterations
Temporal discretization	$2^{nd}$ order upwind	
Convective discretization	$2^{nd}$ order upwind	
$C_{u_l}$	5.0	
$C_{u_u}$	10.0	
URF <sub>velocity</sub>	0.8	default
URF <sub>pressure</sub>	0.2	default
URF <sub>SF</sub>	0.9	default
URF <sub>k-<math>\omega</math></sub>	0.8	default
URF <sub><math>\mu_t</math></sub>	1.0	default

#### 4.2.5 Motion

The motion for the PMM simulations can be obtained in two different ways in Star-CCM<sup>+</sup>, the built-in PMM model can be used, or the motion can be imposed manually. The first approach was initially used, but because the resulting motion did not correspond to the specified motion period, the second approach was adopted.

In the same way as model tests, the motion and force computation was done at midship, and not at the centre of gravity. Star-CCM<sup>+</sup> allows the force and moment to be calculated about any point, provided the mass of the model ( $m$ ), the distance to the centre of gravity to the origin of the motion ( $x_G$ ) and the inertia in yaw ( $I_{zz}$ ) are known. For the KVLCC2 this is readily available from experimental data, see table 1.2. As in the static drift simulations, only 3 DOF were considered, roll, pitch and heave were ignored.

The motion is applied following the equations described in section 3.2.2 and 3.2.3. In pure sway this does not pose any particular problem.

The pure yaw case is more complex. Starting from the straight-ahead position, the yaw motion is first imposed, once the model has reached the correct drift angle the transverse motion starts, see figure 4.8. Care has to be taken that an appropriate delay is introduced between the start of the yaw and the transverse motion. The user-defined functions used to impose the motions are presented in appendix C.3.

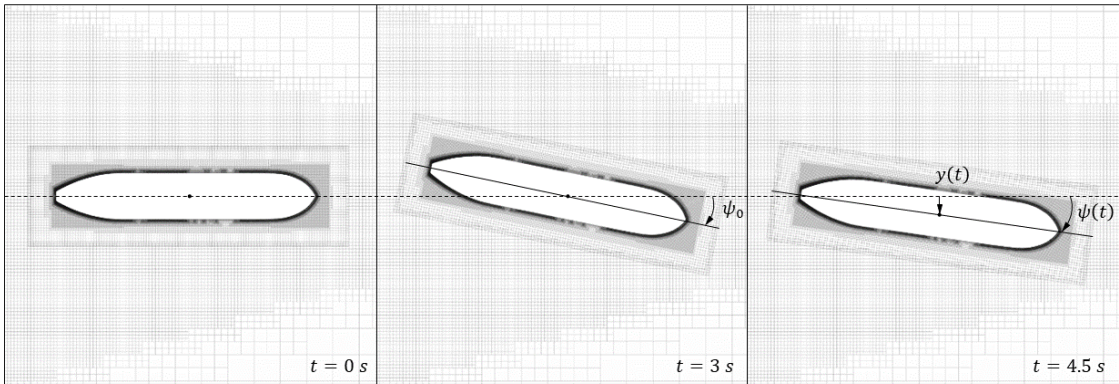


**Figure 4.8:** Illustration of the imposed motion for the PMM in pure yaw ( $T = 12\text{s}$ ,  $Fr = 0.142$ ) at three different times. At  $t = 0\text{ s}$  the yaw motion is imposed, at  $t = 3\text{ s}$  the yaw angle is maximum and the sway motion is imposed,  $t = 4.5\text{ s}$  depicts the position of the model, following the harmonic path. Viewed from above.

#### 4.2.6 Additional Investigations

In addition, the sensitivity of the results to the turbulence model was investigated. The Realizable  $k-\epsilon$  model was compared to the standard model used, the  $k-\omega$  SST for the PMM in pure sway with a motion period of  $T = 12\text{ s}$ . The standard mesh described earlier for the PMM simulation was adopted. All other solver parameters were not altered. The motion was also initialized when the  $L_2$  Norm of the changes in pressure on the hull surface dropped below  $10^{-5}$ .

Finally, the influence of the addition of an undeflected rudder was undertaken. The same approach as in the static drift simulation was used to add the rudder to the PMM simulations. All simulations were performed with the standard mesh (with the addition of the rudder) and the  $k-\omega$  SST turbulence model. The solver properties, motion initialization, etc., followed the approach described previously.

### 4.3 Verification and Validation

The procedure proposed by Stern et al. (2001), which is also the ITTC preferred method (ITTC, 2008), will be used throughout this thesis. The procedure aims at estimating the numerical uncertainties, and once those uncertainties have been determined, benchmark data is used to validate the results.

The numerical error can be defined as consisting of round-off, iterative and discretization errors. The use of a double precision<sup>1</sup> flow solver ensures that the round-off errors are

---

<sup>1</sup>numbers are stored with 16 decimals

negligible compared to the other sources of errors. Therefore, the numerical uncertainty of the solution are

$$U_{SN}^2 = U_I^2 + U_G^2. \quad (4.2)$$

The iterative uncertainty  $U_I$  arises from the imbalance in the numerical solution to the governing equations, often referred to as residuals. The grid uncertainty  $U_G$  is due to the discretization of the governing equations.

To assess the iterative convergence of a solution, the residuals of the momentum, continuity and turbulence closure equations are monitored. For unsteady simulations, they should converge to a reasonable value at each time-step. In addition to monitoring residuals, iterative convergence can be assessed by monitoring global quantities, such as the pressure and shear stress on the hull. The convergence of such quantities is of much more interest than the actual value of the residuals when trying to assess the iterative convergence of a numerical simulation. The  $L_2$  norm of change in pressure and shear stress on the hull is used to assess the iterative convergence of the simulations, as described in Eça and Hoekstra (2006)

$$U_I \equiv L_2(\Delta\phi) = \sqrt{\frac{\sum_{i=1}^{N_P} (|\Delta\phi_i|)^2}{N_P}}. \quad (4.3)$$

Where the variable change between consecutive iterations is used

$$\Delta\phi_i = \phi^n - \phi^{n-1}. \quad (4.4)$$

A typical plot of convergence of the  $L_2$  norm of the pressure and shear stress on the hull is shown on figure 4.9. Shear stress typically converges much faster than pressure, this is the main reason for using the pressure as a way of estimating convergence.

In estimating the grid uncertainty of a simulation, the solution on multiple meshes is required. For unsteady simulations the iterative convergence cannot be guaranteed to be the same for the different meshes. The numerical error therefore needs to be corrected,

$$\hat{S}_{km} = S_{km} - \delta_{I_{km}}^*, \quad (4.5)$$

where  $\delta_{I_{km}}^*$  is the iterative error and must be accurately estimated or negligible. Having corrected the iterative error, the solution changes between the different meshes are

$$\epsilon_{21} = \hat{S}_{k2} - \hat{S}_{k1} \quad \epsilon_{32} = \hat{S}_{k3} - \hat{S}_{k2}, \quad (4.6)$$

where  $\hat{S}_{k1}$ ,  $\hat{S}_{k2}$  and  $\hat{S}_{k3}$  are the corrected results for the fine, standard and coarse mesh,

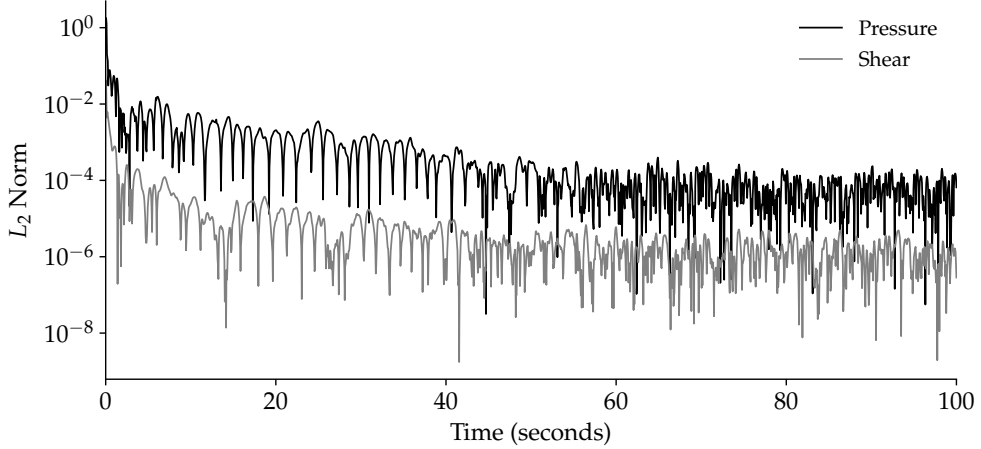


**Figure 4.9:** Convergence of the  $L_2$  norm of the pressure and shear stress on the hull for the static drift simulation for the standard mesh ( $\beta = 8^\circ$ ,  $Fr = 0.142$ ). The shear stress converges to  $1.42 \times 10^{-6}$  whereas the pressure converges to  $7.11 \times 10^{-5}$ .

respectively. The convergence of the solution is estimated as

$$R_G = \frac{\epsilon_{21}}{\epsilon_{32}}. \quad (4.7)$$

The solution is said to monotonically converge if  $0 < R_G < 1$ , oscillatory converge if  $R_G < 0$  and diverge if  $R_G > 1$ . For monotonic convergence, generalized Richardson Extrapolation (RE) can be used to determine the apparent order of convergence,  $p$  and the grid convergence index (GCI), as proposed in Celik et al. (2008),

$$\begin{aligned} p &= \frac{|\ln \frac{\epsilon_{32}}{\epsilon_{21}}|}{\ln(r_{21})} + q(p) \\ q(p) &= \ln \left( \frac{r_{21}^p - s}{r_{32}^p - s} \right) \\ s &= 1 \cdot \text{sgn}(\epsilon_{32}/\epsilon_{21}). \end{aligned} \quad (4.8)$$

Note that for  $r_{21} = r_{32}$ , we have  $q = 0$  and the procedure becomes the exact same as the one described in Stern et al. (2001). The advantage of the method described herein is that it can be applied to meshes with non-uniform refinement ratios  $r_{21} \neq r_{32}$ . Finally, the grid convergence index of the fine mesh is estimated

$$U_G \equiv \text{GCI}_{\text{fine}}^{21} = \frac{1.25 \cdot e_a^{21}}{r_{21}^p - 1}, \quad (4.9)$$

where  $e_a^{21}$  is the approximate relative error and the factor of 1.25 accounts for the confidence in this prediction. See Celik et al. (2008) for the full description of the procedure. Similar

expressions can be derived to obtain GCI<sup>21</sup><sub>standard</sub>, to express the grid convergence index for the standard mesh. This is also equal to the grid uncertainty ( $U_G$ ) defined earlier. Thus, the numerical uncertainty can be estimated using equation 4.2. Validation is then performed by comparing the validation uncertainty

$$U_V = \sqrt{U_D^2 + U_{SN}^2}, \quad (4.10)$$

to the magnitude of the comparison error,  $|E|$ ,

$$E = D - S, \quad (4.11)$$

where  $D$  is the experimental result and  $S$  is the simulation result. The simulations are validated if  $|E| < U_V$ . The uncertainty of the experimental data,  $U_D$ , can be estimated following ITTC (2014).

For oscillatory convergence Richardson extrapolation cannot be used, the results for more than three meshes are required to determine the upper ( $S_U$ ) and lower ( $S_L$ ) bound of the oscillation of the solution and thus the grid uncertainty

$$U_G = \frac{1}{2}(S_U - S_L). \quad (4.12)$$

For divergence, improvements to the solution have to be made, i.e. iterative convergence, grid quality, modelling strategies, etc.

# Chapter 5

## Static Drift Simulations

This chapter exposes the results obtained for the static drift simulations. The results of the verification and validation process are presented. The sensitivity of the solution to the time-step and turbulence model is detailed. Finally, the slow motion derivatives are presented and discussed.

### 5.1 Verification and Validation

To ensure that the complexity of the flow is fully accounted for, the procedure was undertaken for a drift angle  $\beta = 8^\circ$  and  $Fr = 0.142$ . Three meshes were produced to determine the iterative and discretization errors. A systematic refinement and coarsening were applied to the standard mesh described in section 4.1.2. To respect the requirements of the wall function approach, the prism layer on the surface of the hull was not altered. The global refinement in way of the hull and in the viscous wake, as well as the Kelvin wake were adjusted to achieve a mesh refinement ratio of 1.75.

#### 5.1.1 Global Quantities

Results are presented for three meshes with cells count of 1.99, 3.4 and 6.3 millions for the coarse mesh ( $N_3$ ), standard mesh ( $N_2$ ) and the fine mesh ( $N_1$ ), respectively. This corresponds to refinement ratios of  $r_{21} = 1.85$  and  $r_{32} = 1.7$ . The time-step and inner iteration used for the standard mesh were not altered (see table 4.1).

Convergence of the  $L_2$  Norm of pressure change on the model for the three meshes is exposed in table 5.1. Good agreement is obtained for all the meshes considered, the largest difference is obtained for the fine mesh. For all three meshes, the values of iterative uncertainty are well below expected grid uncertainty and can therefore be safely neglected when calculating the corrected numerical solution (equation 4.5). This greatly simplifies the calculation of the grid uncertainty without losses of accuracy. Iterative uncertainty

is expressed as a percentage of the total pressure force ( $\%S$ ) on that particular mesh. It should be noted that values of convergence of the shear stress on the hull are at least an order of magnitude below the pressure for all the meshes considered.

**Table 5.1:**  $L_2$  norm of the change between iterations for the different meshes ( $\beta = 8^\circ$ ,  $Fr = 0.142$ ).

Mesh	Cells ( $\times 10^6$ )	$L_2$ norm Pressure	$U_I \%$ S
Fine ( $N_1$ )	6.3	$6.73 \times 10^{-5}$	0.006
Standard ( $N_2$ )	3.4	$7.10 \times 10^{-5}$	0.007
Coarse ( $N_3$ )	1.99	$7.24 \times 10^{-5}$	0.007

Surge force ( $X$ ), sway force ( $Y$ ) and yaw moment ( $N$ ) used for the grid convergence study were obtained by time-averaging the last 10 s of the time record of the forces and moment obtained from the CFD simulations. The results are presented in table 5.2. Monotonic convergence is achieved for all the global variables considered, implying that all meshes are in the asymptotic range. This is better observed on figure 5.1. Richardson extrapolation can therefore be used to determine the extrapolated value ( $\hat{S}_{\text{ext}}^{21}$ ), the order of convergence and the grid convergence index (GCI).

Extrapolated values, representing the solution on an infinitely refined mesh, is in good agreement with the values of the variable obtained on the different meshes, with the largest variation being 2.04%.

The theoretical order of converge of the numerical scheme used is second-order accurate. This means that the solution should converge at this rate with increased mesh density, however, when a mesh is refined, the physics captured change to a certain extent, increasing the convergence rate of the solution. Large variations of the apparent order of convergence are obtained for the different variables. The surge force shows the best agreement with the theoretical value of 2, while the yaw moment shows an apparent order 6 times greater.

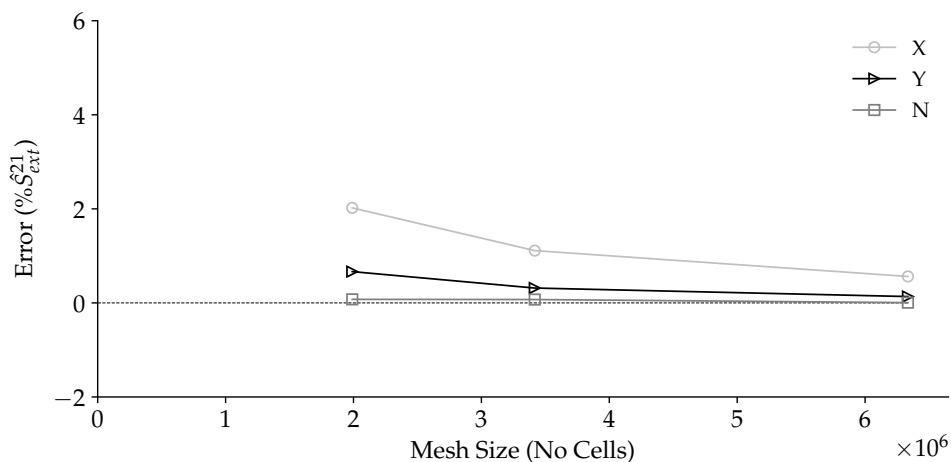
The grid convergence index (GCI) is used as an estimate of the gird uncertainties ( $U_G$ ). Very small values are achieved for all variables considered, with an extremely small value for the yaw moment.

The results from the grid convergence study can be used to determine the numerical uncertainties and therefore validate the simulation using the benchmark data. There is no experimental data for uncertainty analysis for the bare hull in static drift, only for the hull fitted with a propeller and rudder and at a drift angle of  $\beta = 12^\circ$ . It is however believed that the uncertainty obtained during this test should be similar to that of a bare hull static drift tests. The procedure described in ITTC (2014) was used to determine the experimental uncertainties. No additional considerations for measurement devices uncertainties have been made.

**Table 5.2:** Grid convergence study for the static drift simulations ( $\beta = 8^\circ$ ,  $Fr = 0.142$ ).

	$X$ (N)	$Y$ (N)	$N$ (Nm)
$\hat{S}_{k1}$ (Fine)	-3.111	5.512	8.860
$\hat{S}_{k2}$ (Standard)	-3.094	5.502	8.8544
$\hat{S}_{k3}$ (Coarse)	-3.065	5.483	8.8540
Convergence <sup>1</sup>	M	M	M
$p$ (apparent order)	<b>3.31</b>	<b>4.13</b>	<b>12.13</b>
$\hat{S}_{\text{ext}}^{21}$	-3.129	5.519	8.861
$e_a^{21}$	0.55	0.18	0.07
$e_{\text{ext}}^{21}$	0.56	0.14	0.01
<b>GCI<sub>standard</sub><sup>21</sup></b>	<b>1.41</b>	<b>0.4</b>	<b>0.0074</b>

<sup>1</sup> M: monotonic convergence, O: oscillatory convergence, D: divergence

**Figure 5.1:** Relative error in the force and moment prediction for the different meshes with respect to the extrapolated value  $\hat{S}_{\text{ext}}^{21}$ .

The validation uncertainty of the sway force, determined using equation 4.2 is

$$U_V = \sqrt{U_{SN}^2 + U_D^2} = 0.1918 = 2.75\%D, \quad (5.1)$$

with  $U_D$  presented in appendix C.4. The comparison error  $E$  for the sway force at  $\beta = 8^\circ$  is

$$E = D - S = 6.4129 - 5.5024 = 0.9105 = 14.19\%D, \quad (5.2)$$

such that the sway force is not validated, as  $|E| > U_V$ . Similarly, the yaw moment is not validated, with a validation uncertainty  $U_V = 0.56\%D$  and a comparison error of  $E = 7.25\%D$ . Both sway force and yaw moment show very good validation uncertainty, this is because of the very low grid convergence index and thus  $U_G$  obtained, as well as the good repeatability of the experiments. The comparison error being positive means that the CFD results under-predict the experimental data. Validation is also not performed at drift angles of  $\beta = 4^\circ$ , assuming a validation uncertainty of similar order.

On a side note, comparison of the total drag coefficient,  $C_T = X/\frac{1}{2}\rho U^2 A$  (surge force for  $\beta = 0$ ) can be made with numerical results obtained during the Gothenburg 2000 workshop (Larsson et al., 2003). The value obtained from the CFD of the present study overestimates  $C_T$  by 9.2% compared to the mean of the CFD results presented therein. The standard variation found during this workshop was 5.2%. The total drag coefficient found is still within the maximum and minimum range of values obtained from the different investigators, despite being larger than the standard variation. This value, however, corresponds to an average of simulations mostly not accounting for the free surface. Despite the simulations not aimed at resistance prediction, it is able to yield acceptable results of drag coefficients compared to other numerical predictions.

### Temporal Sensitivity

The temporal sensitivity study was performed on the standard mesh by doubling and halving the time-step and the number of inner iterations. This was done to keep the total number of iterations, and thus the simulation time the same. It should be noted that for the time-step of 0.025s the number of inner iterations was not halved, as this would have resulted in very few iterations at each time-step, it was reduced to 7 inner iterations. The  $L_2$  norm of the change in pressure on the hull between two iterations is used as verification for the temporal sensitivity study in addition to the a comparison of the forces obtained. The sway force and yaw moment obtained by varying the time-step can be seen on figure 5.9 and 5.10, respectively.

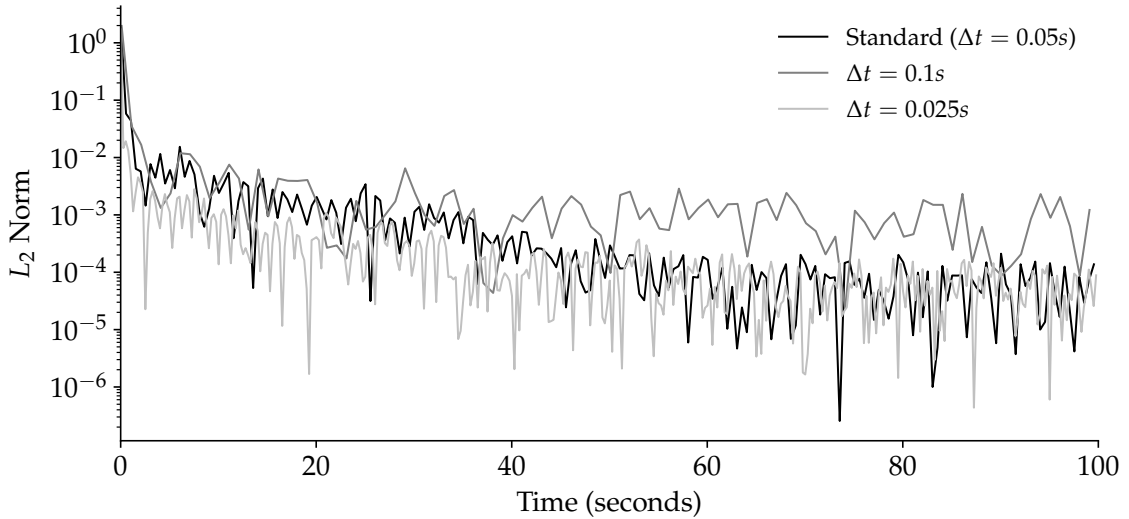


**Figure 5.2:**  $L_2$  norm of the pressure changes between consecutive iterations on the hull for different time-step/inner iteration combinations. Results plotted every 10 points for clarity.

**Table 5.3:** Temporal sensitivity study for the static drift simulations ( $\beta = 8^\circ$ ,  $Fr = 0.142$ ).

Time-step (s)	$Y$ (N)	$N$ (Nm)	$L_2$ Norm Pressure
0.1	5.5068	8.8710	$1.009 \times 10^{-3}$
0.05	5.5024	8.8544	$7.1016 \times 10^{-5}$
0.0025	5.4971	8.8490	$5.1240 \times 10^{-5}$

The difference in iterative convergence with changes in time-steps can be seen on figure 5.2. The two smallest time-steps resulted in values  $L_2$  Norm of pressure changes in the order of  $10^{-5}$ , while the largest time-step resulted in values in the order of  $10^{-3}$ . It also resulted in higher residuals as well as the free surface being not well captured (not presented). Reducing further the time steps compared to the value used for the standard simulations does not show large improvement, neither in the level of iterative convergence achieved, nor in the magnitude of the force predicted. Despite the larger time-step showing some discrepancies, the forces obtained are very similar, with the largest deviation being 0.18%, see table 5.3. The only influence that the time-step has is on the representation of the free surface. The larger time-step results in the waves not being convected properly in the grid. This is due to the Courant number at the free surface being to large and the high dissipation of the scheme used in this case which will effectively dampen the waves. This could be addressed by adjusting the CFL threshold to force the solver to use the HRIC scheme, but this can lead to instabilities if the time-step is too large.

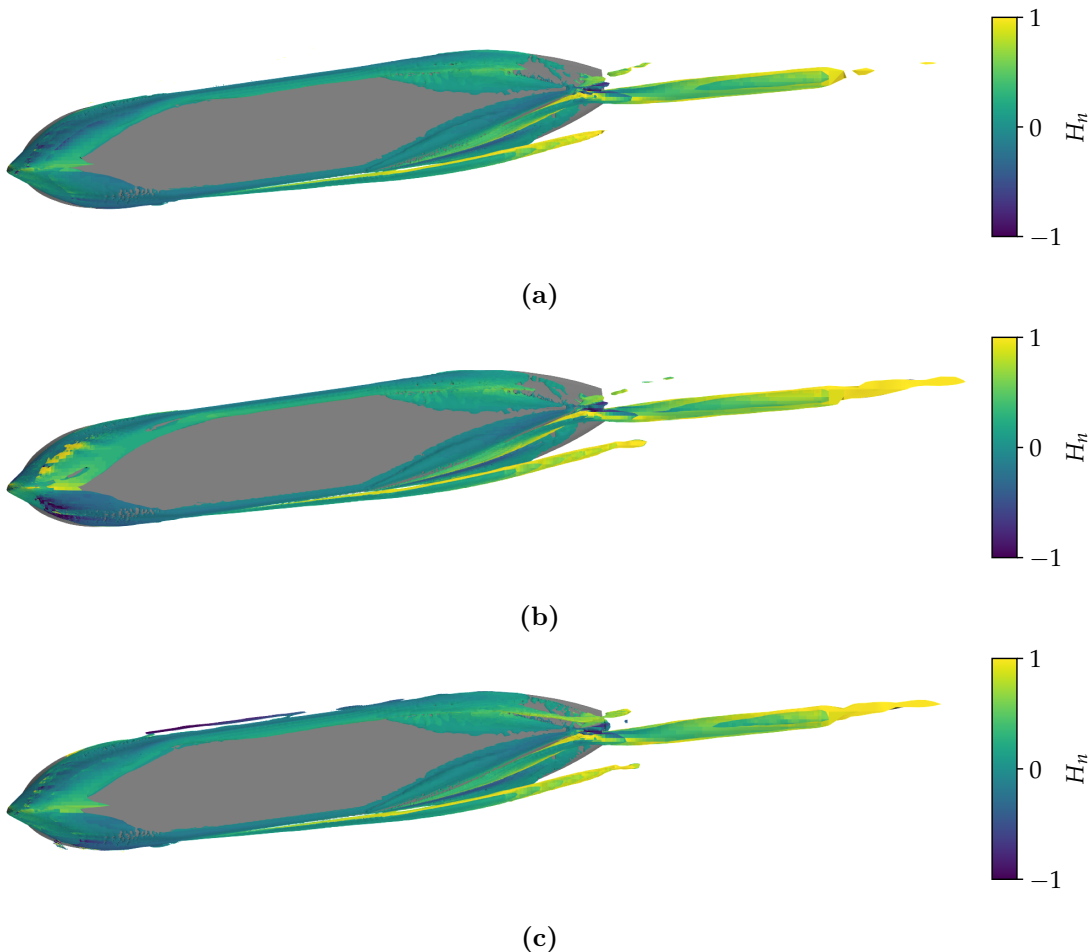


**Figure 5.3:** Isocontours of the Q-criterion (value of  $1.5 \text{ s}^{-2}$ ) coloured with the normalized helicity ( $H_n$ ). (a)  $k-\omega$  SST (b) Spalart-Allmaras (c) Realizable  $k-\epsilon$  turbulence model ( $\beta = 8^\circ$ ,  $Fr = 0.142$ ). Viewed from below.

### Turbulence Closure Sensitivity

In addition to spatial and temporal sensitivity study, a turbulence closure sensitivity study was undertaken. The results from the standard model used, the  $k-\omega$  SST were compared to another two-equation model, the Realizable  $k-\epsilon$  and a one equation model, the Spalart-Allmaras for the test case ( $\beta = 8^\circ$ ,  $Fr = 0.142$ ) the standard mesh was used, as well as the standard time-step/inner iteration.

To visualize the vortical structure forming around the model, the Q-Criterion proposed by Hunt et al. (1988) is used

$$Q = \frac{1}{2} (||\bar{\Omega}||^2 - ||\bar{S}||^2) > 0, \quad (5.3)$$

where  $\Omega$  is the rotation tensor and  $S$  is the strain-rate tensor. This criterion can be colourized using the normalized helicity  $H_n$  (Degani et al., 1990)

$$H_n = \frac{\mathbf{v} \cdot \boldsymbol{\omega}}{|\mathbf{v}| |\boldsymbol{\omega}|}, \quad (5.4)$$

where  $\boldsymbol{\omega}$  is the vorticity and  $\mathbf{v}$  the velocity vector. A positive unity value of the normalized helicity therefore corresponds to an anticlockwise rotation of the flow.

Results for the forces are very similar for the two-equation models; however, differences are present for the Spalart-Allamars, see figure 5.9 and 5.10. It is interesting to note that the vortical structure of the model (as in ship model) is well captured by the three models, see figure 5.3. The two two-equation models show very similar vortical structures, the  $k-\epsilon$  shows a larger fore-body bilge vortex compared to the  $k-\omega$  SST, this vortex is also not visible in the Spalart-Allmaras predictions (5.3b). The Spalart-Allmaras predictions also show differences in the bow region of the model, where the vortical structures are less defined. The discrepancies observed from the Spalart-Allamaras model could arise from the two-layer wall treatment used, combined with a mesh with a  $y^+$  not completely adequate for this model (this model can be applied with wall functions).

The inability of the Spalart-Allmaras model to correctly predict the surge force arise from its computation of the shear stress on the hull, which is greatly underpredicted compared to the two-equations models, especially in the bow region, see figure 5.4. Because the shear stress is the major contributor to the surge force, correctly predicting it is critical; however, this is not as important for the sway force and yaw moment which are mostly driven by pressure forces. The  $L_2$  norm of pressure and shear is of the same order of magnitude for the three models, this would indicate that iterative convergence is not dependent on the choice of the turbulence model.

### 5.1.2 Local Flow Quantities

In addition to the global quantities treated in the previous section, local quantities such as the wave pattern or the nominal wake can be validated with experimental or numerical data available for the KVLCC2 (Kim et al., 2001; Kume et al., 2006).

To validate the free surface capturing method, as well as the grid topology used for this purpose, the wave pattern obtained from the CFD can be compared to wave pattern measurements, see figure 5.5. The KVLCC2 features a particular type of wave pattern, most of it is formed by the bow wave and very few waves are generated at the transom. This is very well captured by the CFD, with the bow wave being very similar to experimental measurements. The elevation generated at the bow by the bulb is also well captured. Differences are present for the stern wave system, mostly due to the experimental data lacking measurements in this area. The grid coarsening approach used to dampen the

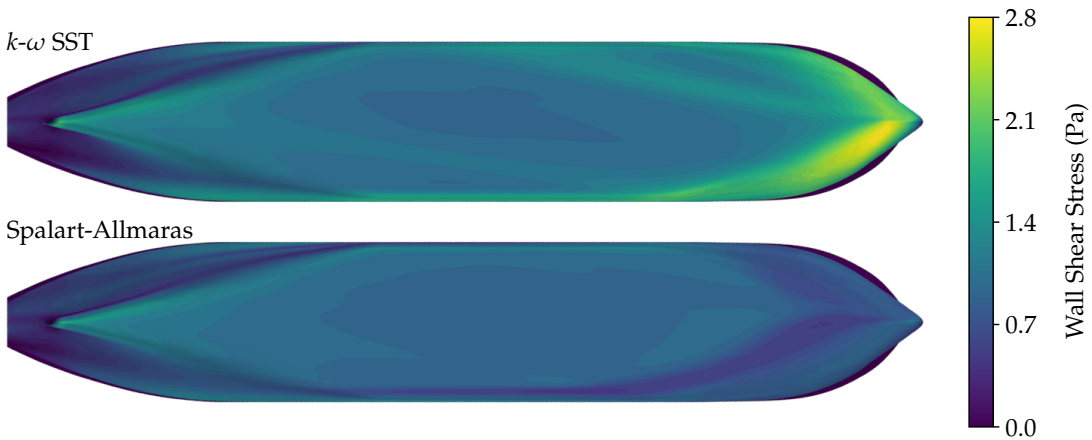


**Figure 5.4:** Bottom view of the wall shear stress on the KVLCC2 for the  $k-\omega$  SST (top, standard simulation) and the Spalart-Allmaras (bottom) turbulence model for the static drift case ( $\beta = 8^\circ$ ,  $Fr = 0.142$ ). Note the large difference in the predicted wall shear stress at the bow for the Spalart-Allmaras model. Model rotated for clarity, the flow is therefore coming from the bottom right.

wave pattern also proved to be working efficiently, with no trace of wave reflection on the boundaries of the domain. The typical Kelvin wave pattern angle is seen to be properly reproduced, implying that the position of the wave is not influenced by the mesh density (except where the coarsening has been applied).

In addition, the wave elevation along the hull can also be compared to experimental data, see figure 5.6. Likewise, the results show good agreement with the experimental data. The smearing of the free surface due to the high local CFD number close to the ship renders the wave elevation uneven. The start of the bow wave pattern on the side of the ship is clearly seen at a  $x/L_{PP}$  of -0.4.

The nominal wake of the KVLCC2 has been the focus in much of the numerical predictions (Kim et al., 2001; Larsson et al., 2003). It features a very distinctive hook shaped structure due to the propeller hub. The study of the wake indicates if the viscous wake is properly captured, for manoeuvring this is relatively important as a majority of the forces are from viscous contributions. The nominal wake of the KVLCC2 is depicted in figure 5.7. The CFL is able to accurately model the viscous wake, the hook shaped structure is captured and shows good agreement with the experimental data. An accurate modelling of the wake is also required to properly measure the influence of adding a rudder, or a propeller.

The vortical structure of the KVLCC2 has been studied both experimentally and numerically (Abdel-Maksoud et al., 2015; Xing et al., 2012). Due to the relatively sharp turn of bilge, three main vortices are formed, see figure 5.8., which are accurately captured,

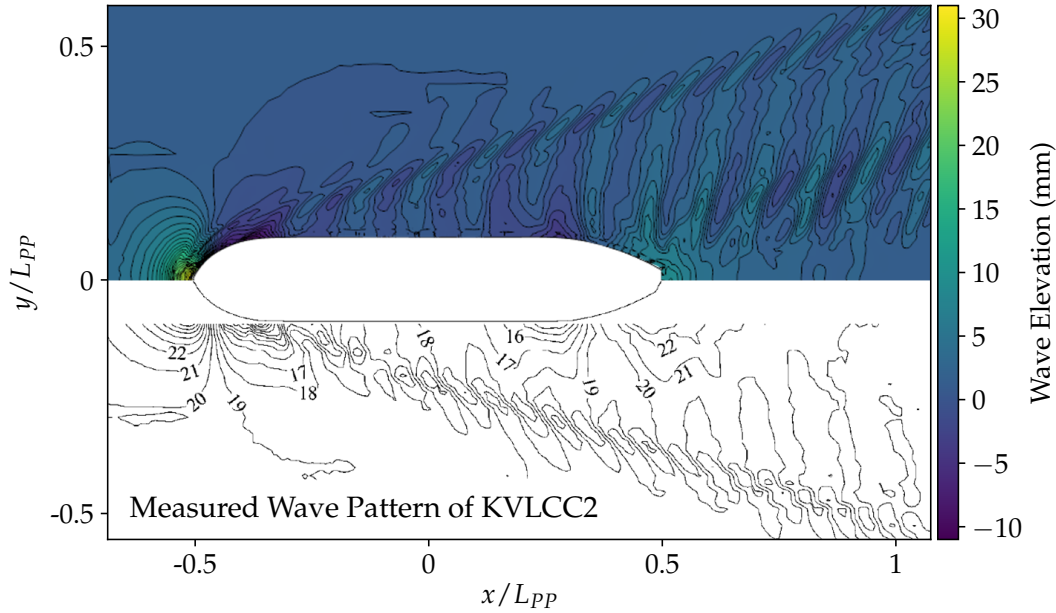


**Figure 5.5:** Wave elevation around the KVLCC2, from CFD of present study (top) and experimental data (Kim et al., 2001)(bottom) for  $Fr = 0.142$ ,  $\beta = 0^\circ$ . For the measured wave elevation, level 21 corresponds to the undisturbed free surface and a unit level change corresponds to a change in elevation of 0.5 mm.

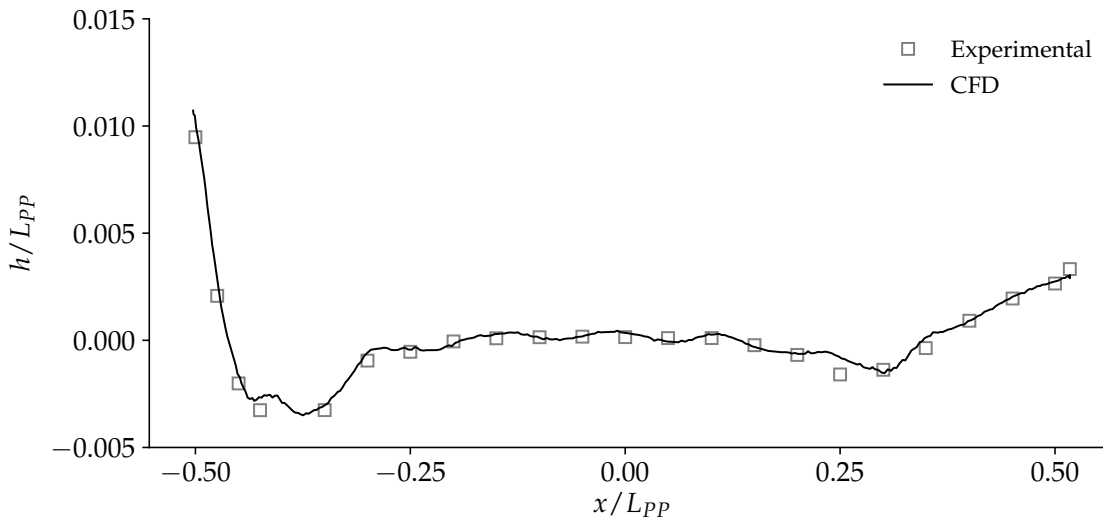


**Figure 5.6:** Comparison of normalized wave profile along the hull of the model ( $Fr = 0.142$ ,  $\beta = 0^\circ$ ). Experimental data from Kim et al. (2001). It should be noted that the interface is not smooth on the surface of the ship due to the CFL being very high and thus the UD scheme is used, introducing numerical dissipation.

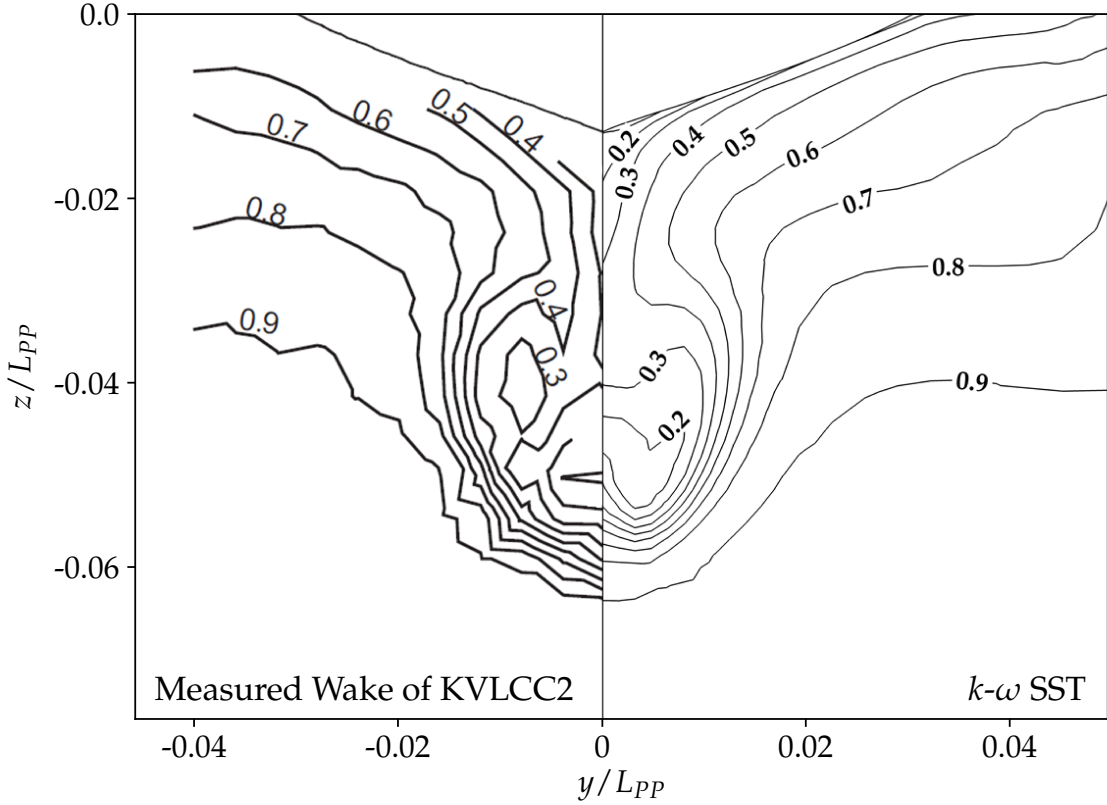


**Figure 5.7:** Normalized velocity in the nominal wake of the KVLCC2, from CFD of present study (right) and experimental data (Kume et al., 2006)(left) for  $Fr = 0.142$ ,  $\beta = 0^\circ$ . The plane is located at  $x/L_{PP} = 0.48$ . Note the typical hook shape present in the wake, which is captured by the CFD.

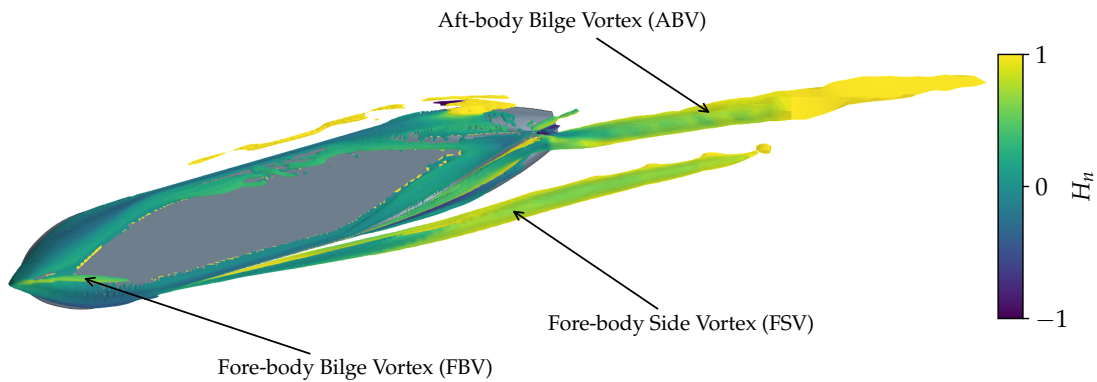


**Figure 5.8:** Isocontours of Q-criterion (value of  $1.5 \text{ s}^{-2}$ ) coloured with normalized helicity ( $H_n$ ) showing the vortical structures forming on the KVLCC2 ( $\beta = 16^\circ$ ,  $Fr = 0.142$ ) using the  $k-\omega$  SST turbulence model.

even the weaker fore bilge vortex. The representation of the vortex is influenced by the mesh density, for the standard mesh, they do not extend past the viscous wake refinement, the fine mesh features a longer viscous wake refinement and the vortices are allowed to extend further downstream. However, this does not seem to have a measurable influence on the forces predicted, as all three meshes show similar results, see figure 5.9 and 5.9.

## 5.2 Slow Motion Derivatives

From the plots of the sway force/yaw moment for different sway velocities (figure 5.9, 5.10), the gradient at the origin can be used to determine the slow motion derivatives. A first-order polynomial is fitted to the points and the gradient recorded. In order to compare results at different scales the slow motion derivatives are made non-dimensional as follows:

$$Y'_v = \frac{Y_v}{\frac{1}{2}\rho UL_{PP}^2} \quad N'_v = \frac{N_v}{\frac{1}{2}\rho UL_{PP}^3}, \quad (5.5)$$

all other non-dimensional coefficients are shown in the *Dimensionless Quantities*.

The results presented in table 5.4 are computed using results up to  $\pm 4^\circ$  of drift, including the points at larger drift angles, where the agreement between the CFD predictions and the experiments starts to deteriorate was not made. Sway force and yaw moment derivatives show acceptable agreement with the experimental data. The observation made earlier that the CFD results underpredicted the forces and moment is reflected here, with the derivatives obtained from the CFD results being lower than the one obtained from the experimental data. The error obtained for the yaw moment  $N'_v$  is somewhat lower than for the sway force  $Y'_v$ . This can be caused by the uncertainties in the force and the point of application of this force used to calculate the moment to somewhat cancel each other out, and give rise to the observed behaviour. Similar behaviour was observed by He et al. (2016) and Kim et al. (2015).

The agreement with experimental data is satisfactory enough so that the slow motion derivative obtained can be used to simulate standard manoeuvres. There is quite a bit of scatter in the derivatives obtained from experimental results as well, this reflects the difficulty to very accurately predict them numerically as well as experimentally. Part of the differences between the experimental results is also due to the scale factor of the model not being the same, which has a measurable influence on the derivatives.

Inclusion of points with smaller drift angles, both for the numerical and experimental (NMRI) data could result in a better agreement, unfortunately, experimental results for such drift angles are not available. Inclusion of points at larger drift angles in the curve-fitting did not result in a better agreement between results.

**Table 5.4:** Comparison of slow motion derivatives against experimental values. Gradients calculated using values from  $\beta \pm 4^\circ$ . Error expressed as a % of experimental data ( $D$ ).

Derivative	Present (CFD)	Experimental			<b>Mean</b>
		NMRI	MOERI	Kume et al. (2006)	
$Y'_v$	-0.01362	-0.01535	-0.01619	-0.01838	-0.01664
$\epsilon$ (%D)	-	-11.26	-15.87	-25.89	<b>-18.14</b>
$N'_v$	-0.00954	-0.01027	-0.00875	-0.01064	-0.009886
$\epsilon$ (%D)	-	-7.13	9.03	-10.43	<b>-3.50</b>

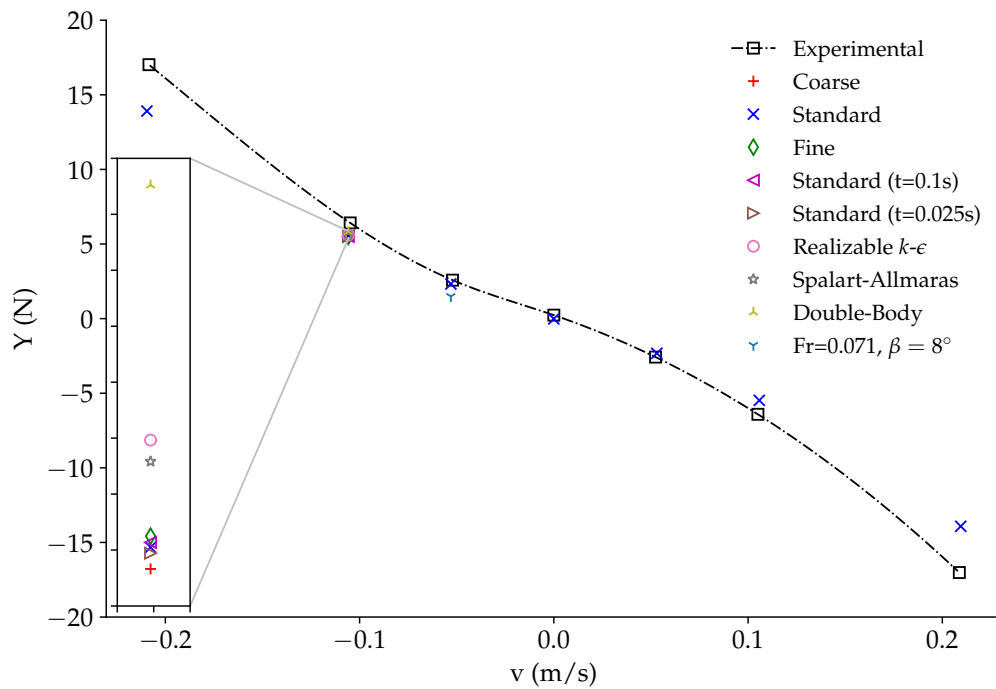


**Figure 5.9:** Sway force for different sway velocities, showing the mesh, time-step and turbulence sensitivity results. Detail magnification:  $\times 75$ .

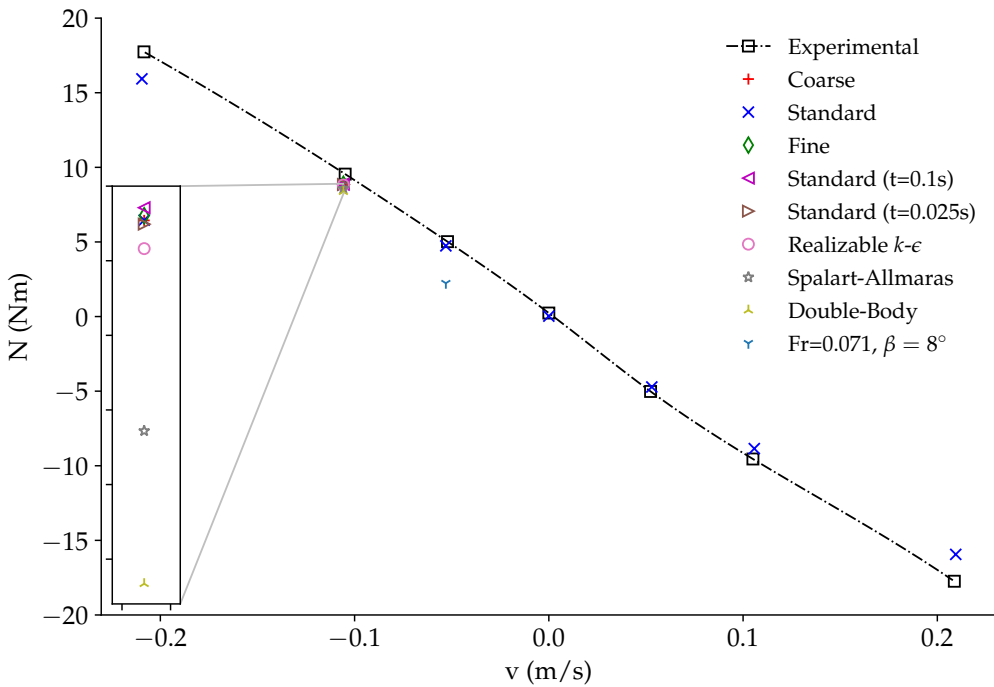


**Figure 5.10:** Yaw moment for different sway velocities, showing the mesh, time-step and turbulence sensitivity results. Detail magnification:  $\times 50$ .

### 5.3 Additional Investigations

To investigate the effects of modelling the free surface, the double-body approach was used. The results are presented in figure 5.9 and 5.10. Differences in the outcome obtained for the free surface capturing and the double-body simulations are small, within numerical errors. The computational time is however diminished with this approach, where only 1000 iterations are required for the  $L_2$  Norm of the pressure change on the hull to drop below  $10^{-5}$ . For low Froude number, such as the one considered here, the two approaches were not be expected to produce too dissimilar results.

The approach where the forward speed of the ship was altered to produce the desired sway velocity resulted in large discrepancies, both with standard numerical predictions and with experimental data. Meshes are Reynolds number dependent, and thus if the flow velocity is altered so should be the mesh to maintain the correct  $y^+$  and boundary layer resolution. By simply altering the inlet boundary condition, those are not respected anymore, and this leads to erroneous values of shear stress and pressure on the model. This approach will require the boundary layer mesh to be adjusted each time. Producing a mesh with the desired  $y^+$  is not a straightforward operation and can require a number of iterations to produce the desired value. Altering the drift angle is a much better approach, as the boundary layer mesh can be kept the same.

**Table 5.5:** Comparison of slow motion derivatives for bare hull and hull with rudder. The Difference ( $\epsilon$ ) is expressed relative to the rudder contribution to the slow motion derivative of the hull with rudder (S).

Derivative	Bare Hull	Hull with Rudder	Rudder Contribution
$Y'_v$	-0.013626	-0.014324	-0.000698
$\epsilon$ (%S)	-	-	4.87
$N'_v$	-0.0095431	-0.0090858	0.000457
$\epsilon$ (%S)	-	-	-5.03

Static drift simulations undertaken for the bare hull were reproduced with the addition of an undeflected rudder to research its influence on the slow motion derivatives. The results are presented in table 5.5.

With the addition of a rudder,  $Y'_v$  is increased, whereas  $N'_v$  is reduced. This results in a negative rudder contribution to the sway force and a positive contribution to the yaw moment. The addition of the rudder has the effect of shifting the centre of sway force aft, which reduces the yaw moment while increasing the sway force. This is often aimed for when the directional stability of the ship is an issue.

## 5.4 Discussion

This chapter presented the results obtained for the static drift simulations. Low levels of iterative convergence were found in all simulations undertaken. From a practical point of view, this simplifies the verification and validation process as well as giving more confidence in the results obtained. The method used for this effect is believed to be more representative than solely monitoring the residuals (Eça and Hoekstra, 2006). The verification process showed very good repeatability of the experimental data and a low level of numerical uncertainties. However, the sway force ( $Y$ ) and yaw moment ( $N$ ) are not properly validated, with a comparison error  $|E|$  larger than the validation uncertainty  $U_V$ . This would indicate that the simulations are subject to modelling errors. These errors could arise from mesh topology, turbulence closure, etc. The tendency observed is that numerical results underpredict experimental data.

The sensitivity of the solution to turbulence closure was also tested. The force and moment predicted by all three turbulence models are very similar. The Realizable  $k-\epsilon$ , predicts remarkably similar values compared to the  $k-\omega$  SST, despite having a relatively different formulation. Results for the Spalart-Allmaras model are also in good agreement with the  $k-\omega$  SST model, here again. Discrepancies were however observed for the shear stress prediction of this model. It is not clear to the author why the prediction is so different, as the Star-CCM<sup>+</sup> implementation of this model allows the use of a wall function

and the mesh used had an appropriate prism layer. Overall, the  $k-\omega$  SST model seemed to have given the best predictions. Very similar results were obtained with the Realizable  $k-\epsilon$  and this model could also be a valid choice for manoeuvring simulations.

Mesh topology was investigated with a comparison of free surface elevation and viscous wake. The results showed good agreement with the experimental data, which would indicate that the mesh topology used is of good quality. The use of wall function to model the boundary layer could contribute to a small part of the modelling errors observed, but they are not expected to be large enough to validate the results. The velocity field generated by the KVLCC2 features large unsteady flow structures such as the bilge and hub vortices. Those structures might benefit from a more advanced turbulent strategy (DDES, LES) to properly capture them, this could help reduce the comparison error and thus validate the findings, but referring to section 2.5, use of such methods do not necessarily result in more accurate force predictions.

Another aspect is the condition considered, at this drift angle  $\beta = 8^\circ$ , the flow might already be too detached and unsteady for the RANS approach used, validation could be performed on smaller drift angles (i.e.  $\beta = 2^\circ$ ), where the flow is not expected to be as unsteady.

Time-step sensitivity was also investigated for the simulation. It was found that while qualitative differences were present in the free surface representation produced by the different time-step chosen, quantitatively, the force and moment measured were within numerical uncertainties. The level of iterative convergence, however, showed to be lower for larger time-steps, even with an increased number of inner iterations. This is a typical behaviour, where the residuals follow an asymptotic decrease, and once a certain level is reached, large numbers of inner iterations are required to drop them further.

It was also found that with the inclusion of the free surface, care has to be taken that the wave field is allowed to travel downstream of the model before the results are extracted. The typical values given by ITTC (2017) were found to be too small. This is probably due to the low speed of the model ( $Fr = 0.142$ ) which requires a longer time for the wave pattern to build up.

The slow motion derivatives obtained show acceptable agreement with experimental data. The agreement for the yaw moment is somewhat better than the sway force. Here again, the predictions might be improved if smaller drift angles are considered. With the inclusion of more points (i.e. up to  $\beta \pm 8^\circ$ ) for the CFD results, the agreement can be improved, but this is not consistent with the approach used for the experimental data.

The double-body approach showed to produce very similar results compared to the VOF method. This is probably due to wave only having a small contribution in the force predictions. For investigations where computational power is limited this approach could be considered as valid, provided the Froude number of the model is small (below 0.15).

# Chapter 6

## Planar Motion Mechanism Simulations

This section presents the results obtained for the simulations of planar motion mechanism. First, the procedure used to post-process the experimental data is presented, then the method used to derive the oscillatory coefficients from the force and moment data is described. The verification and validation of the data is presented, and finally, the oscillatory coefficients are derived and discussed.

Two different motions were imposed on the model, one in pure sway and another in pure yaw. Each motion was imposed with two different oscillation periods, 12 and 6 s, respectively. This resulted in a total of 4 PMM simulations being undertaken to determine the oscillatory coefficients of the model. The motion imposed are presented in table 2.1.

### 6.1 Experimental Data Filtering

The raw experimental data provided by the National Maritime Research Institute (NMRI), via the SIMMAN (2014) workshop had to be post-processed. The forces and moment were expressed in the space-fixed coordinate system and not in the ship-fixed coordinate system. This is corrected by performing a coordinate system transformation.

To remove the noise in the raw data, a zero-lag low-pass Butterworth digital filter is applied (Robertson et al., 1993)

$$G(n)_{\text{filtfilt}} = \frac{1}{1 - \omega^{2n}}, \quad (6.1)$$

where  $n$  is the order and  $\omega$  is the cutoff frequency of the filter. The order and cutoff frequency were chosen by looking at the power spectral density (PSD) of the two signals, see figure 6.1.

The final filter is a 6<sup>th</sup> order Butterworth filter, with a cutoff frequency of 0.3 Hz (this

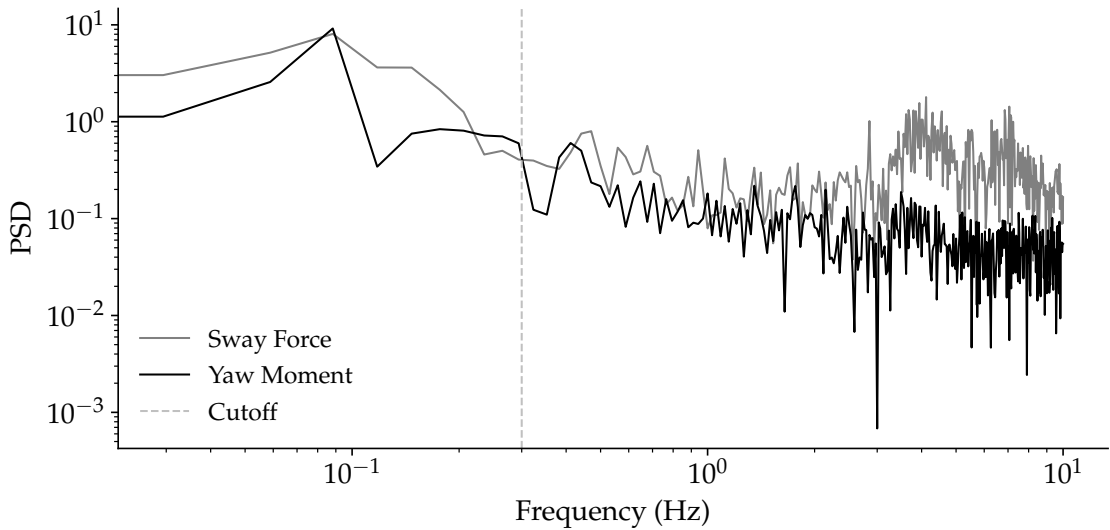


**Figure 6.1:** Power-spectral density of the sway force and yaw moment for the PMM in pure sway, data from experiment ( $T = 12$  s,  $y_0 = 0.2026m$ ). Note the peak at the frequency of oscillation of the PMM motion,  $f = 0.083$  Hz.

is for the PMM of pure sway with a period of  $T = 12$  s, other cutoff frequencies are used for the other experimental data filtering). The zero-lag is required for the post-processing of the experimental data, as the phasing between the velocity, acceleration and resulting force and moment is critical. This is readily implemented in Python, see appendix C.5.

In addition to filtering the data, the force and moment had to be corrected as they included inertial and centrifugal force effects of the model and the measuring system. Hydrodynamic sway force and yaw moment are obtained as follows

$$\begin{aligned} Y_{\text{hydro}} &= Y_{\text{filt}} + m(\dot{v} + ru + x_{\text{CG}}\dot{r}) \\ N_{\text{hydro}} &= N_{\text{filt}} + I_{zz}\dot{r} + mx_{\text{CG}}(\dot{v} + ru), \end{aligned} \quad (6.2)$$

where the letters have their original meaning, and  $u \sim \sqrt{U^2 - v^2}$ . The mass of the measuring equipment is 0.434 kg in the surge direction and 0.764 kg in the sway direction. The moment of inertia in yaw ( $I_{zz}$ ) is 89.67 Nms<sup>2</sup>. The distance between the centre of gravity and the origin of the coordinate system ( $x_{\text{CG}}$ ) is 0.1009 m.

## 6.2 Oscillatory Coefficients

Following Oldfield et al. (2015), a regression method was used to determine the oscillatory coefficients from the experimental and numerical results. This involved minimising the weighted sum of the square of the errors between the results and the corresponding Taylor

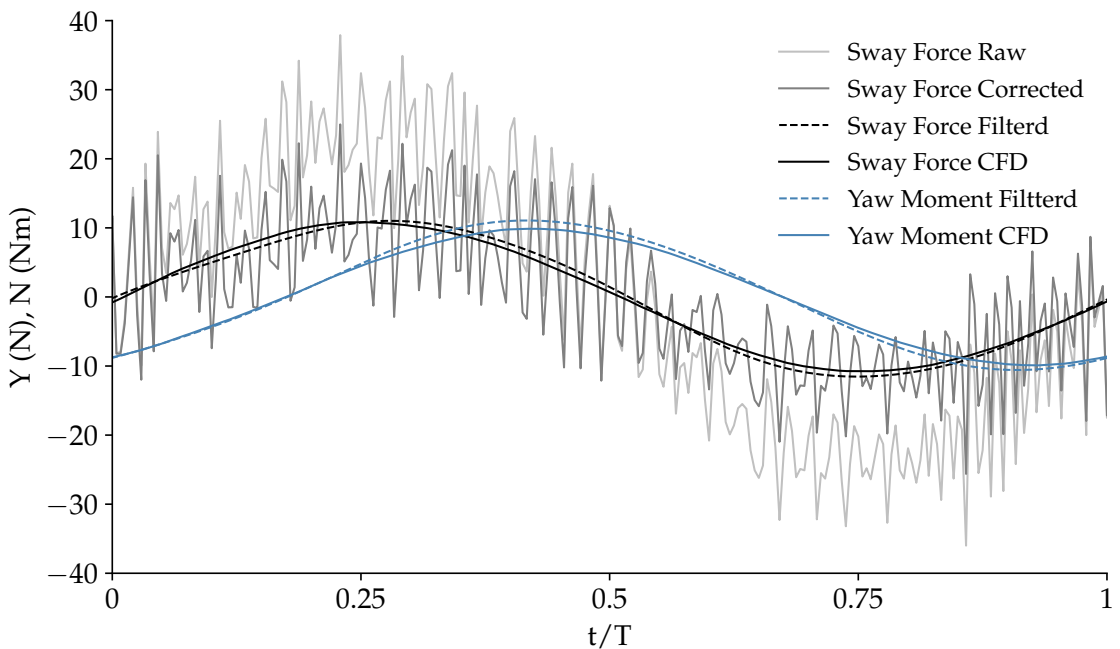


**Figure 6.2:** Sway force and yaw moment for a single period of oscillation for the PMM in pure sway ( $T = 12\text{s}$ ,  $y_0 = 0.2026\text{m}$ ). Raw and corrected yaw moment data have been omitted for clarity.

series approximations given in section 3.2. As an example, for the sway force,

$$\text{SSE}_Y = \sum_i w_i (Y'(v', r', \dot{v}', \dot{r}') - Y'_i)^2, \quad (6.3)$$

where  $i$  denotes the  $i^{th}$  datum,  $Y'(v', r', \dot{v}', \dot{r}')$  is the Taylor series expansion evaluated in the corresponding condition and  $Y'_i$  is the result considered. The weighting function,  $w_i$ , is taken as the inverse of the number of point in the results used. The weighted root mean square is

$$E_{RMS,Y} = \sqrt{\frac{\text{SSE}_Y}{\sum_i w_i}}. \quad (6.4)$$

This method allows different sets of results to be combined to yield a set of manoeuvring derivatives. To see the influence of the motion frequency on the derivatives, each simulation and experimental data was treated separately. It was found upon trials and errors that the best results were obtained when the fitting was performed using the maximum number of periods from the PMM simulation or test.

Figure 6.2 shows a typical sway force and yaw moment data set, both from experimental and numerical results. Results of the fitting operation are presented on figure 6.3 and 6.4 for the experimental and the CFD data, respectively. The script and its verification are presented in appendix C.6.

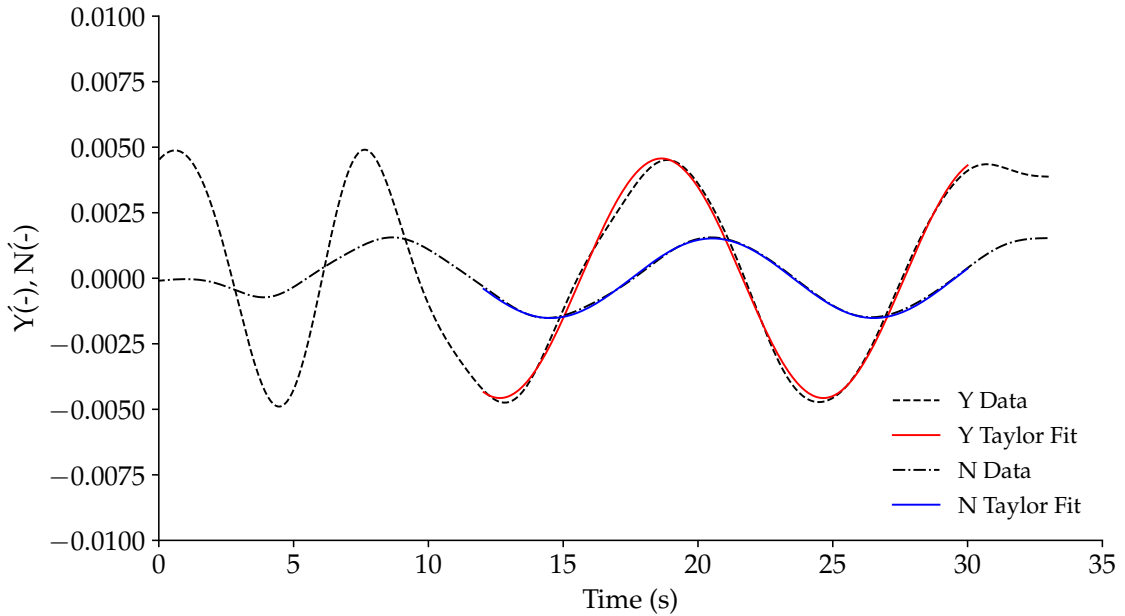


**Figure 6.3:** Experimental data fitting for the pure yaw simulation ( $T = 12$  s). Sway force and yaw moment are presented nondimensional.

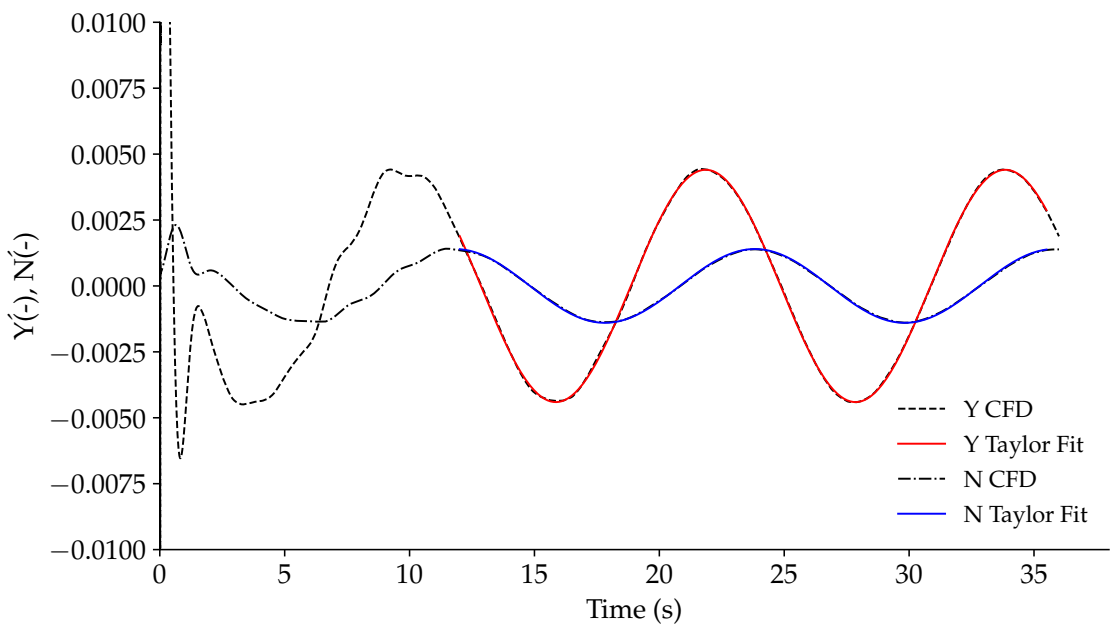


**Figure 6.4:** CFD data fitting for the pure yaw simulation ( $T = 12$  s). The large peaks observed at  $t = 0$  s are due to the motion initialization. Sway force and yaw moment are presented nondimensional.

**Table 6.1:** Mesh and solver metrics for the planar motion mechanism simulations.

Mesh	Cells ( $\times 10^6$ )	CPU Time (Hours)	$L_2$ Norm Pressure
Coarse	4.102899	333:05:18	$1.0535 \times 10^{-4}$
Standard	6.430814	416:48:38	$2.4976 \times 10^{-5}$
Fine	8.102968	511:49:55	$1.1555 \times 10^{-5}$

## 6.3 Verification and Validation

The verification and validation process was performed on the planar motion mechanism in pure sway with a period of oscillation of 12 s. Two other meshes were produced based on the standard mesh described in section 4.2.2. A similar coarsening and refinement approach as in the static drift simulation was applied. In addition, the overlap of the overset in the background also had to be adjusted to ensure that the cell size between them were of similar size. An appropriate target refinement ratio of  $\sqrt{2}$  was chosen, to limit the size of the meshes. Due to the mesh topology, this exact ratio could not be maintained.

### 6.3.1 Global Quantities

The results are presented for three meshes with a cell count of 4.1, 6.4 and 8.1 M cells, for the coarse ( $N_3$ ), standard ( $N_2$ ) and fine ( $N_1$ ) mesh, respectively. This corresponds to refinement ratios of  $r_{21} = 1.26$  and  $r_{32} = 1.56$ . The manoeuvring derivatives were calculated for the three meshes, using the same period of motion each time for the fitting. The use of manoeuvring derivatives is believed to give a more accurate representation of the mesh resolution as opposed to a single force measurement taken arbitrarily during the motion for unsteady simulations.

Iterative convergence between each time-step is achieved to at least an order of  $10^{-3}\%$ S based on the  $L_2$  norm of the pressure change between consecutive iterations relative to the total pressure force on the hull, see table 6.1. Again, this is below the expected grid uncertainty and can be safely neglected when calculating the corrected simulation results. Moreover, the inclusion of the iterative uncertainty in the corrected solution is not expected to have a measurable impact on the resulting oscillatory coefficients.

The results of the grid sensitivity study for the planar motion mechanism simulation in pure sway are presented in table 6.2. All but one of the variables considered show oscillatory convergence (O). Monotonic convergence is achieved only for  $\hat{N}'_v$ , thus the grid convergence index is only valid for this variable, it is however presented for all of them. Oscillatory convergence usually implies that the meshes are not in the asymptotic range, this might be the result of the coarse mesh not being able to accurately capture all the

**Table 6.2:** Grid convergence study for the planar motion mechanism in pure sway ( $T=12s$ ,  $y_0 = 0.2026m$ ).

	$\tilde{Y}'_v$	$\tilde{N}'_v$	$\tilde{Y}'_{\dot{v}}$	$\tilde{N}'_{\dot{v}}$
$\hat{S}_{k1}$ (Fine)	-0.013702	-0.014182	-0.009855	-0.000479
$\hat{S}_{k2}$ (Standard)	-0.013677	-0.014194	-0.009988	-0.000466
$\hat{S}_{k3}$ (Coarse)	-0.014225	-0.01416	-0.009820	-0.000440
Convergence <sup>a</sup>	O	O	O	M
$p$ (apparent order)	<b>21.51</b>	<b>1.99</b>	<b>7.87</b>	<b>0.25</b>
$\hat{S}_{\text{ext}}^{21}$	-0.013708	-0.009051	-0.014168	-0.001152
$e_a^{21}$	0.18	1.35	0.08	2.71
$e_{\text{ext}}^{21}$	0.04	8.88	0.10	58.43
<b>GCI</b> <sup>b</sup> <sub>standard</sub>	<b>0.21<sup>b</sup></b>	<b>6.06<sup>b</sup></b>	<b>0.13<sup>b</sup></b>	<b>184.10</b>

<sup>a</sup> M: monotonic convergence, O: oscillatory convergence, D: divergence

<sup>b</sup> Strictly speaking the GCI cannot be calculated for results showing oscillatory convergence.

physics. A finer mesh would be required to estimate the upper and lower bound of the solution oscillations to estimate the grid uncertainty, this could not be performed due to a lack of time but would be required to properly verify the results. It can however be noted that all oscillatory coefficients show good agreement between each mesh considered, with the standard deviation being 1.98% of the value of the standard mesh, see table 6.4.

The reason for the observed oscillatory behaviour could arise from the limitation of the method used for unsteady flow simulations, and not really reflect actual oscillations in the convergence of the variables. This was also observed by Carrica et al. (2016) who performed a convergence study for unsteady ship simulations (zigzag manoeuvre) and obtained oscillatory convergence for most of their variables, while the same variables showed monotonic convergence when the convergence study was performed on a self-propulsion simulation utilizing the same meshes. Other methods are used in the literature to compare convergence of unsteady simulations, for example Oldfield et al. (2015) verified their results by looking at the convergence of the Fourier coefficients obtained from the fitting of the data with a 3<sup>rd</sup> order Fourier series.

Because numerical uncertainties cannot be accurately estimated for the variables, a proper validation of the results cannot be made. It is however possible to calculate the comparison error  $E$  between the oscillatory coefficients obtained from CFD to the one from the experimental data. This is presented in table 6.3, where the comparison error is denoted by  $\epsilon$  for consistency with previous tables. The two periods are treated independently. Agreement for the sway velocity and acceleration dependent coefficients is better than for rotatory dependent coefficients.

The oscillatory coefficients obtained, see table 6.3, are in acceptable agreement with

**Table 6.3:** Oscillatory coefficients from planar motion mechanism simulations against experimental data. Note that  $\epsilon$  denotes the comparison error otherwise noted as  $E$ . MOERI results are compared to the 12 s period results.

Derivative	Present (CFD)		Experimental		
			NMRI		MOERI
	12 s	6 s	12 s	6 s	10 s
$\tilde{Y}'_v$	-0.013677	-0.01438	-0.01519	-0.01638	-0.016190
$\epsilon$ (%D)	-	-	-9.96	-12.21	-15.52
$\tilde{Y}'_{\dot{v}}$	-0.014194	-0.01470	-0.01439	-0.01868	-0.015104
$\epsilon$ (%D)	-	-	-1.36	-21.31	-6.02
$\tilde{N}'_v$	-0.009988	-0.01076	-0.01070	-0.01318	-0.00875
$\epsilon$ (%D)	-	-	-6.65	-18.36	14.15
$\tilde{N}'_{\dot{v}}$	-0.000466	-0.000418	-0.00051	-0.00076	-0.000785
$\epsilon$ (%D)	-	-	-8.63	-45.0	-40.64
$\tilde{Y}'_r$	0.002862	0.002696	0.004305	a	0.004720
$\epsilon$ (%D)	-	-	-33.52	-	-39.36
$\tilde{Y}'_{\dot{r}}$	-0.000567	-0.000512	-0.003124	a	-0.001428
$\epsilon$ (%D)	-	-	-81.85	-	-60.29
$\tilde{N}'_r$	-0.002132	-0.002461	-0.002524	a	-0.003115
$\epsilon$ (%D)	-	-	-15.53	-	-31.56
$\tilde{N}'_{\dot{r}}$	-0.000676	-0.001005	-0.001134	a	-0.00080
$\epsilon$ (%D)	-	-	-40.39	-	15.5

<sup>a</sup> Raw experimental results is problematic, and thus not included.

**Table 6.4:** Oscillatory coefficients from planar motion mechanism simulations in pure sway ( $T=12s$ ) with for different mesh sizes and turbulence models. Error expressed relative to the standard solution ( $k-\omega$  SST).

Derivative	Coarse	Standard		Fine
		$k-\omega$ SST	Realizable $k-\epsilon$	
$\tilde{Y}'_v$	-0.014225	-0.013677	-0.013902	-0.013702
$\epsilon$ (%S)	4.01	-	1.64	0.18
$\tilde{Y}'_{\dot{v}}$	-0.014161	-0.014194	-0.014267	-0.014182
$\epsilon$ (%S)	-0.23	-	0.51	-0.08
$\tilde{N}'_v$	-0.009820	-0.009988	-0.009939	-0.009855
$\epsilon$ (%S)	-1.68	-	-0.06	-1.33
$\tilde{N}'_{\dot{v}}$	-0.000440	-0.000466	-0.000407	-0.000479
$\epsilon$ (%S)	-5.58	-	-12.6	2.79

experimental data. The frequency dependence of the oscillatory coefficients seems to be captured, in pure sway, the global increase of oscillatory coefficients with reduction in the motion frequency is captured. For the pure yaw PMM, due to the problematic raw data, such conclusions cannot be drawn. Those coefficients could be later used to determine their associated slow motion derivatives for use in manoeuvring simulations.

### Turbulence Sensitivity

Table 6.4 shows the results obtained with the three meshes used for the grid convergence study as well as a simulation using the Realizable  $k-\epsilon$  turbulence model. The two turbulence models used show good agreement with each other. The largest deviation occurs for  $\tilde{N}'_v$ , this is also the value which shows the largest differences between the mesh density considered. No clear tendency can be observed whether velocity or acceleration depended derivatives are more sensitive to mesh density or turbulence closure. Both turbulence models can be expected to yield similar results for this type of flow problems, as their formulations are not too dissimilar (Wilcox, 1993). Additional investigation would be required to see if this pattern is repeated with a change of motion frequency, i.e. if there is a frequency dependency in the convergence of the turbulence model. It should be noted that the simulation using the Realizable  $k-\epsilon$  model showed larger values of the  $L_2$  norm of convergence, especially for the shear stress.

#### 6.3.2 Local Flow Quantities

Unfortunately, no experimental flow measurements are available for comparison purposes for unsteady model tests for the KVLCC2. Only numerical results provide readily accessible information on the flow field generated by the model during PMM tests. Therefore no local flow measurements can be used to validate the simulations.

### 6.4 Additional Investigations

Additional investigations were performed on the KVLCC2 equipped with a rudder, as described in section 4.1.5. The results are presented in table 6.5. The contribution of the rudder to the sway velocity derivatives follows a similar tendency as in the static drift simulations, however the magnitude is reduced, both for the sway force and yaw moment. One can also note that the rudder contributes much less to the acceleration dependent derivatives than to the velocity dependent ones, especially for the sway force. For the yaw moment, because the rudder has the effect of reducing the value of the derivatives and because the magnitude is small, the differences can be significant.

The trend observed for sway velocity dependent derivatives is different for rotatory dependent derivatives. The addition of the rudder has the effect of increasing both the

sway force and yaw moment contribution, whereas it had the effect of reducing the yaw moment in the pure sway PMM. This can easily be explained because during PMM in pure sway, sway force and yaw moment have roughly the same magnitude, as opposed to PMM in pure yaw, where the sway force is typically much larger than the yaw moment, due to the contribution of the bow and stern of the ship to the moment cancelling each other out, while they are simply added for the force.

## 6.5 Discussion

This chapter expose the results of the PMM simulations used to derive the oscillatory coefficients of the KVLCC2. Similar levels of iterative convergence were achieved for these unsteady simulations as for the static drift simulations. However, the time-step and inner iteration used are much more refined. Despite showing good levels of iterative convergence, oscillations were observed in all but one of the variables considered for the grid convergence study. The Richardson extrapolation used earlier cannot be used in this case, and additional results would be required to estimate the grid uncertainties based on the lower and upper bound of the solution oscillation. Or perhaps, the observed behaviour is due to the limitations of the verification approach, as discussed previously. It should be noted that proper verification and validation is not usually performed for PMM simulations, and that the mesh sizes considered herein are of similar order as the ones considered in for example, He et al. (2016) and Kim et al. (2015).

The agreement for the oscillatory coefficients from the pure sway test is acceptable, showing similar agreement as the slow motion derivatives discussed previously. Velocity dependent derivatives are better predicted than acceleration dependent ones, mostly because their magnitude is larger. The trend observed in the static drift results that the yaw moment shows better agreement, at least for velocity derivatives. Agreement for the 12 s period is also better than with the period of 6 seconds, this might be due to the experimental uncertainties in model tests being larger for smaller motion periods. As discussed previously, the frequency dependence of the oscillatory coefficient is captured.

In pure yaw simulations, the agreement deteriorates. The tendencies are accurately captured by the CFD simulations but large discrepancies are present for certain derivatives, namely  $\tilde{Y}'_r$  and  $\tilde{N}'_r$ . Comparison with experimental results for the other oscillation period ( $T = 6$  s) could not be made. The uncertainty in model tests can also be expected to be larger for the pure yaw case. This was discussed previously (section 2.1), but improvements for the pure yaw case can be observed for the results of the present study, compared to, for examples results from He et al. (2016). To properly validate the time-step and inner iteration chosen, a proper sensitivity study would be required.

While no large differences were observed between the results of the different turbulence models used, the use of different turbulence strategies (i.e. hybrid RANS/LES, DDES)

could improve the predictions. As opposed to the argument provided in the discussion of the slow motion derivatives in the previous chapter, correctly modelling the interactions of the coherent flow structures, such as the bilge vortices, with the ship in unsteady motion could be critical, and this cannot accurately be done using RANS approaches. A similar point was raised by Oldfield et al. (2015), who argued that inclusion of local flow history effects, i.e. roll and decay of vortices, could only improve force predictions. They also suggested that the manoeuvring derivatives obtained from unsteady simulations would only be beneficial if used for simulating real manoeuvres where similar flow-history are expected. An example would be to use PMM results to simulate zigzag manoeuvres, and static drift simulation results, or even better, results from rotating arm simulations for turning circle manoeuvres, due to the similarity in the flow-history.

From the set of oscillatory coefficients obtained, a set of slow motion derivatives could be extracted to be used with the equations of motion to simulate standard manoeuvres.

**Table 6.5:** Influence of rudder on oscillatory coefficients from PMM in pure sway and yaw. Difference ( $\epsilon$ ) is expressed relative to the rudder contribution to the oscillatory coefficients of the hull with rudder (S).

Derivative	Bare Hull		Hull with Rudder		Rudder Contribution	
	12 s	6 s	12 s	6 s	12 s	6 s
$\tilde{Y}'_v$	-0.013677	-0.01438	-0.015124	-0.01835	-0.00145	-0.00367
$\epsilon$ (%S)	-	-	-	-	9.58	20.0
$\tilde{Y}'_{\dot{v}}$	-0.014194	-0.01470	-0.014648	-0.01533	-0.000454	-0.00063
$\epsilon$ (%S)	-	-	-	-	3.1	4.1
$\tilde{N}'_v$	-0.009988	-0.01076	-0.009064	-0.00879	0.000924	0.00197
$\epsilon$ (%S)	-	-	-	-	-10.2	-22.41
$\tilde{N}'_{\dot{v}}$	-0.000466	-0.000418	-0.000212	-0.000104	0.000254	0.000314
$\epsilon$ (%S)	-	-	-	-	-119.8	-301.9
$\tilde{Y}'_r$	0.002862	0.002696	0.003854	0.004688	0.000992	0.001992
$\epsilon$ (%S)	-	-	-	-	-	-
$\tilde{Y}'_{\dot{r}}$	-0.000567	-0.000512	-0.000370	-0.000211	0.000142	0.000301
$\epsilon$ (%S)	-	-	-	-	-	-
$\tilde{N}'_r$	-0.002132	-0.002461	-0.002633	-0.003411	-0.000501	-0.00095
$\epsilon$ (%S)	-	-	-	-	-	-
$\tilde{N}'_{\dot{r}}$	-0.000676	-0.001005	-0.000761	-0.001158	-0.000085	-0.000153
$\epsilon$ (%S)	-	-	-	-	-	-

# Chapter 7

## Conclusion and Future Work

This chapter provides conclusions to the results obtained in this study. Link to the aim and objective are made, and the limitations of the present study are discussed. Finally, recommendations for future work are given.

With regards to the task assigned in the *Aim and Objectives*, the slow motion derivatives and oscillatory coefficients for the KVLCC2 have been effectively acquired by numerically replicating static drift and planar motion mechanism tests. Different numerical aspects have been investigated, and the difference in the results obtained contrasted. The rudder study, which was originally not included in this work was undertaken due to the progress made. From the study undertaken the following conclusion can be drawn.

### 7.1 Conclusions

RANS methods have been used to derive manoeuvring coefficients (SMD's and OC's) for a benchmark ship, the KVLCC2, by mean of static drift and planar motion mechanism simulations in pure sway and yaw. The results obtained showed that CFD is a valuable tool for this purpose but some numerical challenges are still present with the methods and computational power available nowadays, they are discussed below.

- While more physical fidelity is gained by modelling the free surface it comes at the cost of a computational time being typically 10 times larger compared to the double-body approach. The unsteady approach required to model the free surface poses additional problems, iterative convergence can hardly be achieved at the same level as a steady state simulation. This leads to both results being very similar, especially for ships operating at low Froude numbers. The influence of the free surface might be more important for PMM simulations, where the frequency of oscillation could lead to complex wave interactions that could have a significant influence on the resulting coefficients.

- Judging convergence of the static drift simulation, despite also being unsteady, proved much easier than for unsteady PMM simulations, as forces and moments, as well as the residuals can be used to assess the convergence of the simulations. For unsteady PMM, where the aimed result is an harmonic force/moment, it is much more difficult to judge the convergence of the results. The  $L_2$  Norm approach used showed to be relatively straightforward to implement and is believed to be more representative of iterative convergence than standard residuals.
- Spatial and temporal discretization errors were found to be small for the static drift simulations, even with large values of time-step, the predicted forces and moment showed good agreement with the other simulations utilizing finer time-step, only the free surface representation was altered. Turbulence closure proved not to have too much influence on the forces predicted, with the exception of the surge force prediction of the Spalart-Allamaras model, good agreement was obtained.
- Verification and validation was performed for both the static drift and the planar motion mechanism tests, for the later, the manoeuvring derivatives have been used as the variables to verify. The limitations of the verification and validation process for unsteady simulations have been seen, additional methods would be required to asses the validity of those simulations.
- The influence of an undeflected rudder was correctly captured by the RANS method, proper verification and validation of the results would be required.
- Finally the manoeuvring derivatives obtained in the present study show similar or better agreement compared to results presented in the literature. They could therefore be utilized to simulate ship manoeuvre.

## 7.2 Recommendations for Future Work

While this investigation tried to be comprehensive, many aspects could not be investigated due to the time constraint, and some of the results obtained required additional investigation. The following recommendations are made to improve those results; as well as to suggest new routes of study.

- This study made extensive use of the wall function approach, ultimately the aim would be to fully resolve the boundary layer. This could be combined with free surface capturing methods, such as the VOF to reduce the modelling assumptions.
- The set of manoeuvring coefficients derived in this study were for the model, the aim would be to be able to derive them for the ship, bypassing the uncertainties associated with the scaling of the results.

- Specific CFD codes for resistance calculations have been created (Hoekstra, 1998), those codes allow much more efficient computations for this specific case, a similar approach could be used to derive a purposely build CFD code for manoeuvring, which would greatly enhance CFD manoeuvring predictions during the design of a new ship.
- While RANS approaches were shown to be able to predict unsteady flow phenomena relatively well, use of scale-resolving simulations for captive model simulations could greatly enhance the results, once the problem of computational power is solved.
- Free-running simulations, despite being also prohibited at present time due to the required computational power, might be the norm in a close future, constant development of numerical methods (free surface modelling, turbulence closure, numerical schemes, etc.) and hardware is therefore required to achieve this ambitious goal.

# References

- Abdel-Maksoud, M., Muller, V., Xing, T., Toxopeus, S., Stern, F., Petterson, K., Tormalm, M., Kim, S., Aram, S., Gietz, U., et al. (2015). “Experimental and Numerical Investigations on Flow Characteristics of the KVLCC2 at 30 Drift Angle”. In: *Proceedings of the 5th World Maritime Technology Conference, Providence, Rhode Island, USA*.
- Abkowitz, M. A. (1964). *Lectures on ship hydrodynamics–Steering and manoeuvrability*. Tech. rep.
- Bertram, V. (2012). *Practical ship hydrodynamics*. Elsevier.
- Carrica, P. M., Castro, A. M., and Stern, F. (2010). “Self-propulsion computations using a speed controller and a discretized propeller with dynamic overset grids”. In: *Journal of marine science and technology* 15.4, pp. 316–330.
- Carrica, P. M., Mofidi, A., Eloot, K., and Delefortrie, G. (2016). “Direct simulation and experimental study of zigzag maneuver of KCS in shallow water”. In: *Ocean Engineering* 112, pp. 117–133.
- Carrica, P. M., Stern, F., and Fu, H. (2011). “Computations of self-propulsion free to sink and trim and of motions in head waves of the KRISO Container Ship (KCS) model”. In: *Applied Ocean Research* 33.4, pp. 309–320.
- Celik, I. B., Ghia, U., Roache, P. J., Freitas, C. J., Coleman, H., and Raad, P. E. (2008). “Procedure for estimation and reporting of uncertainty due to discretization in CFD applications”. In: *Journal of fluids Engineering-Transactions of the ASME* 130.7.
- Choi, J. and Yoon, S. B. (2009). “Numerical simulations using momentum source wave-maker applied to RANS equation model”. In: *Coastal Engineering* 56.10, pp. 1043–1060.
- Clark, D. (1972). “A Two-Dimensional Strip Method for Surface Ship Hull Derivatives: Comparison of Theory with Experiments on a Segmented Tanker Model”. In: *International Symposium on Directional Stability and Control of Bodies Moving in Water*, pp. 43–51.
- Clarke, D. (1983). “The application of manoeuvring criteria in hull design using linear theory”. In: *Trans RINA* 125, pp. 45–68.
- Degani, D., Seginer, A., and Levy, Y. (1990). “Graphical visualization of vortical flows by means of helicity”. In: *AIAA journal* 28.8, pp. 1347–1352.

- Duman, S. and Bal, S. (2016). "Numerical Investigation of Viscous Effects on the Static PMM Tests of Ships". In: *2nd International Meeting on Recent Advances in Prediction Techniques for Safe Manoeuvring of Ships and Submarines, Istanbul, Turkey*.
- Eça, L. and Hoekstra, M. (2006). "On the influence of the iterative error in the numerical uncertainty of ship viscous flow calculations". In: *26th Symposium on Naval Hydrodynamics*, pp. 17–22.
- Ferziger, J. H. and Peric, M. (2012). *Computational methods for fluid dynamics*. Springer Science & Business Media.
- Gallagher, P., Marcer, R., Berhault, C., Jouette, C. de, Raven, H. C., Eça, L., Broberg, L., Janson, C-E., Gao, Q. X., Toxopeus, S., Alessandrini, B., Terwesga, T., Hoekstra, M., Streckwall, H., and Salvatore, F. (Apr. 2009). "Best Practice Guidelines for the application of Computational Fluid Dynamics in Marine Hydrodynamics". In: *VIRTUE - The Virtuel Tank Utility in Europe*.
- Hajivand, A. and Mousavizadegan, S. H. (2015). "Virtual simulation of maneuvering captive tests for a surface vessel". In: *International Journal of Naval Architecture and Ocean Engineering* 7.5, pp. 848–872.
- He, S., Kellett, P., Yuan, Z., Incecik, A., Turan, O., and Boulogeoris, E. (2016). "Manoeuvring prediction based on CFD generated derivatives". In: *Journal of Hydrodynamics, Ser. B* 28.2, pp. 284–292.
- Hirt, C. W. and Nichols, B. D. (1981). "Volume of fluid (VOF) method for the dynamics of free boundaries". In: *Journal of computational physics* 39.1, pp. 201–225.
- Hochbaum, A. C. and Uharek, S. (2014). "Prediction of the manoeuvring behaviour of the KCS based on RANS-simulated captive tests". In: *SIMMAN: workshop on the verification and validation of ship manoeuvring simulation methods*.
- Hochbaum, A. C. and Vogt, M. (2002). "Towards the simulation of seakeeping and maneuvering based computation of the free surface viscous ship flow". In: *Proceedings of the 24th Symposium on Naval Hydrodynamics, Fukuoka, Japan*.
- Hoekstra, M. (1998). "PARNASSOS: An efficient method for ship stern flow calculation". In: *Proceedings of Third Osaka Colloquium on Advanced CFD Applications to Ship Flow and Hull Form Design (OC'98)*, pp. 331–357.
- Hunt, J. C. R., Wray, A. A., and Moin, P. (1988). "Eddies, streams, and convergence zones in turbulent flows". In: *Center for Turbulence Research, Proceedings of the Summer Program 1988*, pp. 193–208.
- IMO, International Maritime Organisation (2002). "Standards for ship manoeuvrability". In: *Resolution MSC.137(76)*.
- Inoue, S. and Kijima, K. (1978). "The hydrodynamic derivatives on ship manoeuvrability in the trimmed condition". In: *ITTC 2*, pp. 87–92.

- ITTC, International Towing Tank Conference (2008). “Uncertainty Analysis in CFD Verification and Validation Methodology and Procedures”. In: *ITTC-Recommended Procedures and Guidelines* 7.5-03-01-01.
- ITTC, International Towing Tank Conference (2014). “Example for Uncertainty Analysis of Resistance Tests in Towing Tanks”. In: *ITTC-Recommended Procedures and Guidelines* 7.5-02-02-02.1.
- ITTC, International Towing Tank Conference (2011). “Practical Guidelines for Ship CFD Applications”. In: *ITTC-Recommended Procedures and Guidelines* 7.5-03-02-03.
- ITTC, International Towing Tank Conference (2017). “Guideline on Use of RANS Tools for Manoeuvring Prediction”. In: *ITTC-Recommended Procedures and Guidelines* 7.5-03-04-01.
- Kijima, K., Katsuno, T., Nakiri, Y., and Furukawa, Y. (1990). “On the manoeuvring performance of a ship with the parameter of loading condition”. In: *Journal of the society of naval architects of Japan* 1990.168, pp. 141–148.
- Kim, W. J., Van, S. H., and Kim, D. H. (2001). “Measurement of flows around modern commercial ship models”. In: *Experiments in fluids* 31.5, pp. 567–578.
- Kim, H., Akimoto, H., and Islam, H. (2015). “Estimation of the hydrodynamic derivatives by RANS simulation of planar motion mechanism test”. In: *Ocean Engineering* 108, pp. 129–139.
- Kume, K., Hasegawa, J., Tsukada, Y., Fujisawa, J., Fukasawa, R., and Hinatsu, M. (2006). “Measurements of hydrodynamic forces, surface pressure, and wake for obliquely towed tanker model and uncertainty analysis for CFD validation”. In: *Journal of Marine Science and Technology* 11.2, pp. 65–75.
- Larsson, L., Stern, F., and Bertram, V. (2003). “Benchmarking of computational fluid dynamics for ship flows: the Gothenburg 2000 workshop”. In: *Journal of Ship Research* 47.1, pp. 63–81.
- Lewis, E.V. (1989). *Principles of naval architecture: Vol. 3. Motions in Waves and Controllability*. Society of Naval Architects and Marine Engineers.
- Luo, W., Soares, G. S., and Zou, Z. (2016). “Parameter identification of ship maneuvering model based on support vector machines and particle swarm optimization”. In: *Journal of Offshore Mechanics and Arctic Engineering* 138.3, pp. 031101-1–031101-8.
- Menter, F. R. (1994). “Two-equation eddy-viscosity turbulence models for engineering applications”. In: *AIAA journal* 32.8, pp. 1598–1605.
- Miyata, H., Akimoto, H., and Hiroshima, F. (1997). “CFD performance prediction simulation for hull-form design of sailing boats”. In: *Journal of Marine science and technology* 2.4, pp. 257–267.
- Mofidi, A. and Carrica, P. M. (2014). “Simulations of zigzag maneuvers for a container ship with direct moving rudder and propeller”. In: *Computers & Fluids* 96, pp. 191–203.

- Muzaferija, S. (1998). "Computation of free surface flows using interface-tracking and interface-capturing methods". In: *Nonlinear water-wave interaction. Computational Mechanics, Southampton*.
- Oldfield, C., Larvaei, M. M., Kendrick, A., and McTaggart, K. (2015). "Prediction of Warship Manoeuvring Coefficients using CFD". In: *World Maritime Technology Conference*.
- Pope, S. B. (2001). *Turbulent flows*. Cambridge University Press.
- Robertson, D. G. E., Barden, J. M., and Dowling, J. (1993). "Response characteristics of different Butterworth low-pass digital filters". In: *Journal of Biomechanics* 26.3, pp. 299–299.
- Sakamoto, N. and Kume, K. (2014). "Zig-zag simulations of KVLCC2 by CFD-systems based maneuvering prediction method". In: *Lectures of the Japan Society of Naval Architects and Ocean Engineers* 19, pp. 227–230.
- Schlichting, H. (1979). "Boundary-layer theory, 7th. editon". In: *McCraw-Hill Book Co., New York*.
- Shen, Z. and Korpus, R. (2015). "Numerical Simulations of Ship Self-Propulsion and Maneuvering Using Dynamic Overset Grids in OpenFOAM". In: *Tokyo 2015 A Workshop on CFD in Ship Hydrodynamics. Presented at the Tokyo 2015 A Workshop on CFD in Ship Hydrodynamics, Tokyo, Japan*.
- Shenoi, R. R., Krishnankutty, P., Selvam, R. P., and Kulsreshtha, A. (2013). "Prediction of maneuvering coefficients of a container ship by numerically simulating HPMM using RANSE based solver". In: *Third International Conference on Ship Manoeuvring in Shallow and Confined Water, Jun*, pp. 3–5.
- Shih, T.-H., Liou, W. W., Shabbir, A., Yang, Z., and Zhu, J. (1995). "A new  $k-\epsilon$  eddy viscosity model for high reynolds number turbulent flows". In: *Computers & Fluids* 24.3, pp. 227–238.
- Siemens, PLM Software (2017). "Star-CCM+ Theroy Guide". In: *Star-CCM+ Documentation* 12.04, pp. 7258–7795.
- SIMMAN (2014). "Workshop on Verification and Validation of Ship Manoeuvring Simulation Methods". In: Lyngby, Denmark. URL: <https://simman2014.dk/>.
- Simonsen, C. D., Otzen, J. F., Klimt, C., Larsen, N. L., and Stern, F. (2012). "Maneuvering predictions in the early design phase using CFD generated PMM data". In: *29th symposium on naval hydrodynamics*, pp. 26–31.
- SNAME (1950). "Nomenclature for treating the motion of a submerged body through a fluid". In: *New York: Technical and Research Bulletin*, pp. 1–5.
- Spalart, P. R. and Allmaras, S. R. (1992). "A one-equation turbulence model for aerodynamic flows". In: *30th aerospace sciences meeting and exhibit*, p. 439.
- Star CCM+, Cd-Adapco (2013). "Best Practice Workshop: Overset Meshing". In: *STAR South East ASIAN Conference, Kual Lumpur, November 11-12*.

- Stern, F., Wilson, R. V., Coleman, H. W., and Paterson, E. G. (2001). “Comprehensive approach to verification and validation of CFD simulations—part 1: methodology and procedures”. In: *Journal of fluids engineering* 123.4, pp. 793–802.
- Temarel, P. (2017). “Manoeuvring of Ships”. In: *SESS3022 Ship Manoeuvring and Control Lecture Notes*.
- Toxopeus, S., Simonsen, C.D., Guilméneau, E., Visonneau, M., Xing, T., and Stern, F. (2013). “Investigation of water depth and basin wall effects on KVLCC2 in manoeuvring motion using viscous-flow calculations”. In: *Journal of Marine Science and Technology* 18.4, pp. 471–496.
- Turnock, S. R., Phillips, A. B., and Furlong, M. (2008). “URANS simulations of static drift and dynamic manoeuvres of the KVLCC2 tanker”. In: *SIMMAN 2008: workshop on verification and validation of ship manoeuvring Simulation Methods*.
- Ubbink, O. and Issa, R. I. (1999). “A method for capturing sharp fluid interfaces on arbitrary meshes”. In: *Journal of Computational Physics* 153.1, pp. 26–50.
- Wilcox, D. C. (1993). *Turbulence modeling for CFD*. Vol. 2. DCW industries La Canada, CA.
- Xing, T., Bhushan, S., and Stern, F. (2012). “Vortical and turbulent structures for KVLCC2 at drift angle 0, 12, and 30 degrees”. In: *Ocean Engineering* 55, pp. 23–43.
- Yasukawa, H. and Yoshimura, Y. (2015). “Introduction of MMG standard method for ship maneuvering predictions”. In: *Journal of Marine Science and Technology* 20.1, pp. 37–52.
- Zou, L., Larsson, L., and Orych, M. (2010). “Verification and validation of CFD predictions for a manoeuvring tanker”. In: *Journal of Hydrodynamics, Ser. B* 22.5, pp. 438–445.

## **Appendix A**

## **Literature Review**

An exclusive summary of part of the literature review is presented on the following pages.



10	N. Sakamoto, K. Kume. Zig-Zag Simulations of KVLC/C2 by CFD-Systems based Maneuvering Prediction Method. JASNAOE Full Annual Meeting At: Nagasaki, JAPAN	2014	CFD is used to generate maneuvering derivatives which are used in mathematical models to simulate zig-zag manoeuvres.	317	KVLC/C2 SURF	Modular type mathematical model (MMG) is utilized (JASNAOE).
11	R.R. Shenoi, P. Krishnakutty, R.P. Selvam, A. Kulasekhar. Prediction of Maneuvering Coefficients of a Container Ship by Numerically Simulating the HPMM using RANS based Solver. Third International Conference on Ship Maneuvering in Shallow and Confined Water.	2013	Determination of the linear, non-linear and coupled hydrodynamic derivative of a container ship (S175) with the aid of CFD by replicating HPMM test.	1295	S175 Star CCM+ turbulent model used. (1.2-0.5M) cells used for the whole simulation. Forces computed in ship fixed coordinate system. Fourier series mode used to determine derivatives.	Computational domain as ITTC. No free surface modeling (Fr=0.15) for static test. VoF approach for pure sway, k-omega SST turbulent model used. (1.2-0.5M) cells used for the whole simulation. Forces computed in ship fixed coordinate system. Fourier series mode used to determine derivatives.
12	A. Cure-Hochbaum, S. Ulurek. Prediction of the manoeuvring behaviour of the KCS based on RANS virtual captive tests. SIMULIA 2014	2014	Derivatomeuvering derivatives from static and dynamic CFD test to simulated manouevres of a ship.	179	KCS Neptune Fine/Marine	Use of standard k-omega turbulence model with wall functions. The free surface is simulated using the level set technique. Grid ranging from 0.45-3.7M elements. mesh sensitivity study undertaken.
13	B. d'Aure, B. Malhotra, C. Hirsch. Resistance and Seakeeping CFD simulations for the Korean Container Ship. Proceedings of the Tokyo 2015 SIMULIA	2015	Investigate the influence of the physical and numerical parameters in the prediction of resistance and seakeeping with V&Y.	-	KCS	Model not free to trim and heave during the tests. Included propeller influence via a data base of propeller performance for different hull yaw factor and advance coefficients. Abowtrav coefficient to third order. Fourier analysis of time series for dynamic test.
14	L. Zou, L. Larsson, M. Orych. Verification and validation of CFD predictions for a manoeuvring tanker. Journal of Hydrodynamics 22(5)	2010	Verification and validation for a tanker without appendages at different drift angles and water depths.	7.5	KVLC/C2 SHIPFLOW	Steady RANS simulation, neglecting free surface, trim and heave. Discretization errors in the order of 5% for the unsteady seakeeping simulation. Y- around 50. Mesh size ranging from 0.26-6.23M. Use of the VoF method together with a k-omega SST turbulence model. Simulation of 1/2 ship as only symmetric motions are considered. Ship is accelerated, not flow.
15	M. Abdell-Maksoud et al. Experimental and Numerical Investigations on Flow Characteristics of a KVLC/C2 at 30° Drift Angle. Proceedings of the 5th World Maritime Technology Conference, Providence, Rhode Island, USA	2015	In depth investigation of the flow features around a tanker at very large drift angles. Comparison of RANS, DES and LES simulations against wind tunnel results. Discretization errors are investigated as well as the effects of turbulence models.	10.3	KVLC/C2 N-A	Drift angles ranging from 0.6° to non-dimensional water depth of 1.2-8.3 (h/T). Verification was performed at 4° drift in the shallowest and deepest conditions. Validation was performed for every case.
16	A. Hajivandi, S.H. Mousavizadeh. Virtual simulation of manoueuvering tests for a surface vessel. International Journal of Naval Architecture and Ocean Engineering Volume 7, Issue 5, Pages 848-872	2015	Investigate the use of CFD to derive the force coefficient from PMM test to predict manouevring characteristics of a ship.	6	DTMB-5415 Star CCM+ grid	The experiment focus on the local and global flow structure around the KVLC/C2 hull at a drift angle of 30°. PV, LDA, smoke test and oil film are used to locate, quantify and study the strength of the vortex, and the separation of the flow resulting from this large drift angle. Double hull simulations.





## Appendix B

# Turbulence Models

The following present the details of the different turbulence closure models used. For a complete explanation of the implementation of the different models, refer to Siemens (2017).

### B.1 $k-\omega$ SST

Menter's formulation of the  $k-\omega$  turbulence model is used (Menter, 1994), where the turbulent kinematic energy  $k$  is given by

$$\frac{Dk}{Dt} = \tau_{ij} \frac{\partial u_i}{\partial x_j} - \beta^* \rho \omega k + \frac{\partial}{\partial x_j} \left[ (\mu + \sigma_{k1} \mu_t) \frac{\partial k}{\partial x_j} \right], \quad (\text{B.1})$$

and the specific dissipation rate  $\omega$ ,

$$\begin{aligned} \frac{D\rho\omega}{Dt} &= \frac{\gamma}{\nu_t} \tau_{ij} \frac{\partial u_i}{\partial x_j} - \beta \rho \omega^2 + \frac{\partial}{\partial x_j} \left[ (\mu + \sigma_\omega \mu_t) \frac{\partial \omega}{\partial x_j} \right] \\ &\quad + 2\rho(1 - F_1) \sigma_{\omega 2} \frac{1}{\omega} \frac{\partial k}{\partial x_j} \frac{\partial \omega}{\partial x_j}. \end{aligned} \quad (\text{B.2})$$

$F_1$  is a blending function that calculates the new model constants  $\phi$  from the constant  $\phi_1$  and  $\phi_2$ ,

$$\phi = F_1 \phi_1 + (1 - F_1) \phi_2. \quad (\text{B.3})$$

The turbulent viscosity is calculated using the turbulent kinetic energy and the specific dissipation rate

$$\nu_t = \frac{a_1 k}{\max(a_1 \omega, \Omega F_2)}, \quad (\text{B.4})$$

with

$$F_2 = \tanh(\arg_2^2), \quad (\text{B.5})$$

where,

$$arg_2 = \max \left( 2 \frac{\sqrt{k}}{0.09\omega y}; \frac{500\nu}{y^2\omega} \right). \quad (\text{B.6})$$

The constant of set  $\phi_1$  are (SST inner):

$$\begin{aligned} \kappa &= 0.41 & \beta^* &= 0.09 & \beta_1 &= 0.0750 & \sigma_{k1} &= 0.85 \\ \sigma_{\omega 1} &= 0.5 & a_1 &= 0.31 & \gamma_1 &= \beta_1/\beta^* - \sigma_{\omega 1}\kappa^2/\sqrt{\beta^*} \end{aligned}$$

The constant of set  $\phi_2$  are (standard  $k-\epsilon$ ):

$$\begin{aligned} \kappa &= 0.41 & \beta^* &= 0.09 & \beta_2 &= 0.0828 & \sigma_{k2} &= 1.0 \\ \sigma_{\omega 2} &= 0.856 & & & \gamma_2 &= \beta_2/\beta^* - \sigma_{\omega 2}\kappa^2/\sqrt{\beta^*} \end{aligned}$$

## B.2 Realizable $k-\epsilon$

The realizable formulation of the  $k-\epsilon$  proposed by Shih et al. (1995) is used. This formulation offers improved results for boundary layer flows under adverse pressure gradients compared to the standard version. It is used with a blended two-layer wall function approach. The eddy viscosity is defined as:

$$\mu_t = \rho C_\mu \frac{k^2}{\epsilon} \quad (\text{B.7})$$

where the transport equation for the turbulent kinetic energy  $k$  is

$$\frac{D\rho k}{Dt} = \frac{\partial}{\partial x_j} \left[ \left( \mu + \frac{\mu_t}{\sigma_k} \right) \frac{\partial k}{\partial x_j} \right] - \rho \overline{u'_i u'_j} \frac{\partial u_j}{\partial x_i} + P_b - \rho \epsilon - Y_M + S_k, \quad (\text{B.8})$$

and for the turbulent dissipation rate

$$\frac{D\rho \epsilon}{Dt} = \frac{\partial}{\partial x_j} \left[ \left( \mu + \frac{\mu_t}{\sigma_\epsilon} \right) \frac{\partial \epsilon}{\partial x_j} \right] + \rho C_1 S_\epsilon - \rho C_2 \frac{\epsilon^2}{k + \sqrt{\nu \epsilon}} + C_{1\epsilon} \frac{\epsilon}{k} C_{3\epsilon} P_b + S_\epsilon. \quad (\text{B.9})$$

The different coefficients are defined as

$$\begin{aligned} C_\mu &= \frac{1}{A_0 + A_s \frac{kU^*}{\epsilon}} & U^* &\equiv \sqrt{S_{ij}S_{ij} + \tilde{\Omega}_{ij}\tilde{\Omega}_{ij}} \\ \tilde{\Omega}_{ij} &= \Omega_{ij} - 2\epsilon_{ijk}\omega_k & \Omega_{ij} &= \overline{\Omega_{ij}} - \epsilon_{ijk}\omega_k \\ \phi &= \frac{1}{3} \cos^{-1}(\sqrt{6}W) & W &= \frac{S_{ij}S_{jk}S_{ki}}{\tilde{S}^3} \\ \tilde{S} &= \sqrt{S_{ij}S_{ij}} & S_{ij} &= \frac{1}{2} \left( \frac{\partial u_j}{\partial x_i} + \frac{\partial u_i}{\partial x_j} \right), \end{aligned} \quad (\text{B.10})$$

with the following constant

$$C_{1\epsilon} = 1.44 \quad C_2 = 1.9 \quad \sigma_k = 1.0 \quad \sigma_\epsilon = 1.2.$$

This model differs in its treatment of  $C_\mu$  which is a variable here but is a constant in the standard  $k-\epsilon$  model ( $C_\mu = 0.09$ ). This enables additional mathematical conditions on the Reynolds stresses to be fulfilled. The turbulent quantities specified at the inlet are the turbulent intensity (0.1) and the turbulent viscosity ratio (10.0).

### B.3 Spalart-Allmaras

The standard formulation of the Spalart-Allmaras turbulence model is used (Spalart and Allmaras, 1992). An all  $y^+$  approach is used to resolve the boundary layer velocity profile. This model provides a transport equation for the modified diffusivity,  $\tilde{\nu}$  to determine the eddy viscosity

$$\nu_t = \tilde{\nu} f_{v1} \quad f_{v1} = \frac{\chi^3}{\chi^3 + c_{v1}^2} \quad \chi \equiv \frac{\tilde{\nu}}{\nu}, \quad (\text{B.11})$$

with,

$$\begin{aligned} \frac{D\tilde{\nu}}{Dt} &= c_{b1} [1 - f_{t2}] \tilde{S}\tilde{\nu} + \frac{1}{\sigma} [\nabla((\nu + \tilde{\nu})\nabla\tilde{\nu}) + c_{b2}(\nabla\tilde{\nu})^2] \\ &\quad - \left[ c_{w1}f_u - \frac{c_{b1}}{\kappa^2}f_{t2} \right] \left[ \frac{\tilde{\nu}}{d} \right]^2 + f_{t1}\Delta U^2. \end{aligned} \quad (\text{B.12})$$

The different coefficients are

$$\begin{aligned} c_{b1} &= 0.1355 & c_{b2} &= 0.622 & c_{w2} &= 0.3 & c_{w3} &= 2.0 \\ \kappa &= 0.41 & \sigma_{\tilde{\nu}} &= 2/3 & c_{\nu1} &= 7.1 & c_{prod} &= 2.0. \end{aligned}$$

The Spalart-Allamars requires only the turbulent viscosity ratio (10.0) to be specified at the inlet.

## Appendix C

# Simulation Set-up

### C.1 Wall Distance ( $y^+$ ) and Boundary Layer Depth

Boundary layer theory can be used to determine the required first cell height and the depth of the boundary layer for meshing. First the Reynolds number of the simulation is determined, using fresh water properties

$$Re_x = \frac{Ux}{\nu} = \frac{0.76 \cdot 2.9091}{1.138 \times 10^{-6}} = 1.94 \times 10^6. \quad (\text{C.1})$$

The wall distance can be calculated using the ITTC skin-friction correlation line

$$C_f = \frac{0.075}{(\log(Re_x) - 2)^2} = \frac{0.075}{(\log(1.94 \times 10^6) - 2)^2} = 4.078 \times 10^{-3}, \quad (\text{C.2})$$

for  $Re_x < 10^9$ . The wall shear stress can be expressed as

$$\tau_w = \frac{1}{2} \rho U^2 C_f = \frac{1}{2} \cdot 999.1026 \cdot 0.76^2 \cdot 4.078 \times 10^{-3} = 1.176. \quad (\text{C.3})$$

From this the friction velocity can be calculated

$$u_* = \sqrt{\frac{\tau_w}{\rho}} = \sqrt{\frac{1.176}{9989.1026}} = 0.0343. \quad (\text{C.4})$$

And finally, the wall distance

$$y = \frac{y^+ \nu}{u_*} = \frac{30 \cdot 1.0034 \times 10^{-6}}{0.0343} = 0.000994m. \quad (\text{C.5})$$

With a target  $y^+ \sim 30$  the required first cell height is (this gives us the position of the first node, which is at the centre of the cell)

$$y = 0.00198m \sim 2mm. \quad (\text{C.6})$$

The total boundary layer depth can be estimated using Schilchting formula for a turbulent boundary layer over a flat plate (Schlichting, 1979)

$$\frac{\delta}{x} = 0.37 Re_x^{-1/5} = 0.37 \cdot 1.94 \times 10^{6-1/5} = 0.02044. \quad (\text{C.7})$$

At the stern, the boundary layer depth will be

$$\delta = 0.02044 \cdot 2.9091 = 0.0595m. \quad (\text{C.8})$$

## C.2 Kelvin Wake Refinement

To create an appropriate refinement in way of the wave field generated by the hull, the expected wave length and height have to be estimated. The ITTC give an empirical formula based on the Froude number ( $Fr$ ) of the model (ITTC, 2011)

$$\lambda_w = 2\pi L_{PP} Fr^2 = 2 \cdot \pi \cdot 2.9091 \cdot 0.1424^2 = 0.37. \quad (\text{C.9})$$

Where  $L_{PP}$  is the length between perpendiculars of the model. With the minimum number of cells per wave length being around 40, the maximum spacing in the axial direction is 0.01 m.

## C.3 User Defined Functions

The pure sway displacement is defined as, in the earth fixed coordinate system:

```
((($Time>40.0)?1.0:0.0)*-0.2026*sin(2*3.14159265*(1/12)*($Time-40.0))
```

The pure yaw transverse displacement is defined as, in the earth-fixed coordinate system:

```
((($Time>43.0)?1.0:0.0)*-0.28968851*sin(2*3.14159265*(1/12)*($Time-43.0))
```

and the yaw angle is defined as, in the earth-fixed coordinate system:

```
((($Time>40.0)?1.0:0.0)*0.199579675*sin(2*3.14159265*(1/12)*($Time-40.0))
```

Normalized Helicity as per Degani et al. (1990)

```
dot($$VorticityVector, $$Velocity)/(mag($$VorticityVector)*mag($$Velocity))
```

## C.4 Experimental Data Uncertainty

KMCC2 Uncertainty Analysis Test (Hull, Prop., Rud.)

U	r'	bet	del	n	x'	y'	N'	Ft'	Fn'	the	phi	z'
0.76	0	11.915	-0.027	1075.16	-1.65E-03	0.088808	2.59E-02	1.19E-03	4.53E-03	-1.51E-01	-3.64E-02	-1.72E+00
0.76	0	11.914	-0.005	1075.35	-1.54E-03	0.087402	2.64E-02	1.10E-03	4.45E-03	-1.71E-01	-8.48E-02	-1.46E+00
0.76	0	11.98	0.006	1077.716	-1.03E-03	0.08494	2.63E-02	1.15E-03	4.35E-03	-1.58E-01	5.30E-02	1.77E+00
0.76	0	11.914	-0.002	1081.484	-1.91E-03	0.087797	2.60E-02	1.14E-03	4.52E-03	-1.47E-01	5.19E-02	-1.59E+00
0.76	0	11.913	0.013	1075.38	-2.13E-03	0.085376	2.61E-02	1.14E-03	4.53E-03	-1.75E-01	3.80E-03	-1.81E+00
0.76	0	11.914	0.012	1075.9	-1.46E-03	0.088359	2.59E-02	1.18E-03	4.44E-03	-1.30E-01	-1.80E-02	-1.46E+00
0.76	0	12.046	-0.012	1075.18	-1.17E-03	0.085668	2.62E-02	1.17E-03	4.23E-03	-1.66E-01	-5.23E-02	-1.10E+00
0.76	0	11.922	-0.014	1078.02	-1.45E-03	0.088155	2.62E-02	1.18E-03	4.28E-03	-1.81E-01	-3.38E-02	-1.56E+00
0.76	0	11.922	-0.051	1077.012	-1.82E-03	0.088331	2.58E-02	1.15E-03	4.46E-03	-1.61E-01	-2.12E-02	-1.21E+00
0.76	0	11.923	0.016	1076.381	-1.22E-03	0.086193	2.54E-02	1.17E-03	4.30E-03	-1.51E-01	-9.37E-02	-1.02E+00
			Mean	-0.0015	0.0871	0.0260						
			StdDev	0.0003	0.0014	0.0003						
			N	9	10	10						

ua(mean)	0.10%	0.44%	0.09%
ua(single)	0.31%	1.38%	0.28%
ua(single)	0.62%	2.76%	0.56%

## C.5 Signal Processing

```
from scipy.signal import butter, filtfilt

# Filter for experimental data
def butter_lowpass(cutoff, fs, order):
    nyq = 0.5 * fs
    normal_cutoff = cutoff / nyq
    b, a = butter(order, normal_cutoff, btype='low', analog=False)
    return b, a

def butter_lowpass_filter(data, cutoff, fs, order):
    b, a = butter_lowpass(cutoff, fs, order=order)
    y = filtfilt(b, a, data)
    return y
```

## C.6 Taylor Series Fit Verification

This section provides a minimal working example of the code used to fit the Taylor series expansion to the force and moment. For simplicity, sine and cosine functions are used to define the data and for the curve fitting.

```
# TAYLOR SERIES FIT TO DATA
import numpy as np
import matplotlib.pyplot as plt
from scipy.optimize import minimize

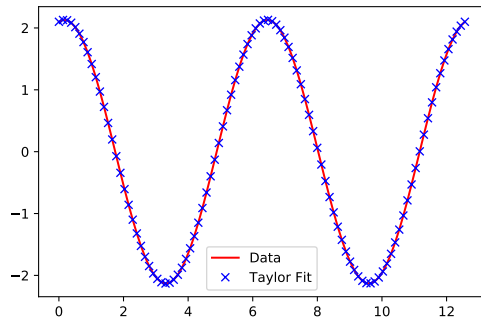
x = np.linspace(0, 4*np.pi, 100)
v = np.sin(x)
v_dot = np.cos(x)
data = 0.365*v + 2.1*v_dot

def SSE_sway(x):
    """The Taylor series expansion fit for SWAY"""
    return np.sum(1/len(data)*((x[0]*v+x[1]*v_dot)-data)**2)

res = minimize(SSE_sway, (0,0))
fit = res.x[0]*v+res.x[1]*v_dot
print(res.x[0], res.x[1])

plt.figure()
```

```
plt.plot(x, data, '-r', label='Data')
plt.plot(x, fit, 'xb', label='Taylor Fit')
plt.legend()
plt.show()
```



The two coefficients used to multiple the base function are recovered by the print function:  
0.364999366284 2.10000010111

## C.7 Free Surface Elevation

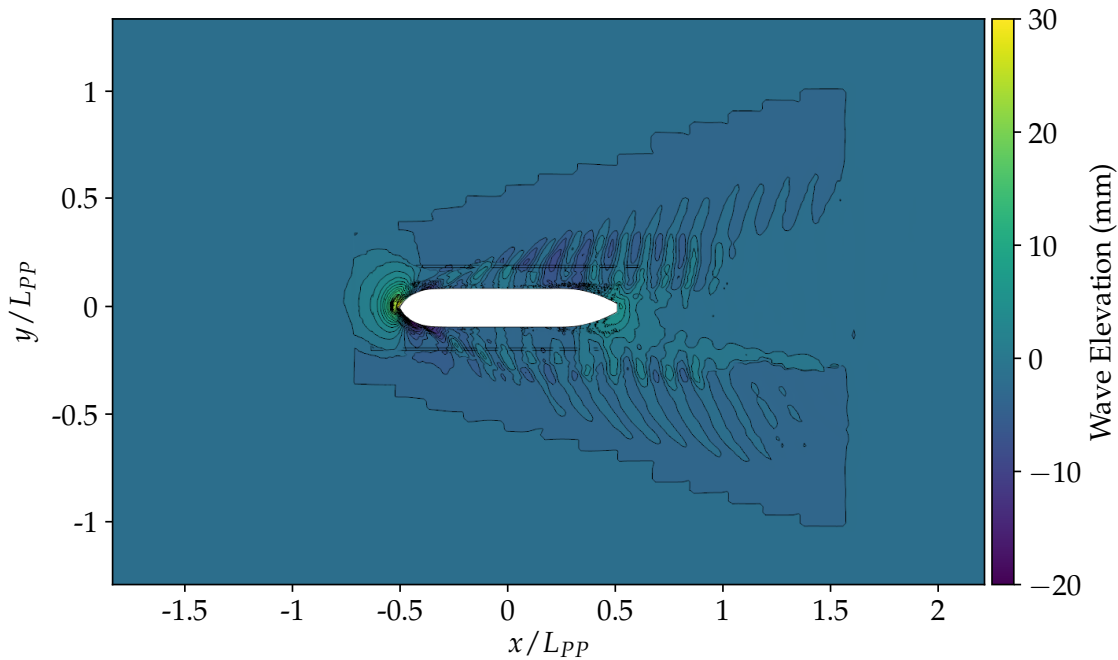


**Figure C.1:** Instantaneous free surface elevation for the PMM in pure sway at a time  $t=36$  s after motion initialisation. Initialized solution.

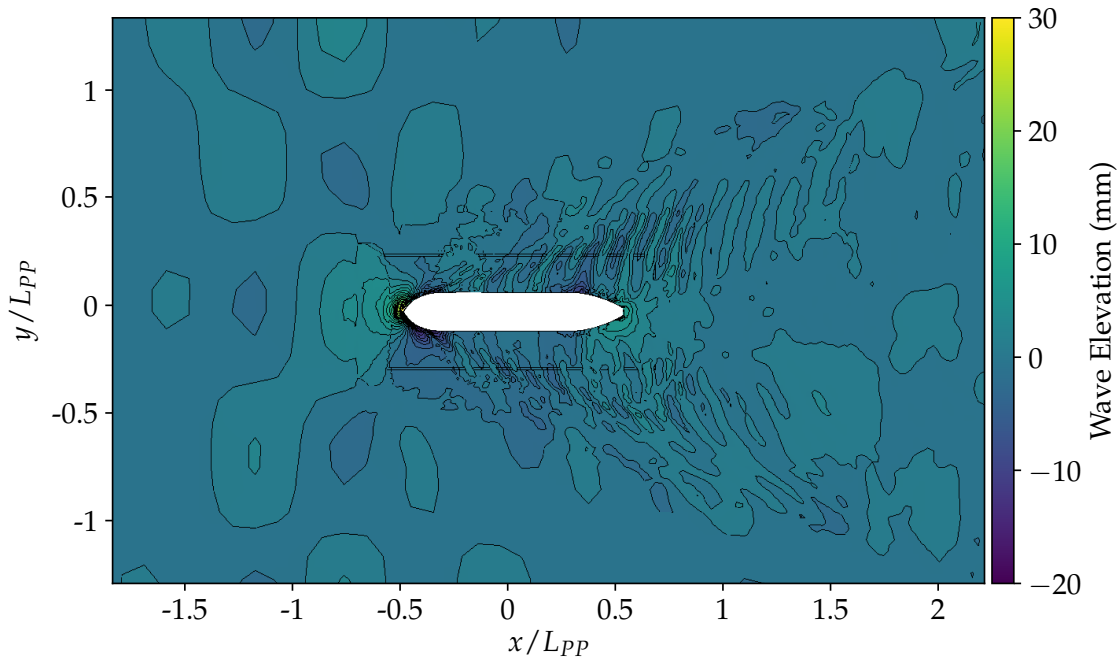


**Figure C.2:** Instantaneous free surface elevation for the PMM in pure sway at a time  $t=36$  s after motion initialisation. Non-initialized solution.

## C.8 Star-CCM<sup>+</sup> Meshing Macro

The following script was used to modify the drift angle of the model by rotating the hull and the local refinements (bow, stern, bilge) and remeshing before running. Note that for clarity purpose single lines had to be broken down.

```
// STAR-CCM+ macro: rotatemeshrun.java
// Written by STAR-CCM+ 12.04.010
package macro;
import java.util.*;
import star.common.*;
import star.base.neo.*;
import star.vis.*;
import star.meshing.*;

public class rotatemeshrun extends StarMacro {
    public void execute() {
        execute0();
    }
    private void execute0() {
        Simulation simulation_0 =
            getActiveSimulation();
        Units units_0 =
            simulation_0.getUnitsManager().getPreferredUnits(new IntVector(
                new int[] {0, 0, 0, 0, 0, 0, 0, 1, 0, 0, 0, 0, 0, 0,
                           0, 0, 0, 0, 0, 0, 0, 0, 0, 0, 0, 0, 0}));
        Units units_1 =
            simulation_0.getUnitsManager().getPreferredUnits(new IntVector(
                new int[] {0, 1, 0, 0, 0, 0, 0, 0, 0, 0, 0, 0, 0, 0,
                           0, 0, 0, 0, 0, 0, 0, 0, 0, 0, 0, 0, 0}));
        MeshPart meshPart_0 =
            ((MeshPart)
                simulation_0.get(SimulationPartManager.class)
                .getPart("Bow"));
        SimpleCylinderPart simpleCylinderPart_0 =
            ((SimpleCylinderPart)
                simulation_0.get(SimulationPartManager.class)
                .getPart("Cylinder"));
        SimpleCylinderPart simpleCylinderPart_1 =
            ((SimpleCylinderPart)
```

```
simulation_0.get(SimulationPartManager.class)
    .getPart("Cylinder_2"));
MeshPart meshPart_1 =
    ((MeshPart)
        simulation_0.get(SimulationPartManager.class)
            .getPart("Stern"));
CadPart cadPart_0 =
    ((CadPart)
        simulation_0.get(SimulationPartManager.class)
            .getPart("KVLCC2"));
LabCoordinateSystem labCoordinateSystem_0 =
    simulation_0.getCoordinateSystemManager()
        .getLabCoordinateSystem();
CartesianCoordinateSystem cartesianCoordinateSystem_0 =
    ((CartesianCoordinateSystem)
        labCoordinateSystem_0.getLocalCoordinateSystemManager()
            .getObject("CG"));
simulation_0.get(SimulationPartManager.class).rotateParts(
    new NeoObjectVector(new Object[] {meshPart_0,
        simpleCylinderPart_0,
        simpleCylinderPart_1, meshPart_1, cadPart_0}),
    new DoubleVector(new double[] {0.0, 0.0, 1.0}),
    new NeoObjectVector(new Object[] {units_1, units_1, units_1}),
    'Specify_Drift_Angle_(rad)', cartesianCoordinateSystem_0);
SubtractPartsOperation subtractPartsOperation_0 =
    ((SubtractPartsOperation)
        simulation_0.get(MeshOperationManager.class)
            .getObject("Subtract"));
subtractPartsOperation_0.execute();
AutoMeshOperation autoMeshOperation_0 =
    ((AutoMeshOperation)
        simulation_0.get(MeshOperationManager.class)
            .getObject("Automated_Mesh"));
autoMeshOperation_0.execute();
simulation_0.getSimulationIterator().run();
}
}
```

Page left intentionally blank.